

FRACTURE AND FATIGUE CRACK GROWTH CHARACTERIZATION OF
CONVENTIONAL AND HEAD HARDENED RAILWAY RAIL STEELS

A THESIS SUBMITTED TO
THE GRADUATE SCHOOL OF NATURAL AND APPLIED SCIENCES
OF
MIDDLE EAST TECHNICAL UNIVERSITY

BY

ALI MOTAMENI TABATABAEI

IN PARTIAL FULLFILLMENT OF THE REQUIREMENTS
FOR
THE DEGREE OF MASTER OF SCIENCE
IN
METALLURGICAL AND MATERIALS ENGINEERING

FEBRUARY 2014

Approval of the thesis:

**FRACTURE AND FATIGUE CRACK GROWTH CHARACTERIZATION
OF CONVENTIONAL AND HEAD HARDENED RAILWAY RAIL STEELS**

Submitted by **ALI MOTAMENI TABATABAEI** in partial fulfillment of the requirements for the degree of **Master of Science in Metallurgical and Materials Engineering Department, Middle East Technical University** by,

Prof.Dr. Canan Özgen
Dean, Graduate School of **Natural and Applied Sciences**

Prof.Dr.C.Hakan Gür
Head of Department, **Metallurgical and Materials Eng**

Prof.Dr. Rıza Gürbüz
Supervisor, **Metallurgical and Materials Eng. Dept., METU**

Assist.Prof.Dr. Kazım Tur
Co-Supervisor, **Metallurgical and Materials Eng. Dept., Atılım University**

Examining Committee Members:

Prof.Dr.C.Hakan Gür
Metallurgical and Materials Eng. Dept., METU

Prof.Dr. Rıza Gürbüz
Metallurgical and Materials Eng. Dept., METU

Assist.Prof.Dr. Kazım Tur
Metallurgical and Materials Eng. Dept., Atılım University

Prof.Dr. Bilgehan Ögel
Metallurgical and Materials Eng. Dept., METU

Prof.Dr. Ali Kalkanlı
Metallurgical and Materials Eng. Dept., METU

Date: _____

I hereby declare that all information in this document has been obtained and presented in accordance with academic rules and ethical conduct. I also declare that, as required by these rules and conduct, I have fully cited and referenced all material and results that are not original to this work.

Name, Last Name: ALI MOTAMENI TABATABAEI

Signature:

ABSTRACT

FRACTURE AND FATIGUE CRACK GROWTH CHARACTERIZATION OF CONVENTIONAL AND HEAD HARDENED RAILWAY RAIL STEELS

MOTAMENI TABATABAEI, Ali

M.S., Department of Metallurgical and Materials Engineering

Supervisor: Prof. Dr. Rıza GÜRBÜZ

Co-Supervisor: Assist.Prof. Dr. Kazım TUR

FEBRUARY 2014, 120 Pages

Fatigue crack growth behaviors of rail R260 and rail R350 HT in head, web and foot region of the rail have been investigated. Crack propagation at these three regions were compared. Furthermore, Fracture toughness (K_{IC}) values in the three region of the rail R260 and R350 HT were calculated.

Compact shear specimens were machined from the web of the rail in the longitudinal direction to conduct K_{IIC} fracture toughness of the rail R260. A special loading frame manufactured for K_{IIC} testing.

Fractographic analysis on the fracture surfaces of both mode I and mode II fracture toughness test specimens and mode I fatigue crack growth test specimens were done.

K_{IIC} values were measured 1.5 times the K_{IC} values for this steel in the web of the rail R260 grade in the longitudinal direction. As for mode I fatigue crack growth rates, head of both the rails in transvers direction shows the highest mode I fatigue crack growth resistance.

Keywords: Rail R350 HT, Rail R260, Mode I fatigue crack growth rate, mode II fracture toughness.

ÖZ

KONVENSİYONEL VE MANTARI SERTLEŞTİRİLMİŞ DEMİRYOLLARI RAYLARINDA KIRILMA VE YORULMA ÇATLAK İLERLEME BÜYÜMESİ

MOTAMENI TABATABAEI, Ali
Yüksek Lisans, Metalurji ve Malzeme Mühendisliği Bölümü

Tez Yöneticisi: Prof. Dr. Rıza GÜRBÜZ

Ortak Tez Yöneticisi: Assist.Prof. Dr. Kazım TUR

ŞUBAT 2014, 120 Sayfa

R350 HT ve R260 kalite rayların mantar, gövde ve tabanlarında yorulma çatlak ilerleme davranışı incelenmiştir. Bu üç bölgedeki çatlak ilerlemeler dikey yönünde karşılaştırılmıştır. Ayrıca, R260 ve R350 HT rayların üç bölgesinin kırılma toklukları dikey yönünde (K_{IC}) hesaplanmıştır.

Rayın gövdesinden uzunlamasına kompakt kesme numuneleri K_{IIC} kırılma tokluğunun yapılması için işlenmiş ve K_{IIC} testi için özel yükleme aparatı imal edilmiştir.

Mod II ve Mod I kırılma tokluğu testi numuneleri ile mod I yorulma çatlak ilerleme testi numunelerinin kırılma yüzeyleri fraktografik analize tabi tutulmuştur.

R260 kalite ray çeliği için K_{IIC} değerleri gövdenin uzunlamasına yönünde, K_{IC} değerlerinin 1.5 katı ölçülmüştür. Mod I yorulma çatlak ilerlemesine karşı en yüksek direnci iki ray içinde rayın mantarı dikey yönünde göstermiştir.

Anahtar kelimeler: Rail R350 HT, Rail R260, mod I yorulma çatlak ilerleme hızı, mod II kırılma tokluğu.

To My Parents

ACKNOWLEDGMENTS

I would like to thank to my supervisors Prof. Dr. Rıza Gürbüz and Assist.Prof.Dr. Kazım Tur for their valuable support and guidance in the process of constitution of this study. I would also like to express my gratitude to my supervisors for their critical comments on this study.

I owe special thanks to my father, mother and sister. My family has always encouraged me and supported my decisions. I owe a large debt of gratitude to them.

I could not have completed this undertaking without the support of Selda. She made me feel that I did not walk alone in the hardest times during the creation of this thesis. I owe a sincere thank to her. I have also special thanks for their friendship and support to Önder Şahin, Cemal Yanardağ, Yusuf Yıldırım, Ender Yurtoğlu, Serkan Yılmaz, Cengiz Tan and Göksu Gürer.

I owe special thanks to Cemali Kılınç, Sedat Ilgaz Günay, Bilge Temiz, Sedef Beşkardeşler and Beyhan for always bearing my burden with warmth and kindness.

TABLE OF CONTENTS

ABSTRACT.....	v
ÖZ	vi
ACKNOWLEDGMENTS	viii
TABLE OF CONTENTS.....	ix
LIST OF TABLES.....	xii
LIST OF FIGURES	xiii
CHAPTERS	
1.INTRODUCTION	1
2.THEORY	3
2.1. MECHANISM OF FATIGUE CRACK GROWTH.....	3
2.2. FATIGUE CRACK GROWTH RATE	8
2.3. LOADING ON RAILS	13
2.3.1. GENERAL REMARKS.....	13
2.3.2. RAIL STRESSES DUE TO WHEEL LOADING	16
2.3.2.1. BENDING STRESSES.....	16
2.3.2.2. SHEAR STRESSES.....	17
2.3.2.3. DYNAMIC EFFECTS	18
2.3.2.4 THERMAL STRESSES.....	18
2.3.2.5. RESIDUAL STRESSES	19
2.4. RAIL FATIGUE	21
2.4.1.1. HEAD CHECKS.....	21
2.4.1.2. SQUATS	22
2.4.2. RAIL HEAD CRACKS WITH INTERNAL ORIGIN	22
2.4.2.1. KIDNEY-SHAPED CRACKS.....	22
2.4.2.2. LONGITUDINAL CRACKS.....	23
2.4.3. RAIL WEB CRACKS.....	23
2.4.3.1. LONGITUDINAL VERTICAL AND HORIZONTAL CRACKS.....	23
2.4.3.2. CRACKS INITIATED AT MACHINED HOLES IN THE WEB	24

2.5. R350 HT RAIL	25
2.6. CRACK GAGE APPLICATION THEORY	28
2.6.1. DIRECT POTENTIAL METHOD	28
2.6.2. INDIRECT POTENTIAL METHOD.....	30
3.EXPERIMENTAL	35
3.1. MATERIAL.....	35
3.2. METALLOGRAPHY.....	36
3.3. MECHANICAL TESTS.....	37
3.3.1. TENSILE TEST	37
3.3.2. CHARPY IMPACT TOUGHNESS TEST.....	37
3.3.3. HARDNESS TEST.....	38
3.4. COMPACT TENSION C (T) SPECIMENS.....	39
3.5. COMPACT SHEAR SPECIMEN	43
3.6. TEST EQUIPMENT.....	47
3.7. TESTING AND DATA ACQUISITION.....	48
4.RESULTS AND DISCUSSION	51
4.1. METALLOGRAPHIC EXAMINATION	51
4.2. MECHANICAL TEST RESULTS.....	60
4.2.1. TENSION TEST.....	60
4.2.2. CHARPY IMPACT TEST RESULTS	63
4.2.3 HARDNESS TEST RESULTS	64
4.3. FRACTURE TOUGHNESS TEST K_{IC} RESULTS	67
4.4 FRACTURE TOUGHNESS K_{IIC} TESTING.....	74
4.5. MODE II FATIGUE TESTING	79
4.6. CRACK LENGTH VERSUS NUMBER OF CYCLE CURVES FOR MODE I FATIGUE TESTING	79
4.7. CRACK GROWTH RATE VS STRESS INTENSITY RANGE.....	84
4.8. PARIS –ERDOGAN LAW APPLICATION	91
4.9. COMPARISON OF THE da/dN vs ΔK	96
4.10. ELECTRON FRACTOGRAPHIC ANALYSIS	100
5.CONCLUSIONS.....	113
REFERENCES.....	115

APPENDICES	119
A. OUTPUT OF BASIC COMPUTER PROGRAM FOR R350 HT HEAD	

LIST OF TABLES

TABLES

Table 3.1. Chemical composition of Rail R350 HT and R260 in weight percentages.	36
Table 3.2. Chemical composition range of Rail R350 HT and R260 in weight percentages according to EN 13674-1:2003+A1:2007.	36
Table 4.1. Inter-lamellar spacing of R350 HT and R260.	60
Table 4.2. Tensile results of R350HT rail.	61
Table 4.3. Tensile results of R260 rail.	62
Table 4.4. R350 HT rail Impact test results.	63
Table 4.5. R350 HT rail Impact test results.	63
Table 4.6. Hardness result of head of R350HT and R260.	65
Table 4.7. Hardness result of web of R350HT and R260.	66
Table 4.8.a. Fracture toughness R350 HT results.	71
Table 4.8.b. Fracture toughness R350 HT results.	71
Table 4.9.a. Fracture toughness R260 results.	72
Table 4.9.b. Fracture toughness R260 results.	73
Table 4.10. R260 rail Shear specimen fracture toughness test results.	78
Table 4.11. Results of KIC and KIIC of rail R260 in the web.	78
Table 4.12. Results of the constants C and m.	95
Table 4.13. Mode I fatigue crack growth rate data at $\Delta K = 25 \text{ MPa.m}^{1/2}$	95
Table 4.14. Micro crack growth rate of rail R350 HT and R260.	100

LIST OF FIGURES

FIGURES

Figure 2.1. Derailment of High Speed Train in UK south of Hatfield station.....	4
Figure 2.2. Stage I and II of fatigue crack propagation.	5
Figure 2.3 Wood's model for crack initiation.....	7
Figure 2.4. Fatigue fracture ripples or striation.....	7
Figure 2.5 Fatigue striation formation by plastic blunting process.....	8
Figure 2.6.Schematic fatigue crack growth curve, crack length (a) vs number of cycle (N).	9
Figure 2.7. Schematic representation of logarithm of fatigue crack growth rate da/dN versus logarithm of stress intensity factor range ΔK	11
Figure 2.8. Modes of loading.	12
Figure 2.9. Basic Elements of the conventional railway structure.....	14
Figure 2.10. (a) A wheel rolling on a continuously welded rail. (b) Contact stresses and longitudinal stress components	15
Figure 2.11. Vertical, longitudinal and lateral forces introduced by a railway wheel on a rail.....	15
Figure 2.12. Rail head bending stress according to wheel position (left), lateral and vertical loading (right).....	17
Figure 2.13. Shear loading during the wheel passage.....	17
Figure 2.14. Corrugation of the rails (a). Flat spots on the wheels (b).	18
Figure 2.15. Extraction slices from the rail to measure residual stress by neutron diffraction method.....	20
Figure 2.16. The effect of cooling rate.....	20
Figure 2.17.Fracture due to head check.	21
Figure 2.18. Spalling of the rail	21
Figure 2.19. Propagation of a squat.	22

Figure 2.20. Kidney-shaped crack.....	22
Figure 2.21. Gauge corner crack.	23
Figure 2.22. Longitudinal web crack.	23
Figure 2.23. Horizontal web crack.	24
Figure 2.24. Web cracks at fishbolt hole.....	24
Figure 2.25. Magnetic Particle Graph of the rail grade 220.....	25
Figure 2.26. Magnetic Particle Graph of the rail grade 260.....	26
Figure 2.27. Magnetic Particle Graph of the rail grade R350 HT.....	26
Figure 2.28. Micro graph of grade R220.....	27
Figure 2.29. Micro graph of grade R260.....	27
Figure 2.30. Micro graph of rail R350 HT.....	27
Figure 2.31. Scheme of a DIRECT POTENTIAL METHOD.	28
Figure 2.32. Out put potential (ΔU) versus crack length (a).	29
Figure 2.33. Out put potential (ΔU) versus crack length (a) for different Alloy A & B.	29
Figure 2.34. Crack-gage/fractomat working principle in indirect potential method..	30
Figure 2.35. Potential distribution on a foil strip.	31
Figure 2.36. Various crack gages.	32
Figure 2.37. Fractomat Control and Read out instrument working principle.	32
Figure 2.38. Fractomat Control and Read out instrument.....	33
Figure 3.1. 60 E 1 (UIC 60) rail profile.	35
Figure 3.2. Metallographic examination specimen.	37
Figure 3.3. Rail brought from TCDD.....	38
Figure 3.4. Positions of hardness testing.....	39
Figure 3.5. Fracture toughness compact tension specimen configuration.	40
Figure 3.6. Fatigue crack growth compact tension specimen configuration.....	40
Figure 3.7. Fatigue crack chevron starter notch configuration.	41
Figure 3.8. Displacement gage.....	41
Figure 3.9. (a) Finished fracture toughness with dimension of both rail R350 HT and R260.	42

Figure 3.9. (b) Finished fatigue crack growth specimen with dimension of both rail R350 HT and R260.....	42
Figure 3.10. The compact shear specimen.....	43
Figure 3.11. Loading frame (R1=95mm, R2=20mm).....	43
Figure 3.12. Straight through notch.....	44
Figure 3.13. Compact shear specimen technical drawing.....	44
Figure 3.14. Loading frame Technical drawing.....	45
Figure 3.15. The compact shear specimen.....	45
Figure 3.16. Precracking shear specimen in mode I condition.....	46
Figure 3.17. MTS 810 servo-hydraulic dynamic testing machine.....	47
Figure 3.18. Clevis and pin assembly for fatigue crack growth propagation test.....	48
Figure 3.19. Crack foil installation process on the specimen.....	49
Figure 3.20. Gluing tool apparatus.....	50
Figure 3.21. Compact tension specimen with crack gage and transferring data cables.....	50
Figure 4.1. Microstructure of rail R350 HT (a) head : Structure is pearlite, Magnification: 100X.....	51
Figure 4.1. Microstructure of rail R350 HT (b) web : Structure is pearlite, Magnification: 100X.....	52
Figure 4.1. Microstructure of rail R350 HT (c) foot: Structure is pearlite, Magnification: 100X.....	52
Figure 4.2. Microstructure of rail R260 (a) head : Structure is pearlite, Magnification: 100X.....	53
Figure 4.2. Microstructure of rail R260 (b) web : Structure is pearlite, Magnification: 100X.....	53
Figure 4.2. Microstructure of rail R260 (c) foot: Structure is pearlite, Magnification: 100X.....	54
Figure 4.3. Microstructure of rail R350 HT (a) head : Structure is pearlite, Magnification: 200X.....	54

Figure 4.3. Microstructure of rail R350 HT (b) web : Structure is pearlite, Magnification: 200X	55
Figure 4.3. Microstructure of rail R350 HT (c) foot : Structure is pearlite, Magnification: 200X	55
Figure 4.4. Microstructure of rail R260 (a) head: Structure is pearlite, Magnification: 200X	56
Figure 4.4. Microstructure of rail R260 (b) web: Structure is pearlite, Magnification: 200X	56
Figure 4.4. Microstructure of rail R260 (c) foot: Structure is pearlite, Magnification: 200X	57
Figure 4.5. Microstructure of rail R350 HT head: Structure is pearlite, Magnification: 10000X	57
Figure 4.6. Microstructure of rail R350 HT head: Structure is pearlite, Magnification: 10000X	58
Figure 4.7. Microstructure of rail R260 head: Structure is pearlite, Magnification: 10000X	58
Figure 4.8. Microstructure of rail R260 head: Structure is pearlite, Magnification: 10000X	59
Figure 4.9.(a) R350 HT tensile specimens.	60
Figure 4.9.(b) Tensile stress versus Axial strain diagram of head of rail R350 HT. .	61
Figure 4.10.Hardness position of rail R 260.	64
Figure 4.11.Hardness position of rail R350 HT.	65
Figure 4.12.Sinoidal form of fatigue loading.	67
Figure 4.13. Displacement gage attached to integral knife edges of specimen.	68
Figure 4.14. Force versus crack mouth opening displacement record.	69
Figure 4.15. Average crack size measurement for three specimen head, web and foot of rail R350 HT.	70
Figure 4.16. Sinoidal form of fatigue loading.	75
Figure 4.17. (a) Mode I loading. (b)specimen inserted in frame.	75
Figure 4.18. Shear specimen inserted in loading frame.	76
Figure 4.19. Force versus displacement record.	77

Figure 4.20. Shear specimen after fracture.	77
Figure 4.21. Mode II fatigue crack growth specimen.	79
Figure 4.22. (a) Applied fatigue loads lower than K_{max} (b) Constant range repeating loading.	80
Figure 4.23. Crack length versus number of cycles of R350 HT HEAD.	81
Figure 4.24. Crack length versus number of cycles of R350 HT WEB.	81
Figure 4.25. Crack length versus number of cycles of R350 HT FOOT.	82
Figure 4.26. Crack length versus number of cycles of R260 HEAD.	82
Figure 4.27. Crack length versus number of cycles of R260 WEB.	83
Figure 4.28. Crack length versus number of cycles of R260 FOOT.	83
Figure 4.29. da/dN vs. ΔK plot of R350 HT HEAD.	85
Figure 4.30. da/dN vs. ΔK plot of R350 HT WEB.	86
Figure 4.31. da/dN vs. ΔK plot of R350 HT FOOT.	87
Figure 4.32. da/dN vs. ΔK plot of R260 HEAD.	88
Figure 4.33. da/dN vs. ΔK plot of R260 WEB.	89
Figure 4.34. da/dN vs. ΔK plot of R260 FOOT.	90
Figure 4.35. da/dN vs. ΔK plot.	91
Figure 4.36. Linear region of da/dN vs. ΔK plot of R350 HT HEAD.	92
Figure 4.37. Linear region of da/dN vs. ΔK plot of R350 HT WEB.	92
Figure 4.38. Linear region of da/dN vs. ΔK plot of R350 HT FOOT.	93
Figure 4.39. Linear region of da/dN vs. ΔK plot of R260 HEAD.	93
Figure 4.40. Linear region of da/dN vs. ΔK plot of R260 WEB.	94
Figure 4.41. Linear region of da/dN vs. ΔK plot of R260 FOOT.	94
Figure 4.42. Comparison of da/dN vs. ΔK plot of R350 HT HEAD versus R260 HEAD.	96
Figure 4.43. Comparison of da/dN vs. ΔK plot of R350 HT WEB versus R260 WEB.	97
Figure 4.44. Comparison of da/dN vs. ΔK plot of R350 HT FOOT versus R260 FOOT.	98

Figure 4.45. SEM fractographs of Mode I Fracture Toughness Specimen in WEB Longitudinal Direction of R260.(a) General view of fracture surface transition from fatigue precrack to final loading region Magnification:100 X..... 101

Figure 4.45. SEM fractographs of Mode I Fracture Toughness Specimen in WEB Longitudinal Direction of R260.(b) Fatigue fracture striations in precrack region between two tear ridges. Magnification:8000 X. 101

Figure 4.45. SEM fractographs of Mode I Fracture Toughness Specimen in WEB Longitudinal Direction of R260.(c) Final loading region with brittle cleavage fracture and river markings in each grain. Magnification: 800 X.....102

Figure 4.46. SEM fractographs of Mode II Fracture Toughness Specimen in WEB Longitudinal Direction of R260 (a) General view of elongated shear dimples on the ductile fracture surface. Magnification: 10000 X. 102

Figure 4.46. SEM fractographs of Mode II Fracture Toughness Specimen in WEB Longitudinal Direction of R260(b) Cup-like depressions of shear dimples can be seen easily in the close view of ductile fracture. Magnification: 20000 X103

Figure 4.47. SEM fractographs of R350 HT HEAD in Transverse Direction (a) Fatigue crack propagation from starter chevron notch. Magnification: 50 X 103

Figure 4.47. SEM fractographs of R350 HT HEAD in Transverse Direction.(b) Fatigue striations in the stage II region. Magnification: 13000 X104

Figure 4.47. SEM fractographs of R350 HT HEAD in Transverse Direction. (c) Close view of fatigue striations in the stage II region. Magnification: 25000 X104

Figure 4.48. SEM fractographs of rail R350 HT WEB in Transverse Direction.(a) Fatigue crack propagation striations between tear ridges. Magnification: 5000 X. .105

Figure 4.48. SEM fractographs of rail R350 HT WEB in Transverse Direction.(b) General view of fatigue crack propagation in stage II region. Magnification: 500 X 105

Figure 4.48. SEM fractographs of rail R350 HT WEB in Transverse Direction.(c) Brittle cleavage fracture and river markings in each grain. Magnification: 1000 X.....106

Figure 4.48. SEM fractographs of rail R350 HT WEB in Transverse Direction(d) Secondary cracks between striations and tear ridges on different planes.

Magnification: 12000 X.....	106
Figure 4.49. SEM fractographs of rail R350 HT FOOT in Transverse Direction. (a) Pearlite morphology in stage II region of fatigue crack propagation. Magnification: 10000 X.....	107
Figure 4.49. SEM fractographs of rail R350 HT FOOT in Transverse Direction. (b) Fatigue striation in direction of fatigue crack propagation. Magnification: 5000 X.....	107
Figure 4.49. SEM fractographs of rail R350 HT FOOT in Transverse Direction. (c) Transition from fatigue crack propagation region to fast brittle fracture region. Magnification: 100 X.....	108
Figure 4.50. SEM fractographs of rail R260 HEAD in Transverse Direction. (a) Crack propagation in stage II region on multiple plateaus at different elevations. Magnification: 8000 X.....	108
Figure 4.50. SEM fractographs of rail R260 HEAD in Transverse Direction. (b) Close view of tear ridges and fatigue striation. Magnification: 25000 X.....	109
Figure 4.50. SEM fractographs of rail R260 HEAD in Transverse Direction. (c) Joining of two fatigue striation plateaus by tear ridges. Magnification: 15000 X..	109
Figure 4.51. SEM fractographs of rail R260 WEB in Transverse Direction. (a) Joining of fatigue striation by walls which contain fatigue striation. Magnification: 10000 X.....	110
Figure 4.51. SEM fractographs of rail R260 WEB in Transverse Direction. (b) Forming of secondary cracks between fatigue striations. Magnification: 10000 X	110
Figure 4.51. SEM fractographs of rail R260 WEB in Transverse Direction. (c) Fatigue striations in stage II region of propagation. Magnification: 15000 X.....	111
Figure 4.52. SEM fractographs of rail R260 FOOT in Transverse Direction. Fatigue crack propagation between two tear ridges. Magnification: 12000 X.....	111

CHAPTER 1

INTRODUCTION

Today in urban and interurban transport, railways are preferred due to safety, speed and comfort they suggest. With the development of high speed railway systems the time needed for journeys decreased significantly. Increase in train performance and rail traffic necessitated the development of new grades of materials used in the construction of rails. Reviewing and improving the old studies with the light of new improvements have become crucial. The modernization of railways constructed for normal speed trains is achieved by investigations of mechanisms of deformation and derailment and by elimination of the defects identified as the root causes for such problems.

Turkish State Railways Authority (TCDD) has launched huge investment programs to renovate the existing lines which are at least 70 years old, and to extend the railway network all over Turkey. It has been planned that total network length would increase to about 24.000 km from present network of only about 9.000 km. Some part of these new lines will be for high-speed trains.

One important subject in this context is the development of high capacity 60 kg/m R260 rails, which have been domestically produced by KARDEMİR AŞ at its new rail mill since 2006, and R350HT head hardened rails, domestic production technology of which is underway and TÜBİTAK has recently granted substantial amount of R&D fund for this purpose and rail welding to a consortium consisting of KARDEMİR AŞ, Atılım University and Karabük University for a duration of 36 months.

Parallel to this huge investment launch in Turkey, Turkish universities and research institutions should launch research projects on all areas of rail transportation systems such as railway electronics, signaling, scheduling, and may be the most notably on

materials research covering many metallic materials and production technologies for different grades of steel rails, car wheels, axles, engines, and for many other components. Research projects on these areas will be eminent for the success and safe introduction of new domestically produced materials and components for the entire railway system.

Therefore; with the development of domestic technologies outlined above, deformation, fracture and fatigue mechanisms of the steel rails are among the most important ones and they should be studied based on a systematic approach.

The scope of this study is to investigate fracture and fatigue crack growth of UIC 900A (grade R260) which has been mostly used in the past and present in railway network of TURKEY, and 'HEAD HARDENED' R350 HT grades rail steels.

CHAPTER 2

THEORY

2.1. MECHANISM OF FATIGUE CRACK GROWTH

The fatigue failures discovered in 1800 s when several inspectors in the Europe seen that railway rails and bridges were fractured by means of repeated loading [1]. As the progressed century the use of metals in engineering application increased and components used in many application of engineering failed owing to the repeated load.

Fatigue term can be defined as advancing, localized and permanent change in the metallic material in which subjected to repeated stresses and fluctuating strains at stresses less than yield strength of the material of interest. This fluctuating stresses and strains eventually cause cracking or failure of the component [2]. Most of engineering components have fluctuating stress and strains below the yield strength of the material. In spite of the low value of the acting cyclic stresses, failure of the component because of accumulation of the damage is inevitable. It is assumed that 80 percent of failures in brittle materials have some period of propagation of crack [3].

There is no doubt that fatigue failure plays a big role in design of all components. Most of the engineering components exposed to cyclic stresses and strains so fatigue failure is an essential role in all cases. However, it is critical in the design of the component of interest to take account the nucleation processes rather than fatigue which may cause nucleation and propagation of cracks under cyclic loading in the service life of the component. Figure 2.1 indicate a disaster fatigue failure of the rail in October 2000 in UK. Four Passengers were killed and seventy passengers were injured.



Figure 2.1. Derailment of High Speed Train in UK south of Hatfield station [4].

Fatigue failures starts with forming of micro cracks and then coalesces of micro cracks and then propagation of cracks which end with fracture after enough number of fluctuations. Fatigue failure is caused by the action of the cyclic stress, plastic strain and tensile stress at the same time. If one of these is not exist, a fatigue crack will not initiate and propagate. The plastic strains arise from cyclic stresses initiate the crack in the component; tensile stresses assist crack propagation in the component. Compressive stresses will not result in fatigue but compressive loads may lead to local tensile stresses. Microscopic plastic strains also can be existed at the low stress levels where strain might appear to be elastic [5].

Fatigue cracks mainly start at highly stressed regions of a component exposed to the cyclic stresses of enough magnitude. Crack propagation in components under the applied stress continues through the material in which fracture toughness of material is surpassed and final sudden fracture occurs. On the microscopic scale, nucleation of cracks under the reversed cyclic stresses which pass the flow stress is the most property of fatigue process. Fatigue cracks occur along slip bands, grain boundaries. Afterward, fatigue crack growth by means of opening and closing movement at the tip of the crack which cause striations that are parallel to the crack front [6].

Fatigue failure process divided into the following stages:

Stage I: Crack nucleation and initiation.

Stage II: Crack propagation in the direction of normal to maximum tensile stress.

Stage III: Final fracture occurs when crack has reached to sufficient length

In stage I of the fatigue, a fatigue crack started at the specimen surface. Crack initiation at stage I is formed at the surface where the planes are under high shear stress. In this stage crack propagation rate is about angstroms per cycle. After extension of the initial crack from the surface in the order of few grains in length, stage II of fatigue starts and crack propagation continue across the crack front. The propagation rate of stage II is comparatively high it is approximately in the order of microns per cycle. Stage III occurs when the cross section of the specimen or the component cannot support the applied load.

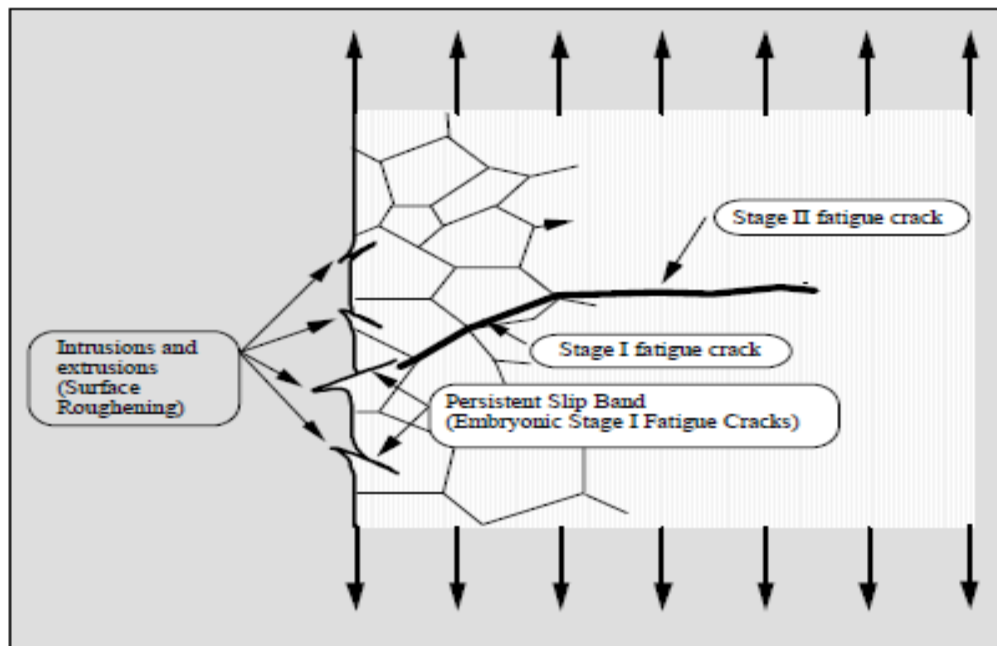


Figure 2.2. Stage I and II of fatigue crack propagation [7].

The nucleation process of undamaged material can be explained by intrusion-extrusion mechanism, shown in Figure 2.2. As a result of dislocation movement slip bands are formed within individual grains. Slip bands generally formed in the first

few thousand cycles of stress. When the stress is low only some of grains have favorable orientations in which shear stresses are in a magnitude that can start plastic deformation and as a result only a few slip bands form. When the stress is high, plastic deformation forms in many grains and a large amount of slip band form. When cyclic loading occurs, the slip is working back and forth on the slip bands and finally a fatigue crack is generated along the persistent slip band. By working slip in the back and forth on the slip line, an important structural feature of fatigue appears which is unique to fatigue deformation. Ridges and grooves in other words slip band extrusions and slip band intrusions forms in the free surface of the material. By careful metallography examination it can be seen that fatigue crack initiate at intrusions and extrusions [8].

W.A.Wood proposes a mechanism for producing slip-band extrusions and intrusions [9]. He conducted microscopic observation of produced slip by fatigue. He observed that slip bands are caused by build of fine slip movements. Slip movements are in the order of 1 nm rather than steps of 100 to 1000 nm. As seen in Figure 2.3. which shows wood's concept how deformation by slip can lead to a fatigue crack. Slip produced by deformation produce a counter at the surface of the metal. As a result of back-and-forth fine slip motions of fatigue cause notches or ridges at the surface of the metal .So notches result from fine movements of fatigue acts as a stress riser with a notch root in the order of atomic dimensions. This situation is the point of a fatigue crack.

In the stage I of the crack propagation, crack propagates along the persistent slip bands. In polycrystalline metals crack extension is in the order of few grain diameters prior the crack propagation alter to stage II. The propagation rate of crack in stage I is very low approximately about nm per cycle but propagation in stage II is in the order of microns per cycle. The fracture surface of stage II of crack propagation illustrates a pattern of ripple or striations. Each striation produced by single cycle of stress as shown in Figure 2.4.

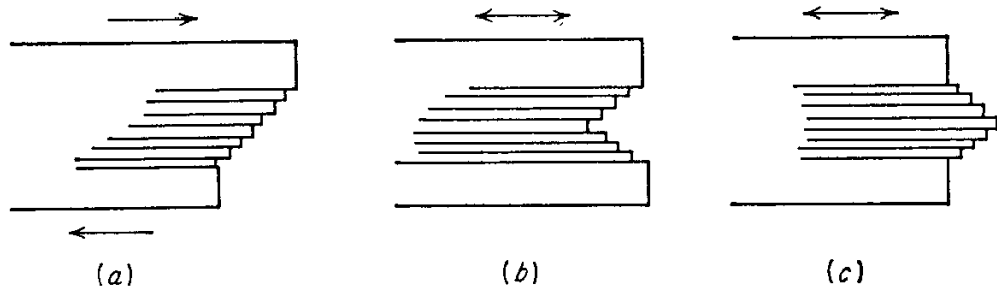


Figure 2.3 Wood's model for crack initiation [9].

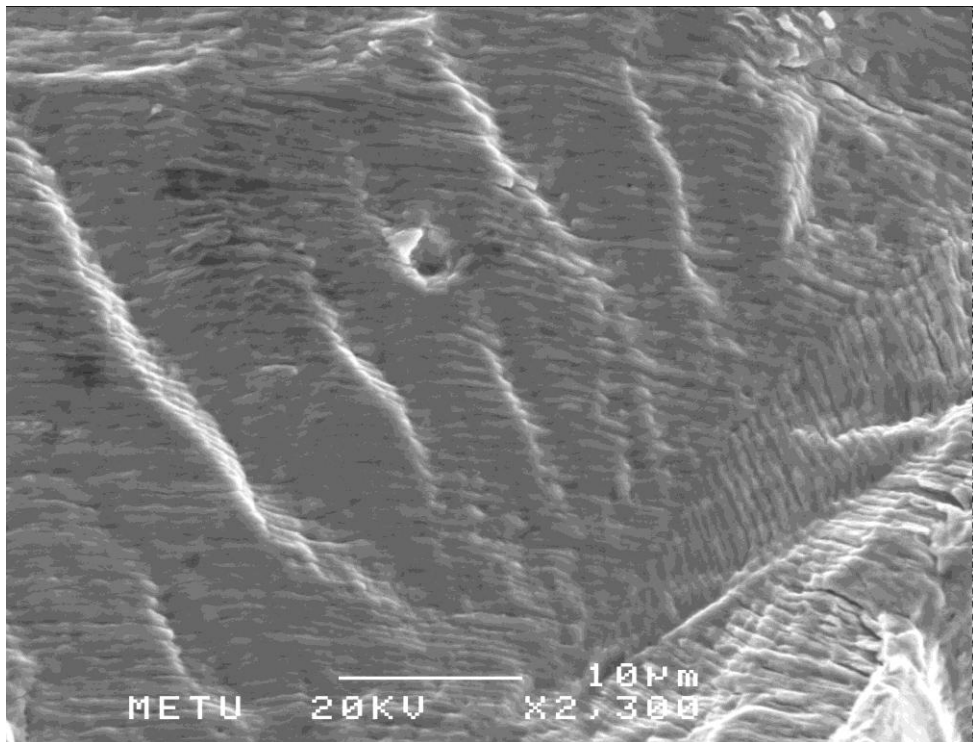


Figure 2.4. Fatigue fracture ripples or striation.

Stage II of the crack propagation happened by plastic blunting process. A head of growing crack as shown in Figure 2.5-a crack tip is sharp. When the tensile force is applied the double notch at the tip of the crack concentrate the slip along the planes which is 45° to the plane of the crack as shown in Figure 2.5-b. By plastic shearing crack extend to its maximum and the tip of the crack becomes blunter. When applied

load alters to compression the direction of the slip at the end of the crack tip zone reversed (fig 2.5- d).

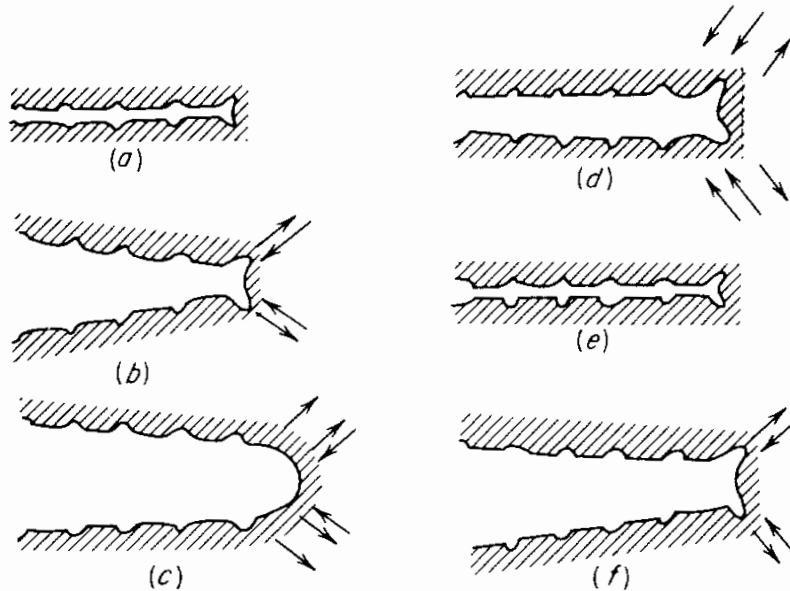


Figure 2.5 Fatigue striation formation by plastic blunting process [10].

2.2. FATIGUE CRACK GROWTH RATE

Although measurements can be take into account to minimize the possibility of fatigue failures, materials are not free of defects .There are always cracks and nucleation sites in structural component of materials. Components under cyclic loading, cracks will form and grow through the structure so the extension of cracks ultimately causes the sudden failure of the component [11]. Results of fatigue research have illustrated that the life of structural component can be correlated to the rate of fatigue propagation. Cracks can extend from hardly detectable size to some critical value during stage II growth. Experimental techniques are exists to monitor crack length during cyclic loading [11].

The fatigue crack growth rate of a material (da/dN) is simply the slope of a (crack length) versus N (number of cycles) curve fig 2.6. at a given number of cycles or length of crack.

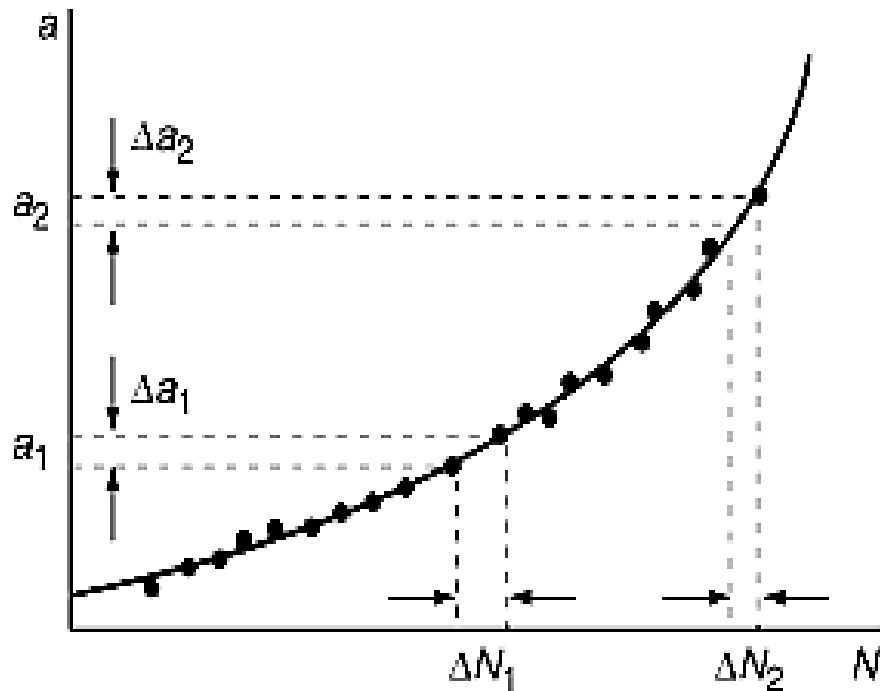


Figure 2.6. Schematic fatigue crack growth curve, crack length (a) vs number of cycle (N).

If a component or material which containing crack is exposed to cyclic loading, the length of the crack in it (a) increases with the number of fatigue cycle (N) when cyclic frequency (ν), load ratio (R) and load amplitude (ΔP) held constant. The crack propagation rate, da/dN , increases as the crack length of the specimen increases during the test. The crack propagation rate is also high for any given crack length performed at high load amplitudes. From these observations it can be concluded that:

$$\frac{da}{dN}_{R,\nu} = f \Delta P, a$$

Where the function in the above expression f , is dependent on the geometry of the specimen, the loading configuration, the length of the crack as well as range of the cyclic loading. This general relationship can be simplified via the stress intensity range parameter, ΔK . The magnitude of the load range (ΔP), crack length and the geometry is expressed by ΔK as follows:

$$\Delta K = K_{\max} - K_{\min}$$

$$K_{\max} = f(\sigma_{\max}, a)$$

$$K_{\min} = f(\sigma_{\min}, a)$$

Stress intensity range can also be defined in terms of stress ratio as follows relationships:

$$\Delta K = (1 - R)K_{\max} \text{ for } R \geq 0$$

$$\Delta K = K_{\max} \text{ for } R \leq 0$$

Experiments done on fatigue crack growth rate for almost all metallic materials have illustrated that the da/dN versus ΔK curves have three distinguishable regions [10]. A characteristic sigmoidal shape of this curve is shown in Figure 2.7. The fatigue crack propagation threshold can be seen in the first region of this curve. Below this region, ΔK_{th} , there is not observable crack propagation. At stresses below ΔK_{th} cracks are non-propagating cracks. By increasing stress intensity factor, crack propagates in the order of 0.25 nm/ cycle in the region I. By increasing stress intensity factor crack propagation rate increases and region II of the curve is observed. In this region plastic blunting process occurs and striation can be observed. Region II of this curve is important since $\log da/dN$ and $\log \Delta K$ has linear relationship in this region. Region II called Paris region. Region III is the region where crack propagation rate is so high and instability occurs in this region and fatigue crack propagation life is so low. In this region maximum stress intensity K_{\max} approaches fracture toughness of the K_c of the material.

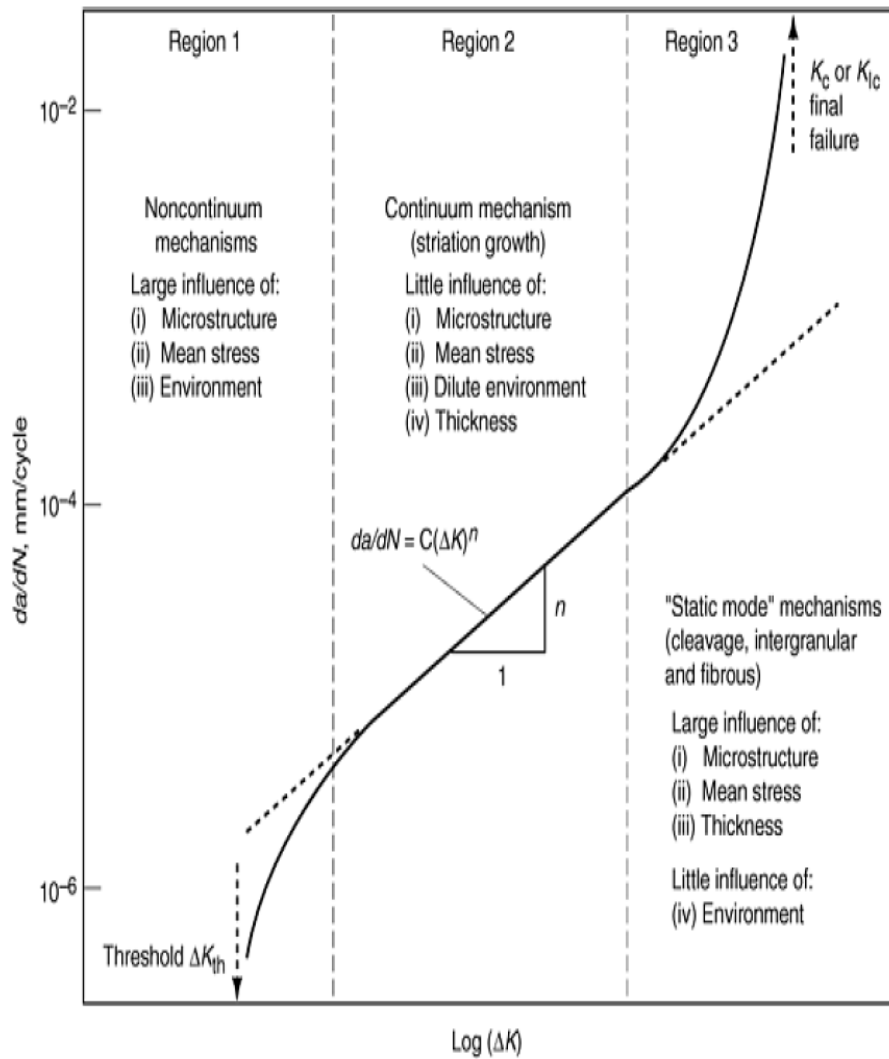


Figure 2.7. Schematic representation of logarithm of fatigue crack growth rate da/dN versus logarithm of stress intensity factor range ΔK [6].

Lots of studies conducted which describes the crack growth propagation rate curve in semi or wholly empirical manner. The most widely used model is published by two researcher's Paris and Erdogan in 1963: [10]

$$\frac{da}{dN} = C \Delta K^m$$

In the above empirical equation C is the slope of the curve in the linear region and A is the value found by extending the straight line to the stress intensity factor where it is $1 \text{ MPa m}^{1/2}$. The constant C in the equation includes effects of material, loading frequencies, mean load and environment. The constant m in the equation is an empirical constant which is in the range of 2 and 7. For ductile materials exponent m is between 2 and 4.

For opening (Mode I) fatigue, it is figured out that ΔK refers to the range of opening (Mode I) stress intensity factors during stress cycle. In the same manner, in sliding (Mode II) and tearing (Mode III) (Fig 2.8.) also a stress intensity factor range ΔK_{II} or ΔK_{III} can be utilized in Paris-Erdogan equation to characterize fatigue crack propagation in modes II and III. Fatigue life of components can be estimated by knowing the empirical constants defined above as m and C and knowing fracture toughness of the material.

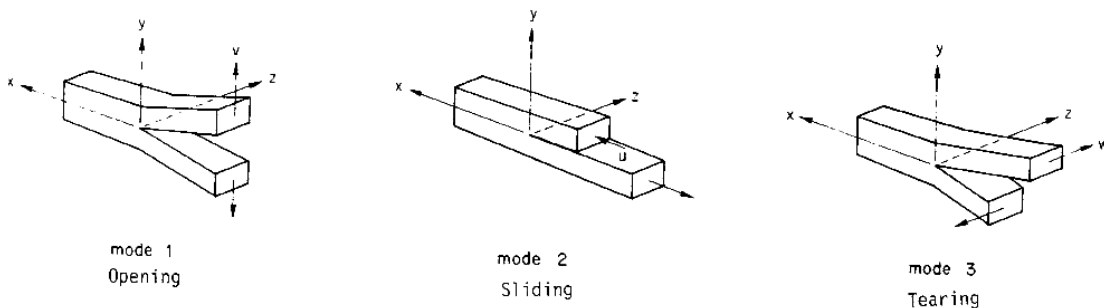


Figure 2.8. Modes of loading.

In 1967, Forman et al [12] proposed another equation which is known as Forman equation. This equation is applicable widely for fatigue crack propagation of aluminum alloys. This equation also specifies crack propagation rate for both stage II and stage III.

$$\frac{da}{dN} = \frac{C \Delta K^m}{1 - R (K_c - \Delta K)}$$

In the above equation, K_c is fracture toughness of material and R is the stress ratio ($\frac{\sigma_{min}}{\sigma_{max}}$). It is clear from the above equation dependency of da/dN on stress ratio and fracture toughness of the material. Fatigue crack propagation decreases with increasing load ratio and decreasing fracture toughness of the material of the interest

In 1972, Pearson et al., changed the equation by explaining the fact that short fatigue cracks may grow at stress intensity levels which is below the threshold level for macroscopic cracks.

$$\frac{da}{dN} = \frac{C \Delta K^m}{1 - R (K_c - \Delta K)^{1/2}}$$

Ewalds and Wanhill [13] developed an equation to describe the whole sigmoidal curve by the formula below.

$$\frac{da}{dN} = C \Delta K^m \frac{1 - \frac{\Delta K_{th}}{\Delta K}^{n_1 n_3}}{1 - \frac{\Delta K_{max}}{\Delta K}^{n_2}}$$

In the above equation ΔK_{th} is the near threshold intensity factor and n_1 , n_2 and n_3 are empirically found constants.

2.3. LOADING ON RAILS

2.3.1. GENERAL REMARKS

The elements of a conventional railway track are illustrated in Figure 2.9. These elements are the rails, the sleepers including the ballast bed, the subgrade and fasteners.

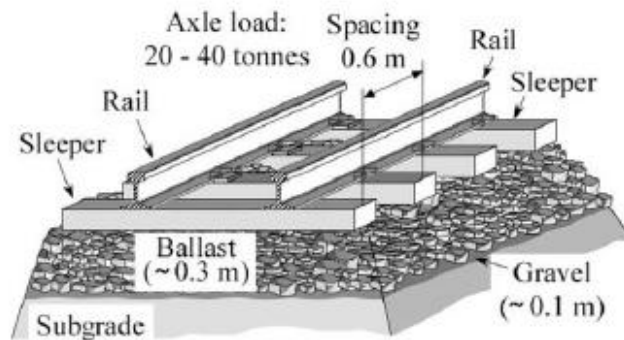


Figure 2.9. Basic Elements of the conventional railway structure [14].

According to Esweld [15] the running surface of the rail is the highest stress point where the stress reaches to 1500 MPa at the wheel-rail contact for an axle load of 25 tons.

Up to the 1930's joining was performed to piece together the rails; however this causes fatigue cracks to occur at the holes, so frequent maintenance was required. Continuous welding of the rails was used to solve this problem around 1930, but welding cause to develop residual stress, microstructure and toughness inhomogeneity in the material [16]. As well as contact stress, both shear and bending stresses due to wheel loading contribute to the fatigue crack propagation. These stresses combined with the residual stress resultant from manufacturing and thermal stress depending on the ambient temperature. The complex stress state in longitudinal direction is illustrated in Figure 2.10.

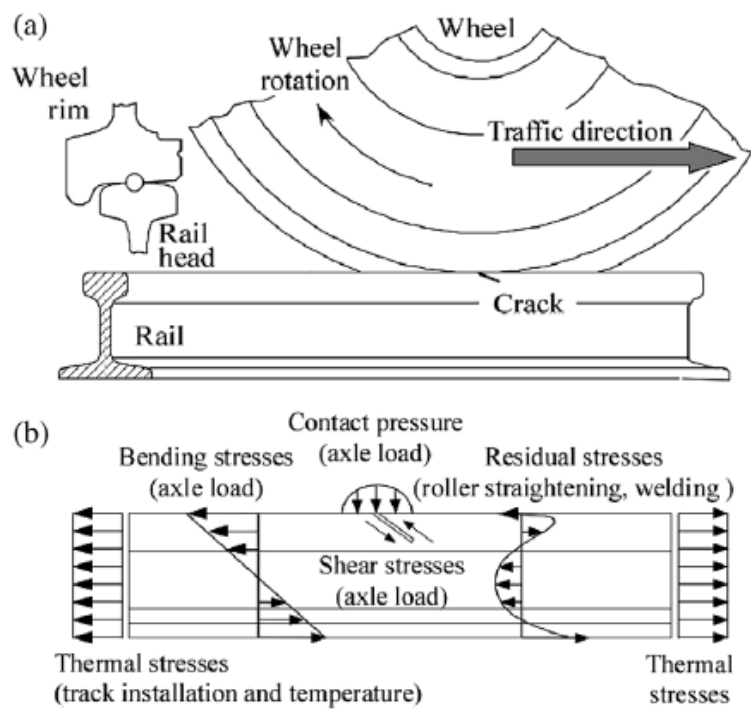


Figure 2.10. (a) A wheel rolling on a continuously welded rail. (b) Contact stresses and longitudinal stress components [16].

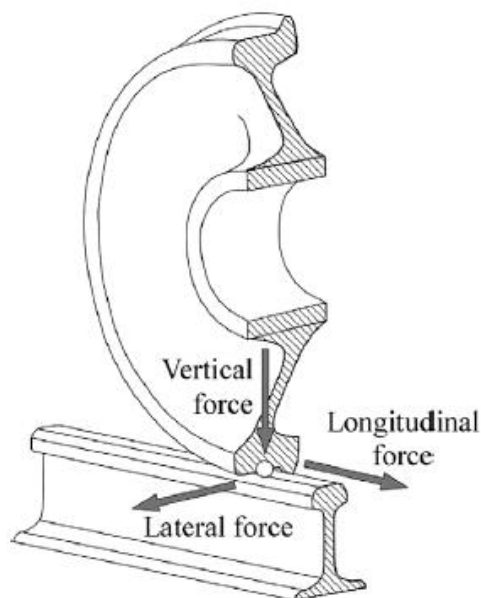


Figure 2.11. Vertical, longitudinal and lateral forces introduced by a railway wheel on a rail [16].

2.3.2. RAIL STRESSES DUE TO WHEEL LOADING

2.3.2.1. BENDING STRESSES

Vertical and lateral forces acting on the rail which illustrated in Figure 2.11, causes bending of the rail and bending moments can be calculated according to formula;

$$M_y(x) = \frac{F_v}{4\lambda_v} \cdot (\cos \lambda_v x - \sin \lambda_v x) \cdot \exp(-\lambda_v x) \quad (1)$$

$$M_z(x) = \frac{F_l}{4\lambda_l} \cdot (\cos \lambda_l x - \sin \lambda_l x) \cdot \exp(-\lambda_l x) \quad (2)$$

$$\lambda_v = (k_v/4E \cdot I_{yy})^{0.25} \quad (3)$$

$$\lambda_l = (k_l/4E \cdot I_{zz})^{0.25} \quad (4)$$

where: F_v is vertical wheel load

F_l is lateral wheel load

k_v is vertical foundation stiffness

k_l is lateral foundation stiffness

E is elastic modulus of elasticity

I_{yy} is second moment of area with respect to horizontal axis

I_{zz} is second moment of area with respect to vertical axis

According to equation (1), the maximum tensile stress occurs at a distance from wheel position at the surface of the rail head which can be seen from Figure 2.12 [17]. Both of the bending stresses contribute to the fatigue but vertical bending stress dominates according to [18].

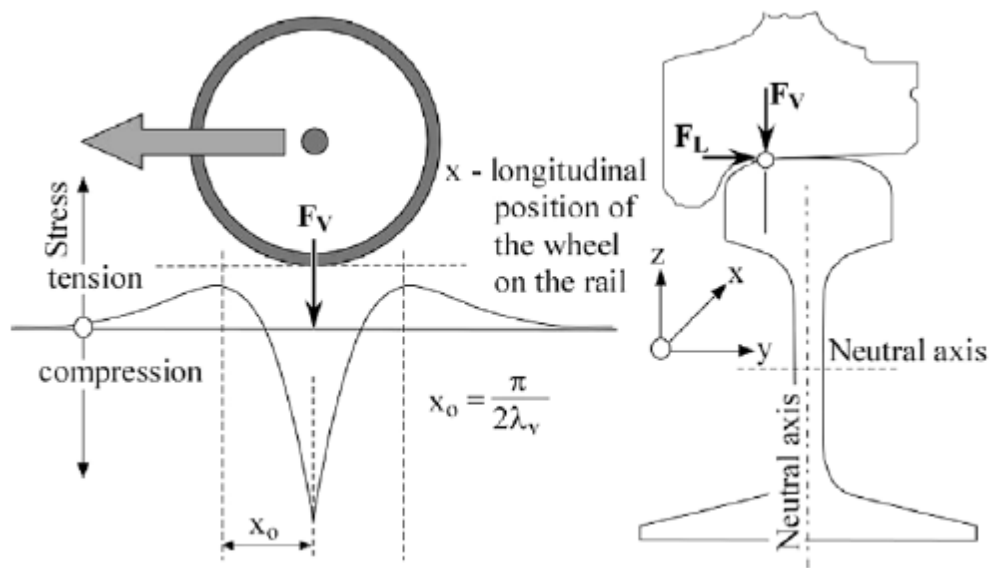


Figure 2.12. Rail head bending stress according to wheel position (left), lateral and vertical loading (right) [17].

2.3.2.2. SHEAR STRESSES

The shear stresses generated on the rail known as the reason of failure at the bolt holes in joined rails [18] because they cause to occur mixed type loading on rails as shown in the figure 5 [19].

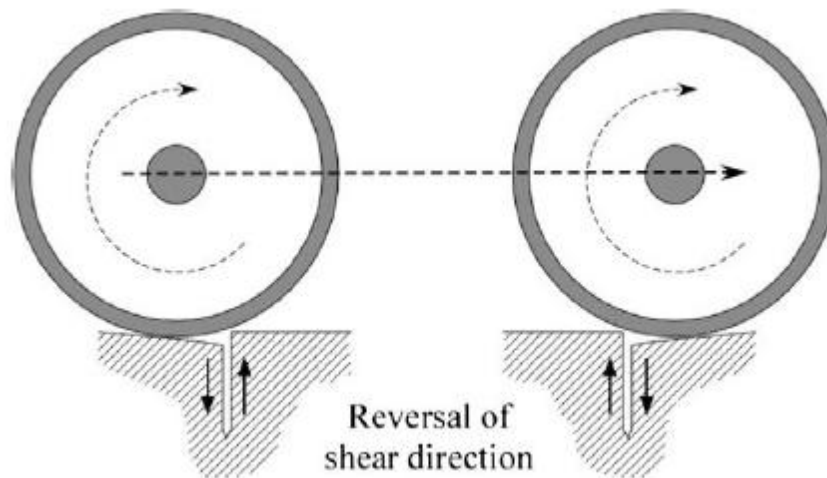


Figure 2.13. Shear loading during the wheel passage [19].

2.3.2.3. DYNAMIC EFFECTS

The wheel loads may vary at frequencies up to 10 Hz due to car motions [17]. Also dynamic responses of the ballast bed and subgrade are important [20].

The dynamic load can be modelled as statistical distribution for a static wheel load. To obtain dynamic load, static load is multiplied with a magnification factor K_{dyn} .

$$F_v(\text{dynamic}) = F_v(\text{static}) \cdot K_{dyn} \quad (5)$$

This magnification factor increases with irregularities in the rails and in the wheels such as corrugation of rails or flat spots on the wheels especially at high speeds. These irregularities can be seen from the figure 2.14.

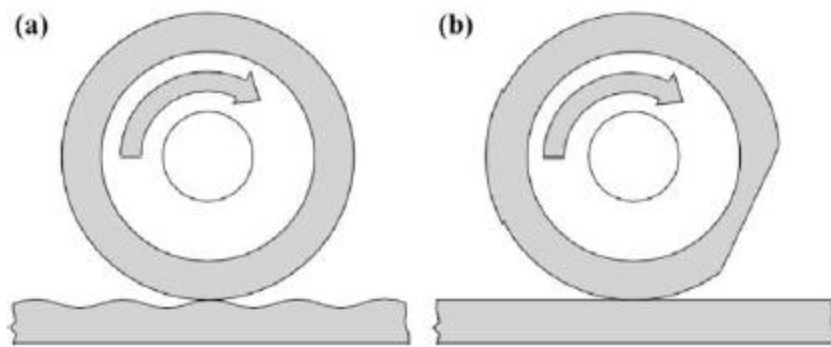


Figure 2.14. Corrugation of the rails (a). Flat spots on the wheels (b) [16].

2.3.2.4 THERMAL STRESSES

Thermal stresses occur due to difference between the neutral temperature and the service temperature. The neutral temperature of the rails can be defined as the temperature at which the longitudinal force is zero. If service temperature is higher than the neutral temperature, rails tend to expand but they cannot because they are continuously welded, then compressive stresses occur. This may cause formation of sun kinks and then buckling of the rails which lead to derailment of the train. At the temperatures lower than the neutral temperature, tensile thermal stresses which act as

additional static loading component together with the wheel loads. This tensile thermal stresses reach the highest value at cold winter nights which increases the risk of rail fracture. Thermal stress σ_T can be calculated according to formula below for continuously welded rails.

$$\sigma_T = \alpha \cdot E \cdot (T_N - T) \quad (6)$$

2.3.2.5. RESIDUAL STRESSES

Residual stresses are stresses that exist in the rail without any external loading. The origin of them is the manufacturing processes such as heat treatment, rolling, welding or the passage of the wheel on the rail. For example the latter cause to build up compressive residual stresses at the surface layer of the rails due to plastic deformation. The amount of residual stresses are measured by the destructive saw cutting and hole drilling method [21] or the nondestructive X-ray or neutron diffraction [22-23] methods. However the measurement method itself may cause the change in the residual stress in the rails. For example the accuracy of the neutron diffraction method depends on the thickness of the material, the extraction of such thin slices from the rail cause to change the three dimensional residual stress states in the rail. The extraction of thin slices from the rail can be seen from the figure 2.15.

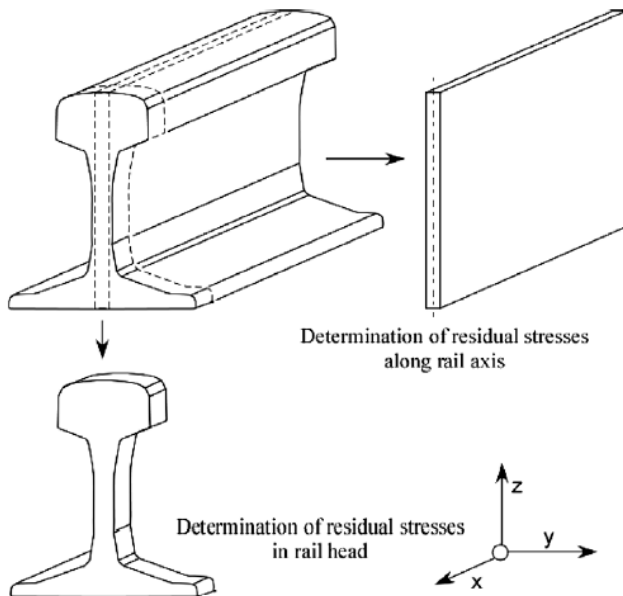


Figure 2.15. Extraction slices from the rail to measure residual stress by neutron diffraction method [16].

The amount of the residual stress in the rails can be reduced by both the modifications in the manufacturing procedure and on process parameters such as cooling rate. Cooling the rails at higher rates reduces the tensile residual stresses on the rails. The effect of the cooling rate on the residual stress is shown in the figure 2.16.

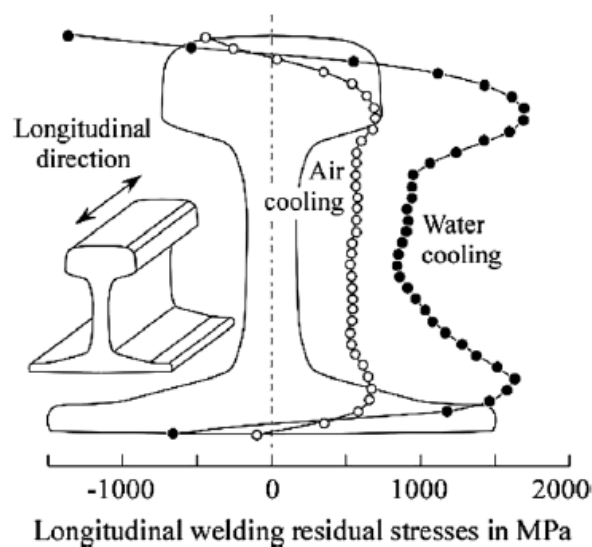


Figure 2.16. The effect of cooling rate [17].

2.4. RAIL FATIGUE

Fatigue cracks can be started at the rail head, web and foot. Propagation of initiated cracks can cause catastrophic failure of the rail.

2.4.1.1. HEAD CHECKS

Head checks are wheel rail contact defects that formed at the surface of the rail corners due to friction with an interspacing of 0.5-10 mm. This small interspacing makes them very dangerous because if one of them fails, then adjacent sections also fail which may cause derailment of the train. Failure of the rail originated from the head check is illustrated in Figure 2.17. Also they can cause spalling of the material between the two head checks which can be seen from the Figure 2.18.



Figure 2.17.Fracture due to head check [16].

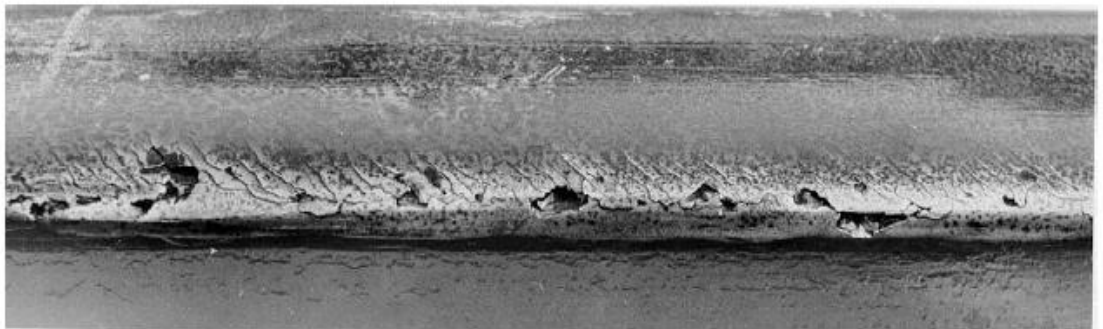


Figure 2.18. Spalling of the rail [16].

2.4.1.2. SQUATS

Squats are also wheel rail contact surface defects, not at rail corners but at flat surface of the rail. Squats form randomly at the rail surface as seen from the Figure 2.19.

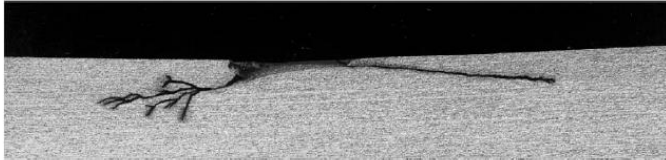


Figure 2.19. Propagation of a squat [16].

To overcome the metal removal from the surface of the rail, the wear resistance of the rail metal should be increased; however squats are especially seen at wear resistant materials. Although improvements in wear resistance increase the fatigue life of the steel and decrease the maintenance costs, the head crack formation possibility at the surface increases.

2.4.2. RAIL HEAD CRACKS WITH INTERNAL ORIGIN

2.4.2.1. KIDNEY-SHAPED CRACKS

In past days the possibility of formation of rail cracks with internal origin was the highest because of manufacturing defects. This cracks called kidney shaped cracks. The example of such a crack can be seen from the Figure 2.20.

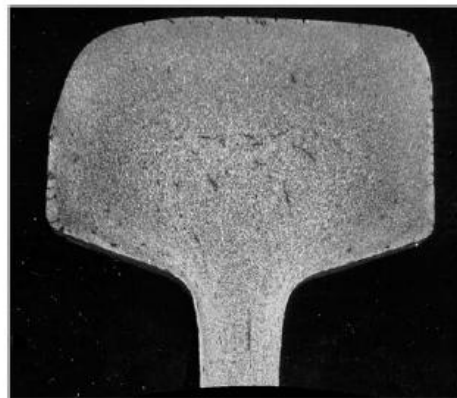


Figure 2.20. Kidney-shaped crack [16].

2.4.2.2.LONGITUDINAL CRACKS

Longitudinal cracks are horizontal cracks formed at usually 10 mm below the surface due to non-metallic inclusion band especially at gauge corners. An example of such a crack is illustrated in the figure 2.21.

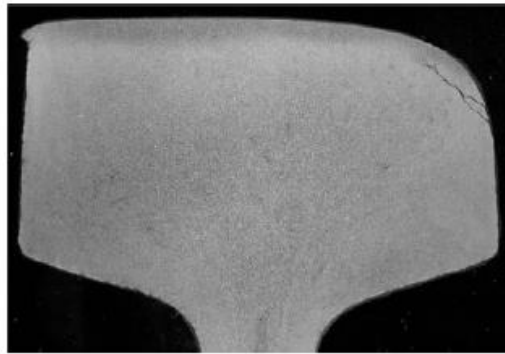


Figure 2.21.Gauge corner crack [16].

2.4.3. RAIL WEB CRACKS

2.4.3.1. LONGITUDINAL VERTICAL AND HORIZONTAL CRACKS

These cracks form due to poor manufacturing. Examples of vertical and horizontal cracks are illustrated in Figure 2.22 and Figure 2.23.



Figure 2.22.Longitudinal web crack [16].



Figure 2.23.Horizontal web crack.

2.4.3.2. CRACKS INITIATED AT MACHINED HOLES IN THE WEB

At fishbolt holes or insulation holes, crack generally initiates and propagates at an angle of 45° to the horizontal but may change its direction as it propagates. If vertical stresses cause to form crack at hole, then it can also form at 0° to the horizontal. These cracks are shown in figure 2.24. They become dangerous at the rail ends.

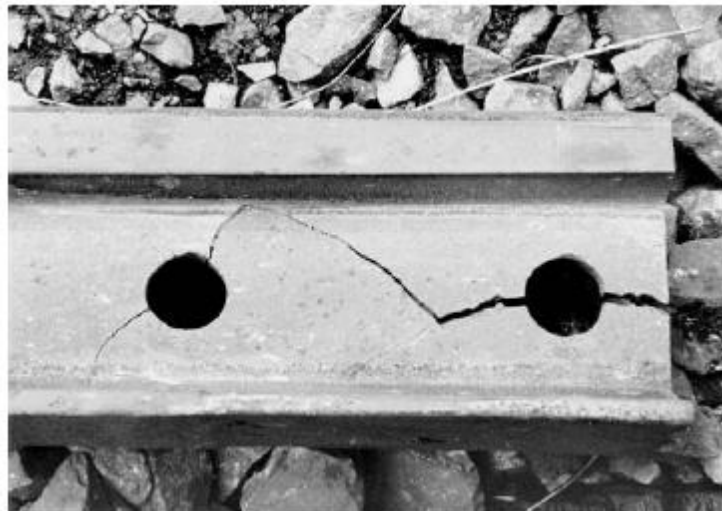


Figure 2.24. Web cracks at fishbolt hole [16].

2.5. R350 HT RAIL

With increasing the traffic and acting loads on rails, the stresses between wheel-rail interface increases. Therefore, increasing traffic and load rolling contact fatigue effects increases. To overcome this problem in the 1990 the Company Voestalpine Schienen produced a new rail so called head hardened rail (R 350HT).

A proper heat treatment followed by hot rolling results in improved rail wear property, hardness, endurance limit and strength. Head hardened rail steels have 3 times wear resistance than grade R260 and also high resistance to rolling contact fatigue defects.

In order to verify high wear resistant and high resistant to rolling contact fatigue of R350 HT, Voestalpine Schienen and DB AG set a test program to compare rail grade R220, grade R260 and grade R350 HT which were conducted on high speed and medium speed lines of DB [24].

After 3 years of installation, rails cut from place of installation which were subjected to 90 Mega Tones. Magnetic particle inspection conducted on three steel grades. Head checks in gauge corner of the rails which is one of the rolling contact fatigue defect can be seen clearly Figures 2.25 to 2.27.

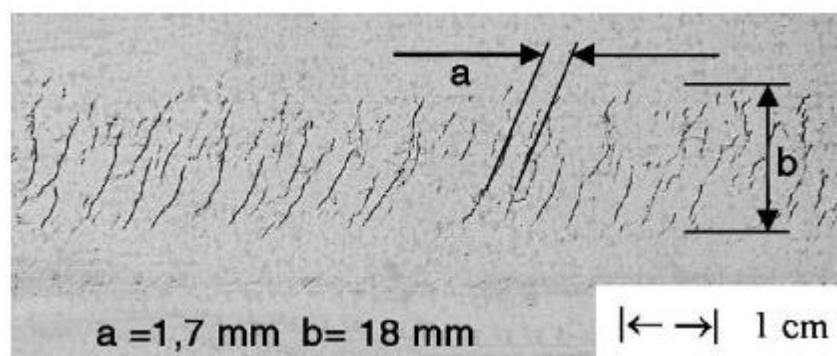


Figure 2.25.Magnetic Particle Graph of the rail grade 220 [24].

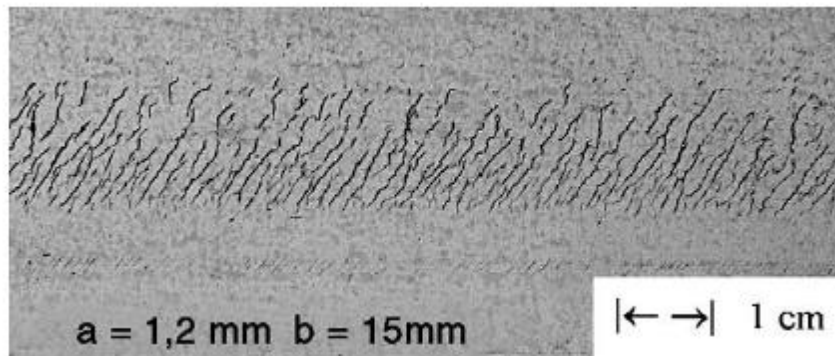


Figure 2.26. Magnetic Particle Graph of the rail grade 260 [24].

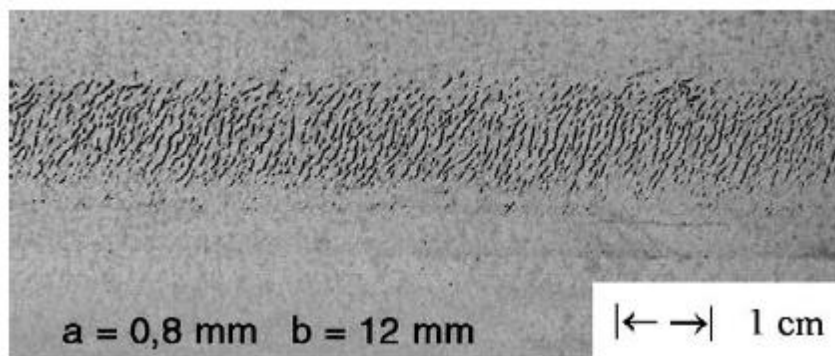


Figure 2.27. Magnetic Particle Graph of the rail grade R350 HT [24].

As a result of test, grade 220 rail has the longest head checks $b=18$ mm and widest distance to each other $a=1.7$ mm .To the contrary, head hardened rails had shortest head checks and spacing of 0.8 mm to each other.

Metallographic examination conducted on the rails. Specimens extracted from the rails R220, R260 and R350 HT measure angle of head checks and angle of head checks into the rail head. The crack growth direction is nearly same for all grades. Depth of rail damage was 2.3 mm for the grade R220 (fig 2.28), 1.3 mm for the grade R260 (fig 2.29), and 0.4 mm (fig 2.30) for head hardened rail grade.



Figure 2.28.Micro graph of grade R220 [24].



Figure 2.29.Micro graph of grade R260 [24].



Figure 2.30. Micro graph of rail R350 HT [24].

2.6. CRACK GAGE APPLICATION THEORY

There are two basic methods to measure the length of a propagating crack using electrical signals the first one is direct potential method and the second one is indirect potential method.

2.6.1. DIRECT POTENTIAL METHOD

In this method, the Compact Tension C(T) specimen with appropriate electrically insulated loading clevis which gripped into a testing machine is used. The specimen is directly induced with a constant current ($I_{\text{CONS.}}$) in the order of 10 Amps as shown in figure below. The potential (ΔU) can be monitored and measured from the selected two measuring points on the specimen (A&B) separated from each other by a distance (d) [25].

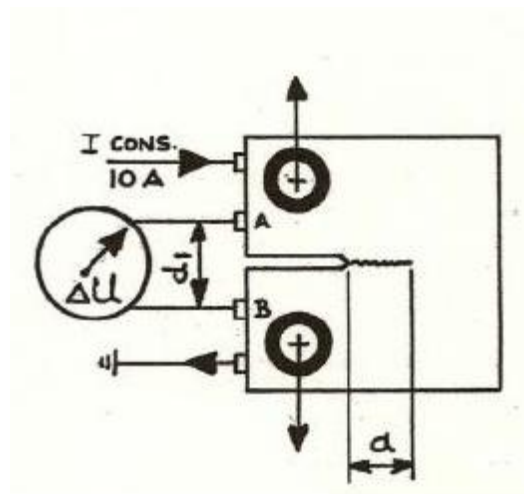


Figure 2.31. Scheme of a DIRECT POTENTIAL METHOD.

Diagram below shows a typical crack length (a) relation versus potential output (ΔU). Curves d_1 and d_2 on the diagram shows the dependency of the measuring locations on the output potential (ΔU). Diagram also shows a limited linearity

between potential output and crack length. The output voltage from the connection point of A&B having a distance d (ΔU) is very low and in the microvolt range.

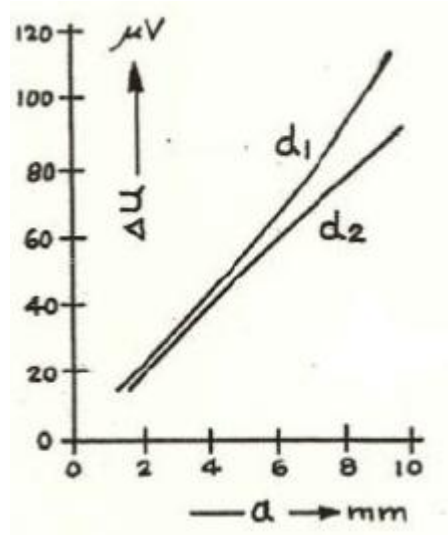


Figure 2.32.Out put potential (ΔU) versus crack length (a).

In direct potential method, materials composition can change the material conductivity and this issue causes the different output potential (ΔU). Direct potential method can be used for non-alloyed steels, aluminum and copper alloys. Naturally this method cannot be used to non-conductive materials.

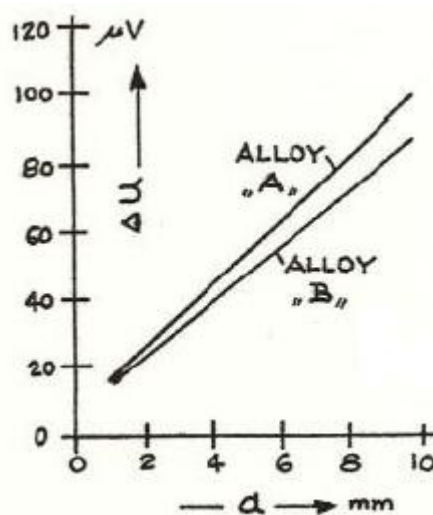


Figure 2.33.Out put potential (ΔU) versus crack length (a) for different Alloy A & B.

2.6.2. INDIRECT POTENTIAL METHOD

In indirect potential method a thin electrically insulated metal-foil (crack-gage) is glued on the specimen in a manner similar to a strain gauge. In this method While crack is propagating in the in the test specimen at the same time crack also propagate in the foil material. Basic working principle of indirect potential method is illustrated in Figure 2.34 [25].

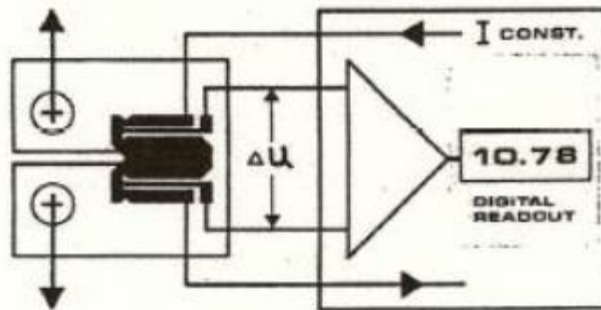


Figure 2.34. Crack-gage/fractomat working principle in indirect potential method.

This method have advantages listed below:

1. High linearity between potential output and crack-length.
2. High potential output (volts) with very low current input (mA).
3. Uniform calibration constant for all size gauges, independent of specimen geometry.
4. Independent of conductivity, size and material composition.
5. Infinite resolution, continuous DC output.
6. Static and dynamic testing.
7. Easy interface to conventional instrumentation, control circuits, and computers.
8. Small size, low mass, low cost, standard grips.
9. Adaptable to large structural elements and specimens.
10. Adaptable to environment chambers, hot cells, corrosive environments.

11. Permits automation of testing, reduction in costs, eliminates costly manual data acquisition

Lots of theoretical and experimental studies were conducted in order to get the linearity between crack length and output voltage. The final design of crack-gages is shown in Figure 2.35. Infinite length of a conductive strip was supposed to be bonded to a V notch test specimen. Constant current input (I) is excited to the strip and electrical field distribution on the strip can be shown graphically on the thin strip. At a definite distance from the left of starting notch of a specimen, a linear field line A to B distribution is existing. In this linear range, the voltage is proportional to the crack length. To the right side of the field line A to B distribution is not obeying linearity. Between points A and B a certain voltage U_0 is calculated with input of constant current.

Suppose an increase in length of the crack (Δa) from the V notch of the specimen to the right, increase in crack length (Δa) cause shifting linear range to the right side by the same amount of crack (Δa). Consequently, potential which is proportional to the length of the crack, increases with the extension of the crack by that amount. The voltage drop (U_0) in the non-linear range remains constant.

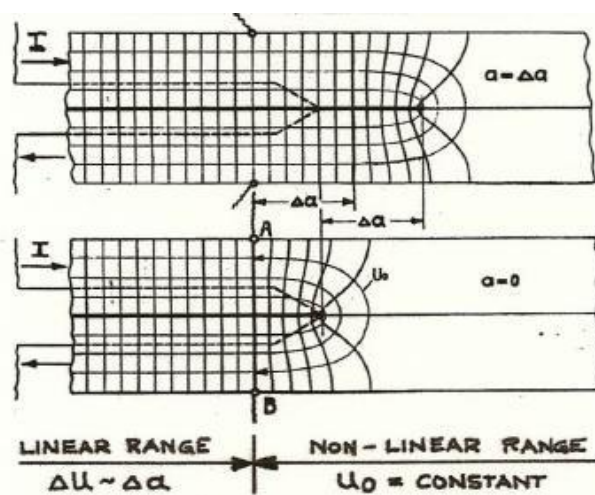


Figure 2.35.Potential distribution on a foil strip.

By using the theory discussed above various crack-gages are designed which has a reduced section, V notch comply with the test specimen notch .Various type of crack gages shown in Figure 2.36.

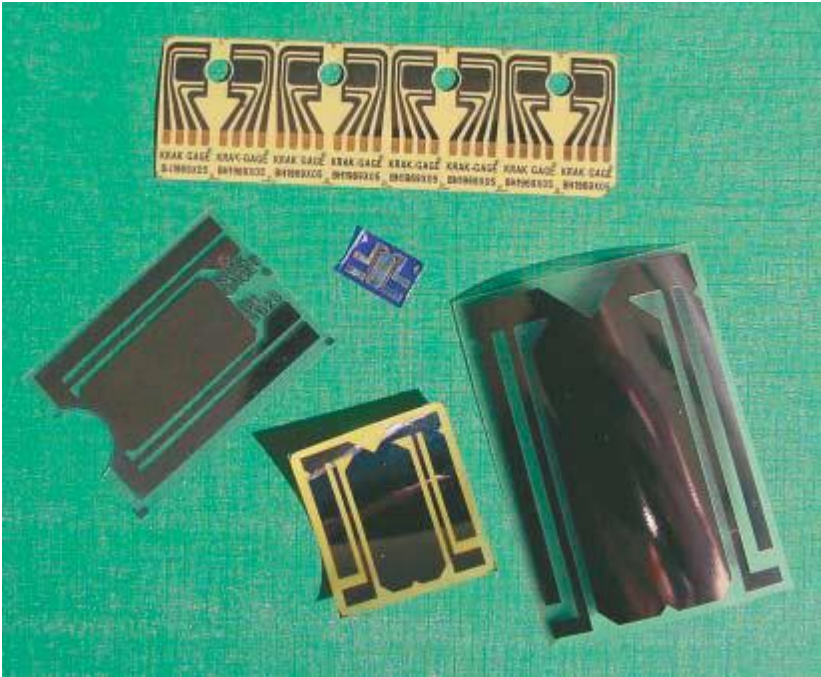


Figure 2.36. Various crack gages.

In order to investigate the propagating crack length the electronic control and readout instrument named fractomat is manufactured by RUMUL. Fractomat Control and Readout Instrument is schematically illustrated in Figure 2.37.

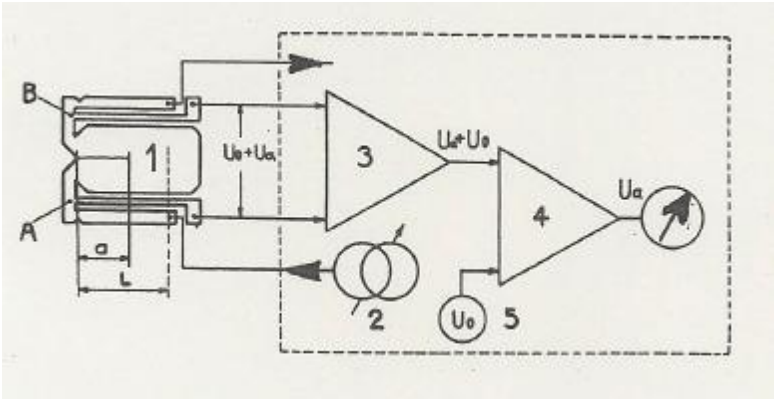


Figure 2.37. Fractomat Control and Read out instrument working principle.

The crack-gage (1) bonded on the notch specimen is excited from a constant current source (100 mA) (2). The given current to the uncracked crack-gage produces a voltage differential U_0 between points A and B on the crack-gage. By propagating the crack, the voltage rises to the total value of $U_0 + U_a$. This total voltage is available at the output of the differential amplifier (3). A second differential amplifier compensates an internal voltage U_0 so the second differential amplifier (4) illustrates only the voltage U_a which is directly proportional to the crack length. On the screen of the fractomat, the propagating crack is shown in engineering units or percentage for any given size of the crack-gage used on the specimen.



Figure 2.38. Fractomat Control and Read out instrument.

Table 3.1. Chemical composition of Rail R350 HT and R260 in weight percentages.

Rail Grade	C	Si	Mn	P	Cr	Al	V	N
R350HT	0.7808	0.4043	1.0597	0.0138	0.0292	0.0084	0.0002	0.0061
R260	0.6524	0.2386	1.0685	0.0115	0.0252	0.0070	0.0017	0.0046

Table 3.2. Chemical composition range of Rail R350 HT and R260 in weight percentages according to EN 13674-1:2003+A1:2007.

Rail Grade	C	Si	Mn	P max	Cr max	Al max	V max	N max
R350HT	0.70/0.82	0.13/0.60	0.65/1.25	0.025	0.15	0.004	0.030	0.010
R260	0.60/0.82	0.13/0.60	0.65/1.25	0.030	0.15	0.004	0.030	0.010

3.2. METALLOGRAPHY

Metallographic examinations were carried out on the samples cut from both of the steel rail grades, R350 HT and R260, from the positions which is indicated in Figure 3.2. Firstly, specimens were grinded with emery papers with grade of 220, 400, 600 and 800 in a row. After grinding, the specimens were polished using 1 μm and 0.6 μm alumina powder suspension, and subsequently etched with 0.2% nital to reveal the microstructures under optic and electron microscopy. Olympus optical microscope, NOVA NANO SEM 430 at metu and Zeiss Evo Ls 15 Scanning Electron Microscope (SEM) at Atılım University were used for microstructure examinations.



Figure 3.2. Metallographic examination specimen.

3.3. MECHANICAL TESTS

3.3.1. TENSILE TEST

Tensile properties of the R350 HT and R260 rail grades were obtained from the tensile specimens cut and machined from head of the rails, both from longitudinal and transverse direction of the rails. Tensile properties in the web of the rails were also measured on the specimens cut and machined in longitudinal direction of the rails. Tensile tests were conducted according to TS EN ISO 6892-1 standard tensile testing of metallic materials [27] on a 10 KN Instron 5582 Tensile test machine, using a strain rate of 1 mm/min at room temperature.

3.3.2. CHARPY IMPACT TOUGHNESS TEST

V-notched Charpy impact specimens machined from the head of R350 HT and R260 grade rails, in the short transverse direction, having notches parallel to transverse direction and hence perpendicular to rolling direction as seen in Figure 3.3. Charpy impact tests were carried out at 3 different temperatures; room temperature, 0 and 20 C° according to ASTM E23-12, “Standard Test Methods for Notched Bar Impact Testing of Metallic Materials” [28]. Tinius Olsen impact testing machine was used to conduct Charpy impact tests.

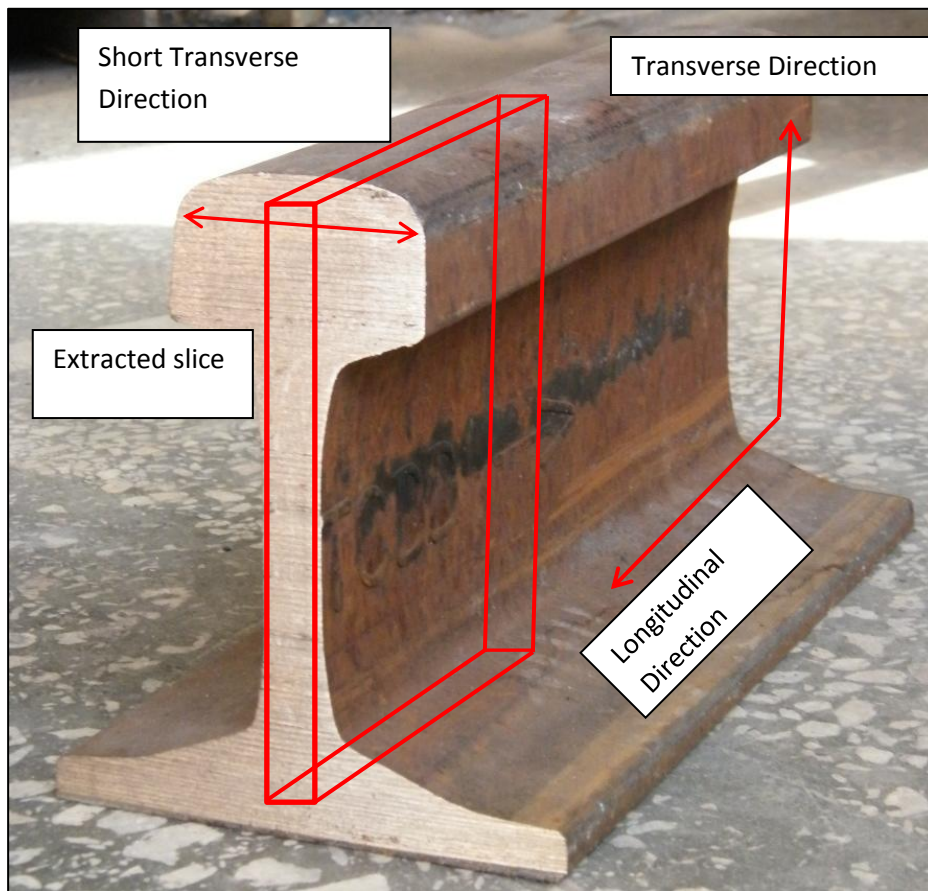


Figure 3.3. Rail brought from TCDD.

3.3.3. HARDNESS TEST

The Brinell hardness measurements on two rails R350 HT and R260 were made on the specified positions shown in Figure 3.4 as per EN 13674-1:2003+A1 standard. Brinell hardness tests were carried out on Universal Emco M4U-025 hardness testing device and in accordance with ASTM E10-12 [29]. During tests, 2.5 mm diameter tungsten carbide ball indenter used and applied for 15 s with a load of 187.5 kg.

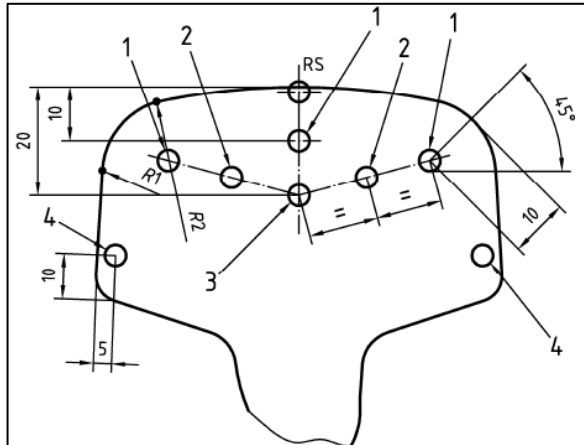


Figure 3.4. Positions of hardness testing.

3.4. COMPACT TENSION C (T) SPECIMENS

Compact tension specimens were machined from the head, web and foot of the R350HT and R260 rails for fracture toughness and fatigue crack growth rate tests. The orientations of the specimens are in the transverse direction of the rail having machined notch in transverse direction for fatigue crack growth rate and fracture toughness tests. In addition to those, compact tension specimens were machined from the web of the rail R260 only in the longitudinal direction with machined notch in the longitudinal direction for fracture toughness tests.

Compact tension specimens were machined from the slice extracted from the center of the R350HT and R260 rail fig 3.3. Fracture toughness specimens comply with all of the dimensional requirements of standard E399-09ε2 (Plane-Strain fracture toughness of (K_{IC}) metallic materials) as shown in Figure 3.5. [30]. Fracture toughness specimens with a width of $w=32$ were used. Generally, thickness $W/2$ is taken to calculate a valid fracture toughness value. In this work thickness taken as $B=16$ mm so as to get the plain strain condition which is required to carry out LEFM approach to calculate plane strain stress intensity values.

Similar to fracture toughness specimens, fatigue crack growth rate specimens were machined in transverse direction of the rail. Thickness between ranges of

$W/20 \leq B \leq W/4$ is recommended in ASTM E647-11 [31]. Specimens with dimensions of $W=40$ mm and $B=10$ mm are prepared as Figure 3.6.

A chevron starter notch was machined for fatigue crack growth tests. The detail of chevron notch is shown in Figure 3.7.

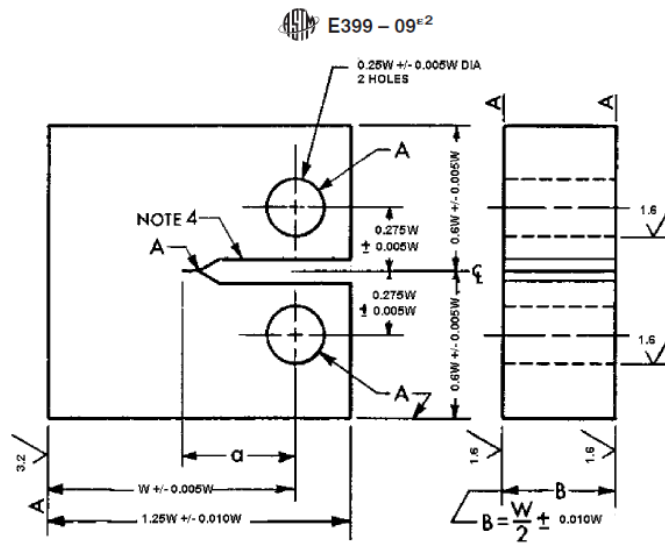


Figure 3.5. Fracture toughness compact tension specimen configuration.

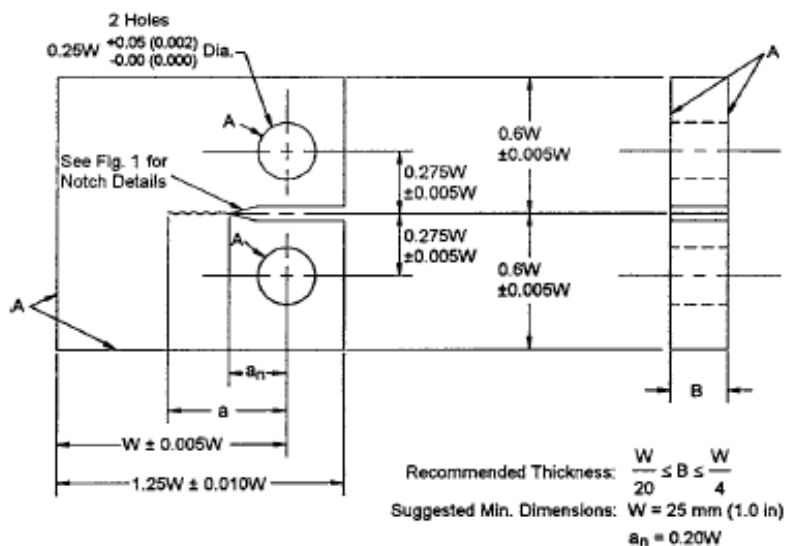


Figure 3.6. Fatigue crack growth compact tension specimen configuration.

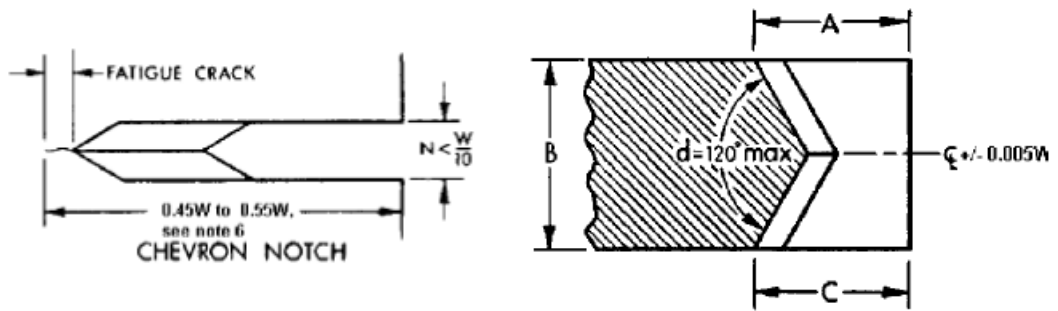


Figure 3.7. Fatigue crack chevron starter notch configuration.

In plane-strain fracture toughness test, crack mouth opening displacement (CMOD) and force data is required to conduct analysis. This data can be taken by the help of a computer data acquisition system. To record the crack mouth opening displacement, a displacement gage is required. Thus, a displacement gage was mounted to the specimen via integral knife edges as shown in Figure 3.8. The distance between the integral knife edges is 12 mm because of the working range of the displacement gage available. The dimension of the finished specimens of fracture toughness and fatigue crack growth machined from the both of the R350HT and R260 grades rails are shown in Figure 3.9.a-b

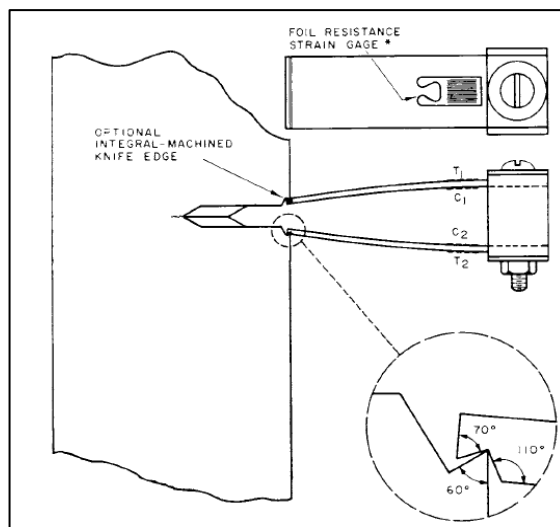


Figure 3.8. Displacement gage.

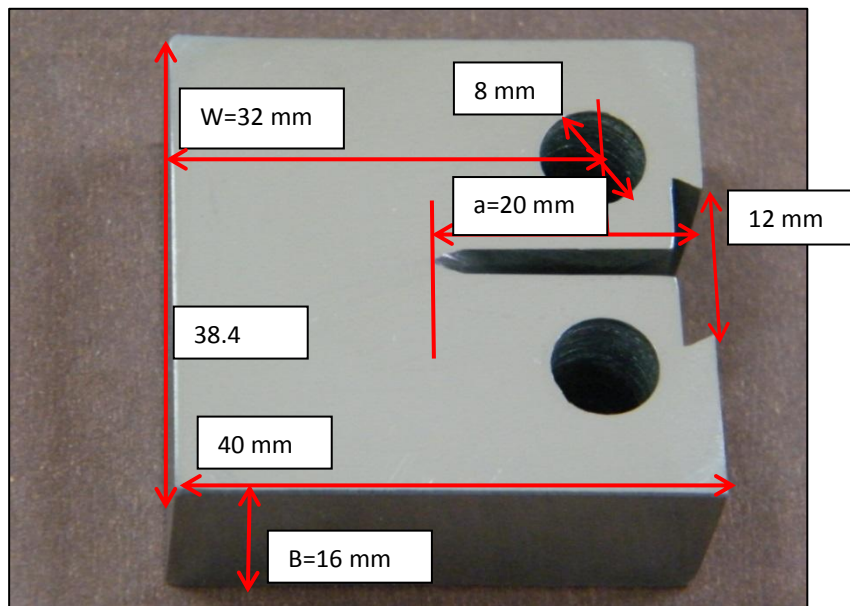


Figure 3.9. (a) Finished fracture toughness with dimension of both rail R350 HT and R260.

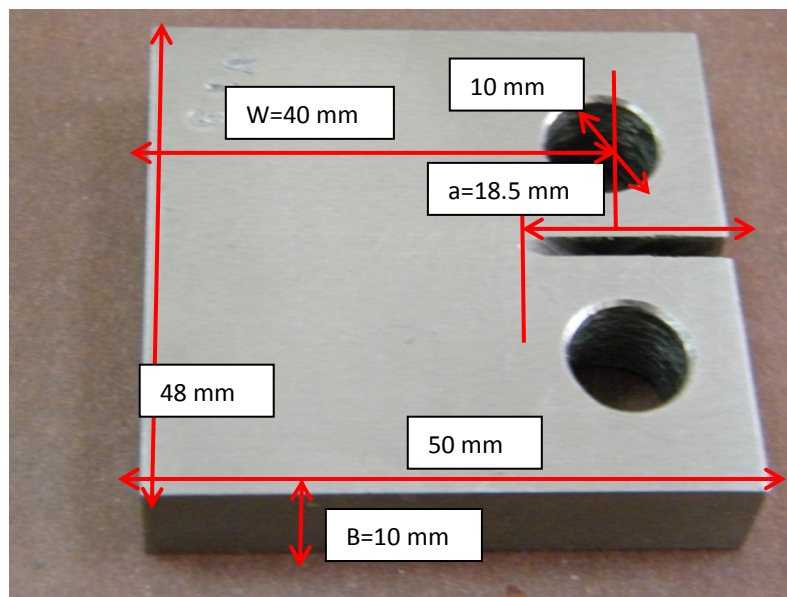


Figure 3.9. (b) Finished fatigue crack growth specimen with dimension of both rail R350 HT and R260.

3.5.COMPACT SHEAR SPECIMEN

Compact shear (fig 3.10) specimens, according to the work of Banks-Sills L. and Arcan M., were machined from the web of the rail R260 in longitudinal direction in order to conduct K_{IIc} fracture toughness of the rail. Loading frame as shown in Figure 3.11 used to conduct tests [32].

Banks-Sills L. and Arcan M. proposed that the specimens in this configuration are subjected to a pure shear stress field at the region between DD and DD of the specimen as shown in the figure 3.10 and pure shear stress is applied to the specimen by the loading frame shown in Figure 3.11. Straight-through notch for fatigue precracking is used in the compact shear specimen as shown in Figure 3.12

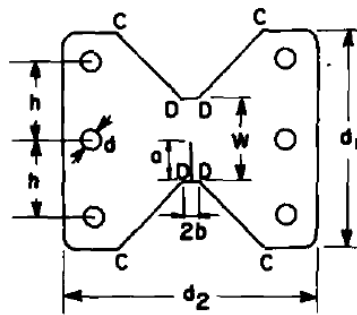


Figure 3.10. The compact shear specimen [32].

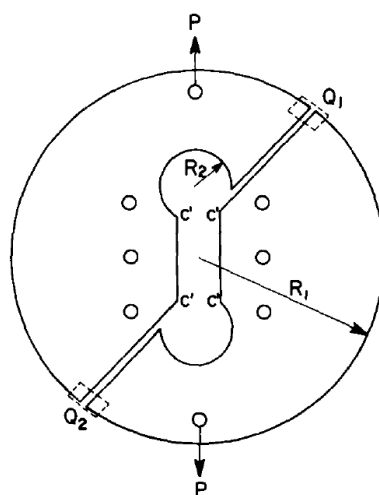


Figure 3.11. Loading frame ($R_1=95\text{mm}$, $R_2=20\text{mm}$) [32].

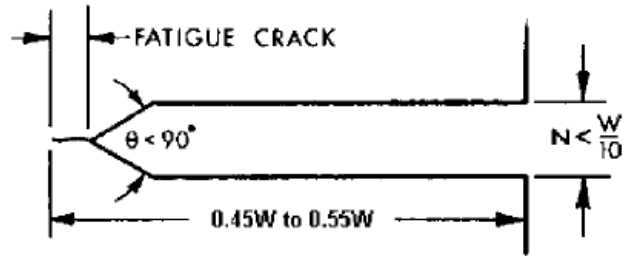


Figure 3.12. Straight through notch.

The details of the technical drawings of compact shear specimens and the loading frame are provided in Figures 3.13 and 3.14.

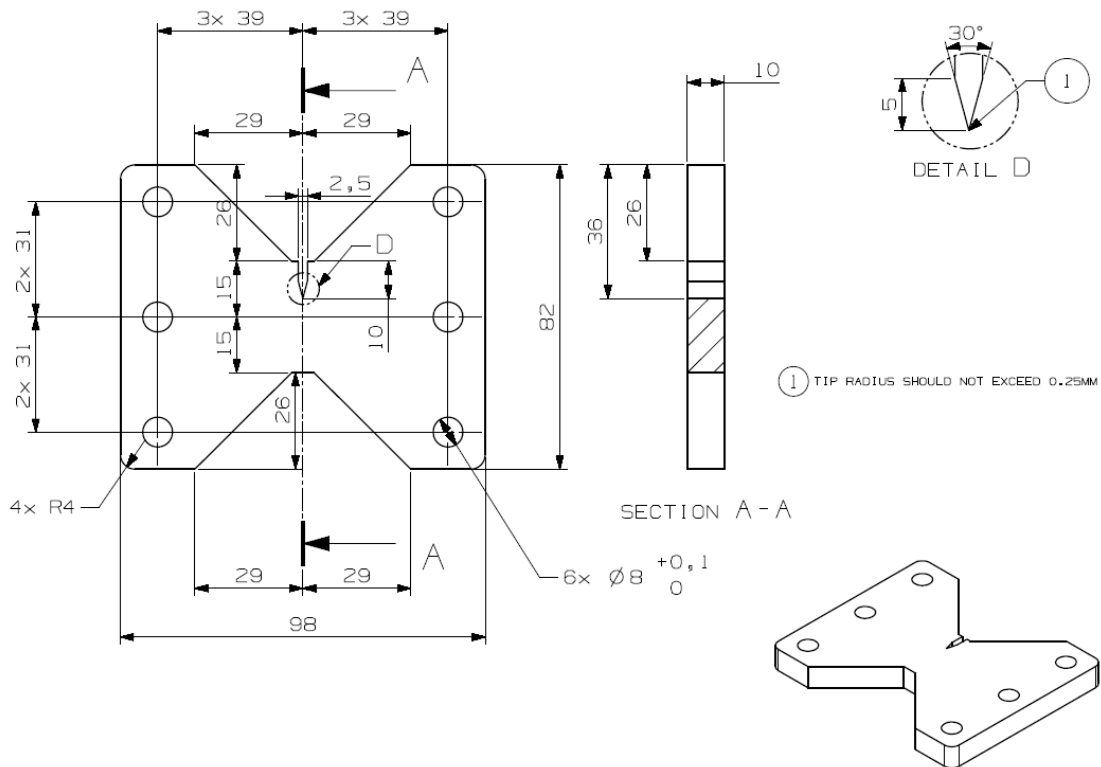


Figure 3.13. Compact shear specimen technical drawing.

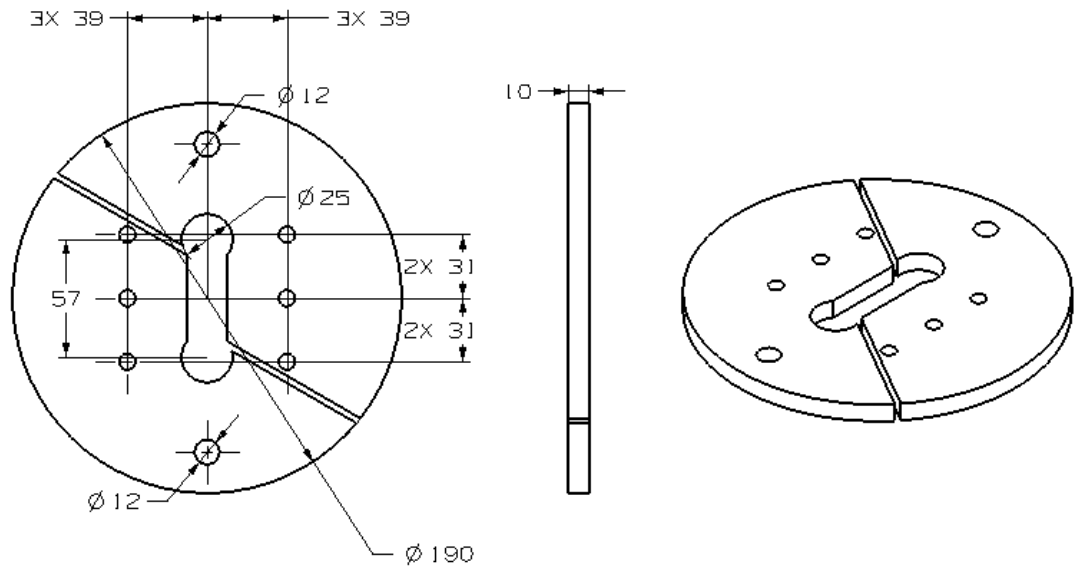


Figure 3.14. Loading frame Technical drawing.

Specimens were machined on a CNC machine and the finished specimen is shown in Figure 3.15.

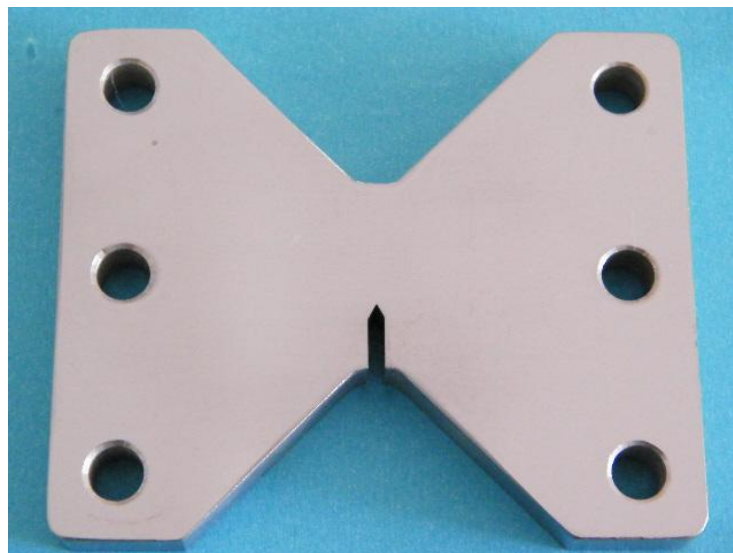


Figure 3.15. The compact shear specimen.

To conduct K_{IIC} fracture toughness test on shear specimen, shear specimen is cyclically loaded in Mode I condition (fig 3.16) according to Banks-Sills and Arcan M. until crack length is within $0.45W$ to $0.55W$. The force required for fatigue pre-cracking calculated from the equation below [32].

$$K_I = \frac{P \sqrt{\pi a}}{Wt} \left(5.528 - 42.29 \frac{a}{W} + 159.8 \frac{a}{W}^2 - 254.1 \frac{a}{W}^3 + 162.5 \frac{a}{W}^4 \right) \quad (1)$$

Where,

- P : precrack load
- t : Specimen thickness
- W : Specimen width
- a : Crack length

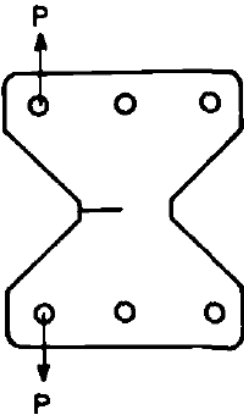


Figure 3.16. Precracking shear specimen in mode I condition [32].

When fatigue crack is reached to the specified length, cyclic loading is finished. Subsequently, shear specimen is inserted into the loading frame (fig 3.11) to conduct K_{IIC} fracture toughness testing. Specimen in the loading frame is loaded statically at a rate of 0.5 kN/sec until the specimen fractures. Forces versus displacement data are plotted and, data evaluation is done similar to the method given in ASTM E399. The value of fracture toughness is calculated by the formula below:

$$K_{II} = \frac{P \sqrt{\pi a}}{Wt} \left(1.006 - 0.313 \frac{a}{W} + 3.344 \frac{a}{W}^2 - 6.691 \frac{a}{W}^3 + 5.649 \frac{a}{W}^4 \right) \quad (2)$$

Where

P : Load

t : Specimen thickness

W : Specimen width

a : Crack length

3.6. TEST EQUIPMENT

Fracture toughness and fatigue crack growth rate tests conducted on a 10 ton MTS 810 servo-hydraulic dynamic (fig 3.17) testing machine. In fracture toughness tests, the crack growth was monitored by traveling microscope with sensitivity of ± 0.1 mm. The MTS CMOD displacement gage is used in final static loading of the specimen.

Crack (strain) gages are used for the measurement of crack length during fatigue crack growth.



Figure 3.17. MTS 810 servo-hydraulic dynamic testing machine.

3.7. TESTING AND DATA ACQUISITION

In order to conduct FCG test, a clevis and pin assembly (fig 3.18) was used at the top and bottom of the specimen which was gripped by hydraulic unit of the MTS 810 testing machine.

Fatigue crack propagation tests were conducted in a laboratory environment and at room temperature. Specimens were first pre-cracked until the requirement of ASTM E647-11[3-6] was satisfied. After pre-cracking, fatigue crack propagation tests were carried out at a constant force amplitude for fatigue crack growing at a rate of greater than $da/dN > 10^{-8}$ m/cycle. Specimens were tested at a constant force (ΔP) and a fixed set of stress ratio ($R=0.1$) with tensile-tensile sinusoidal loading at frequencies of 5 and 10 Hz.

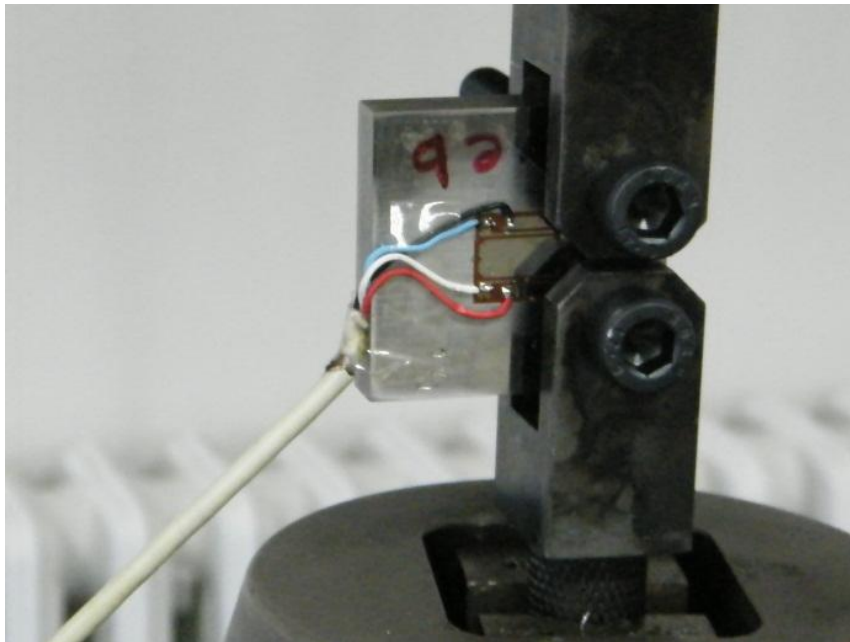


Figure 3.18. Clevis and pin assembly for fatigue crack growth propagation test.

FCGs were measured by the use of crack foils, trade marked as krack gage by Rumul Company, glued to single side of the CT specimens. Among many available crack gage sizes, A10 size was used as it was suitable to the specimen dimensions used in the study and this size is suitable up to 10 mm crack length measurement. Crack gages were glued by 270 Z Schnellklebstoff to the side of the specimen, aligned precisely from the machined notch. Firstly, specimen surfaces were grinded with emery papers with grade of 220, 400 and 600. Then surface of specimens were cleaned with alcohol to remove any contamination. Afterwards, the glue was poured on the side of the specimen and distributed evenly on the specimen with PVC spatula. Lastly, crack gage was positioned to the machined notch properly and pressed by hand by the help of a Teflon foil for 2 minutes. Specimen preparation and crack foil installation steps can be seen from the figure 3.19. After this, specimen was placed in to a specially designed gluing tool. Gluing tool (fig 3.20) provides uniform pressing on crack gage to prevent any air bubbles between the gage and specimen. Specimen was hold pressed by gluing tool for 30 minutes and then taken from the gluing tool for the soldering of wires.



Figure 3.19. Crack foil installation process on the specimen.



Figure 3.20. Gluing tool apparatus.

Resistivity of crack gage changes as crack propagates and the values sent to Fractomat which transforms data to crack lengths with an accuracy of 0.1 mm. Communication between crack foil and Fractomat is via wiring established between the two as shown in Figure 3.21.

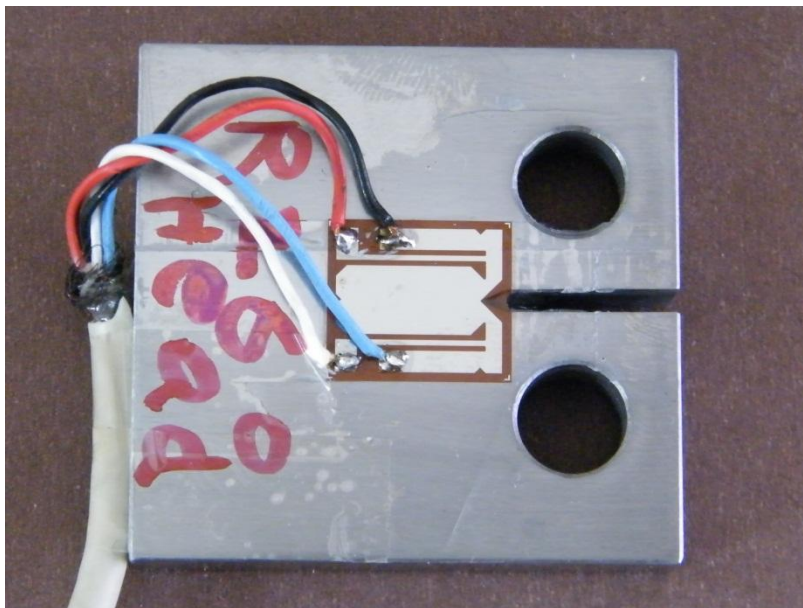


Figure 3.21. Compact tension specimen with crack gage and transferring data cables.

CHAPTER 4

RESULTS AND DISCUSSION

Optic and electron metallographic microstructures in two different magnifications are provided in the following figures, for both R350 HT and R260 specimens. Figures 4.1 to 4.4 provide optical micrographs of R350 HT and R260, whereas Figures 4.5 to 4.8 are the SEM micrographs of the same.

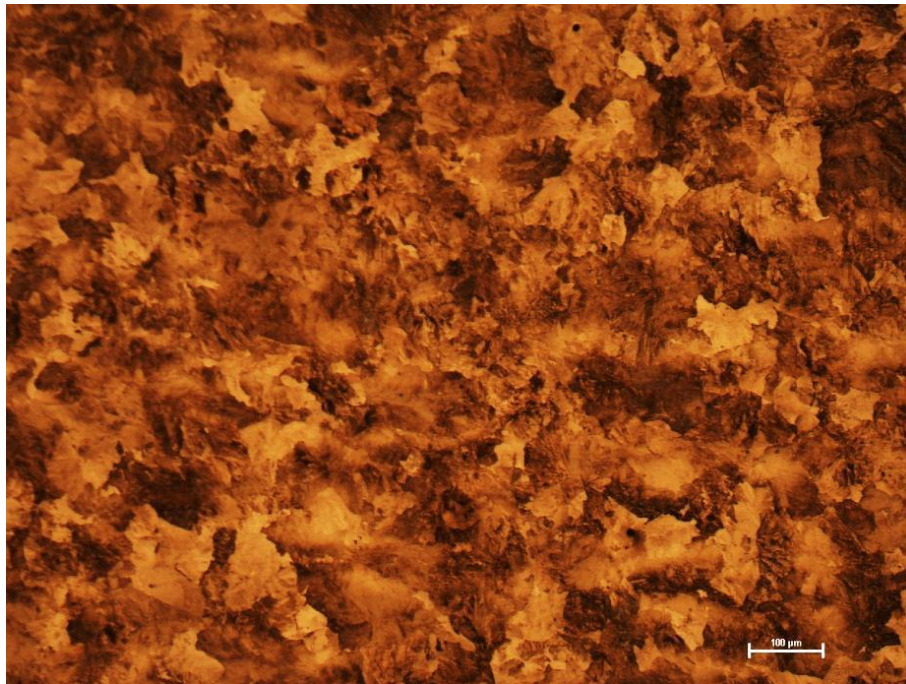


Figure 4.1. Microstructure of rail R350 HT (a) head : Structure is pearlite,
Magnification: 100X

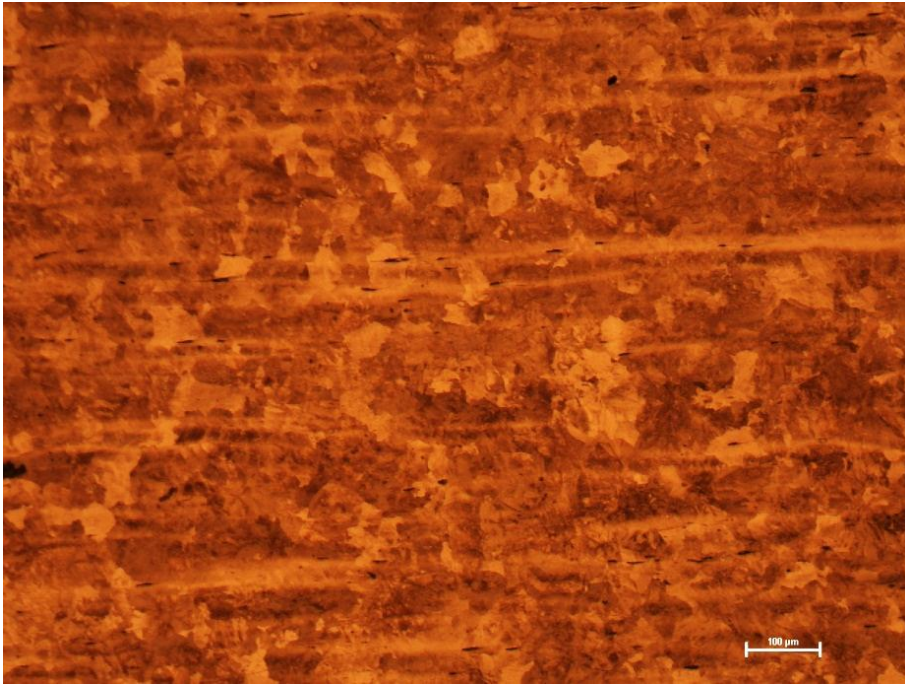


Figure 4.1. Microstructure of rail R350 HT (b) web: Structure is pearlite, Magnification: 100X

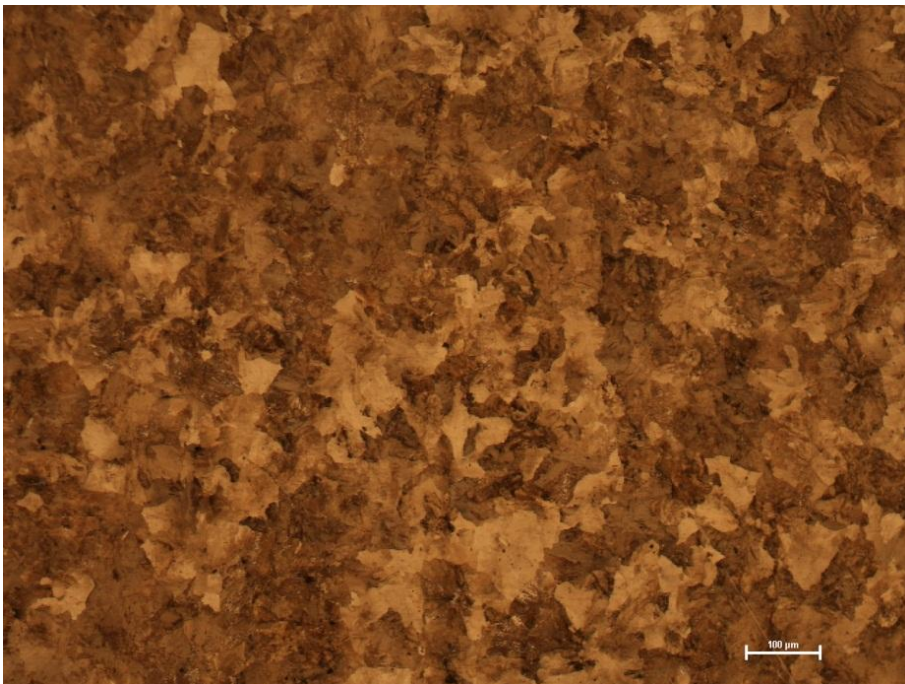


Figure 4.1. Microstructure of rail R350 HT (c) foot: Structure is pearlite, Magnification: 100X

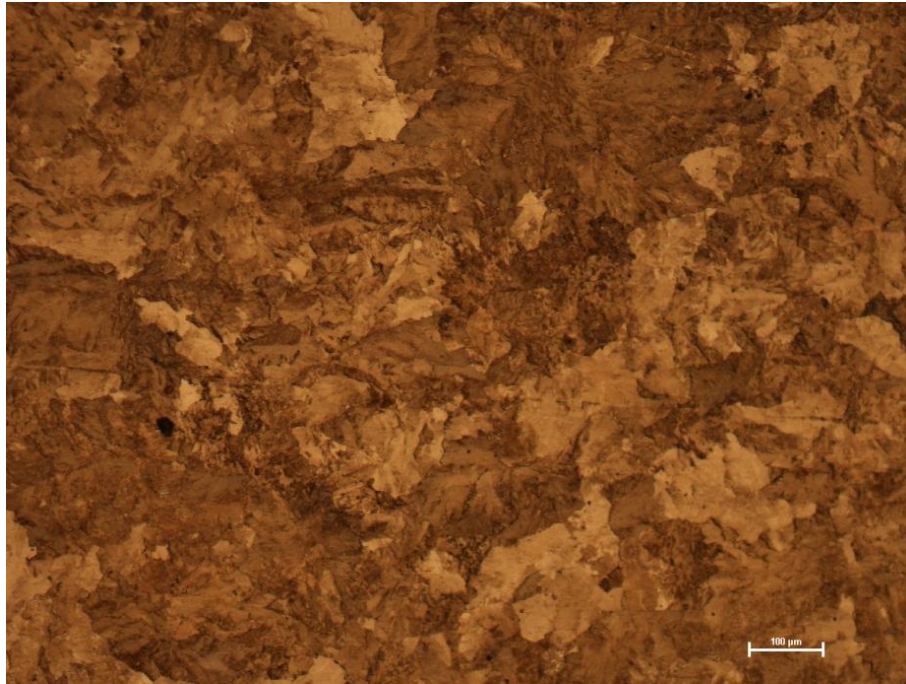


Figure 4.2. Microstructure of rail R260 (a) head: Structure is pearlite, Magnification: 100X

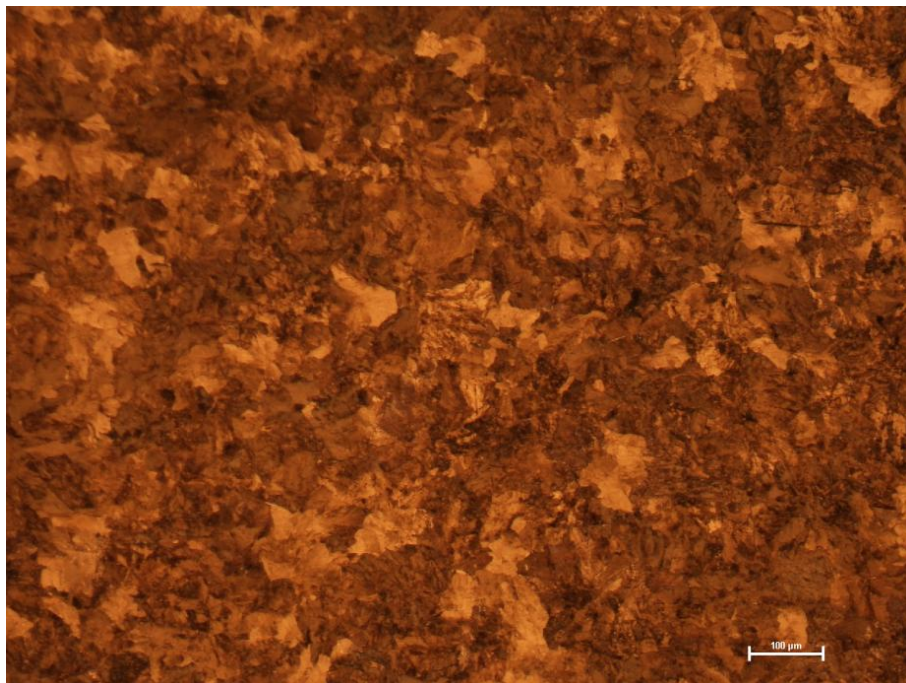


Figure 4.2. Microstructure of rail R260 (b) web: Structure is pearlite, Magnification: 100X

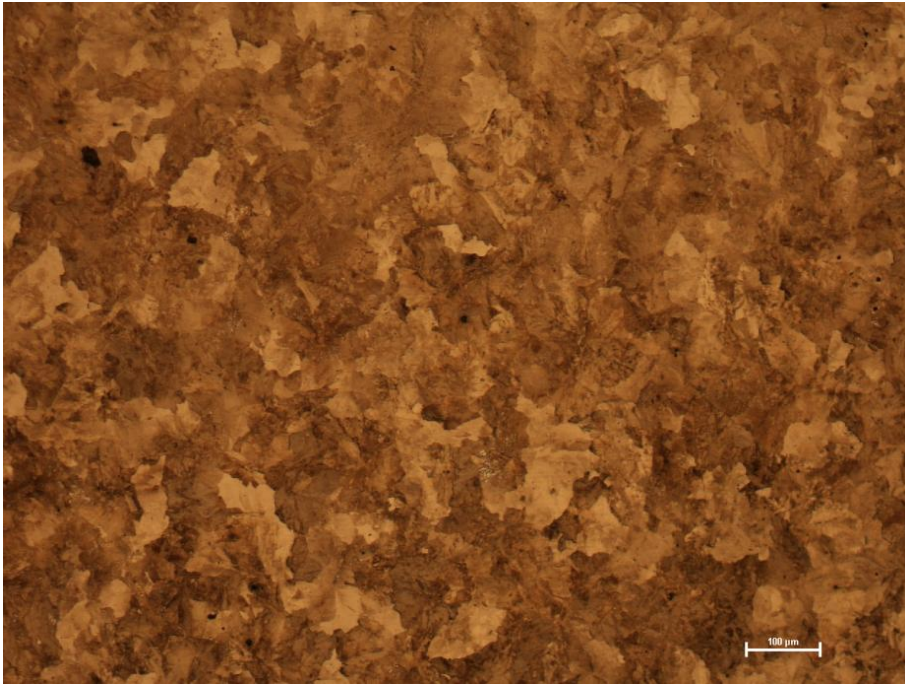


Figure 4.2. Microstructure of rail R260 (c) foot: Structure is pearlite, Magnification: 100X

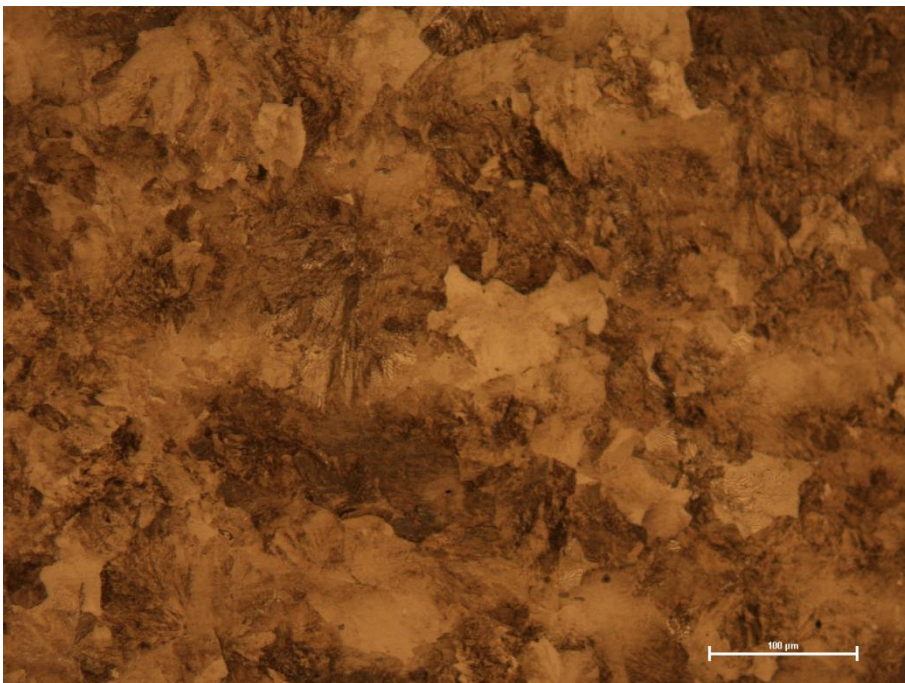


Figure 4.3. Microstructure of rail R350 HT (a) head : Structure is pearlite, Magnification: 200X

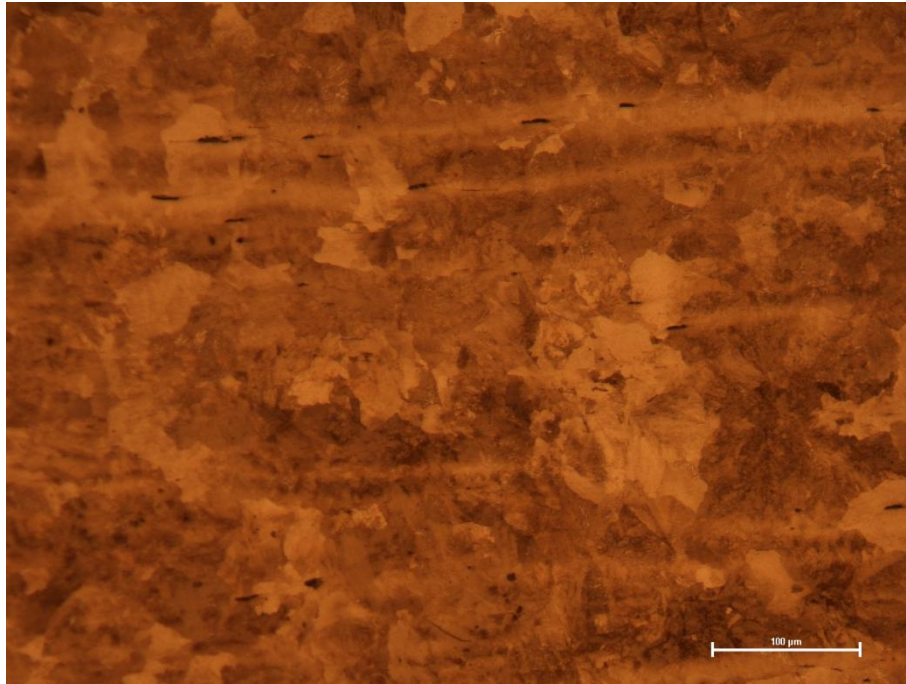


Figure 4.3. Microstructure of rail R350 HT (b) web: Structure is pearlite, Magnification: 200X

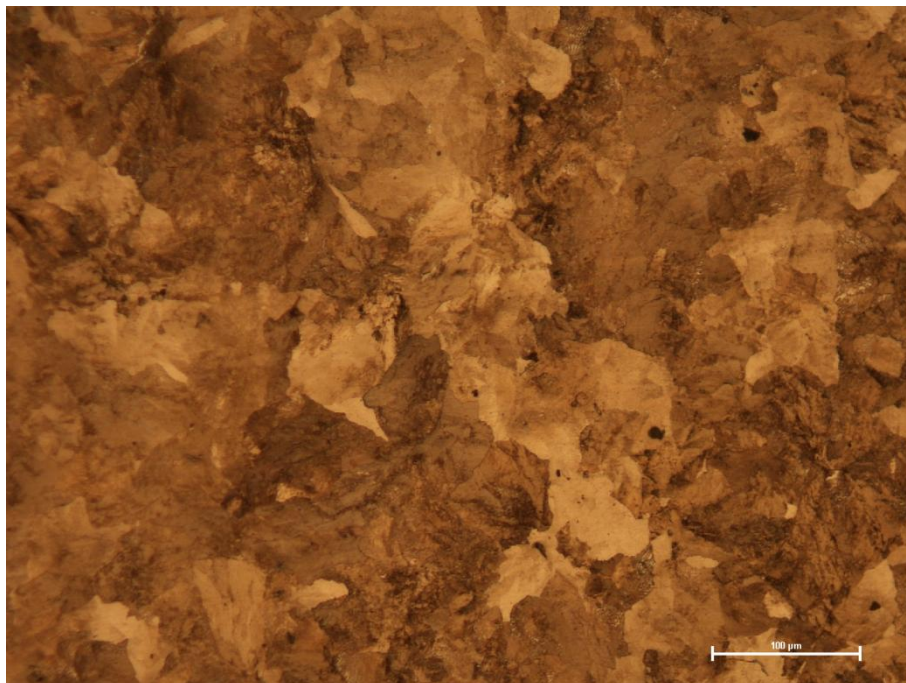


Figure 4.3. Microstructure of rail R350 HT (c) foot: Structure is pearlite, Magnification: 200X

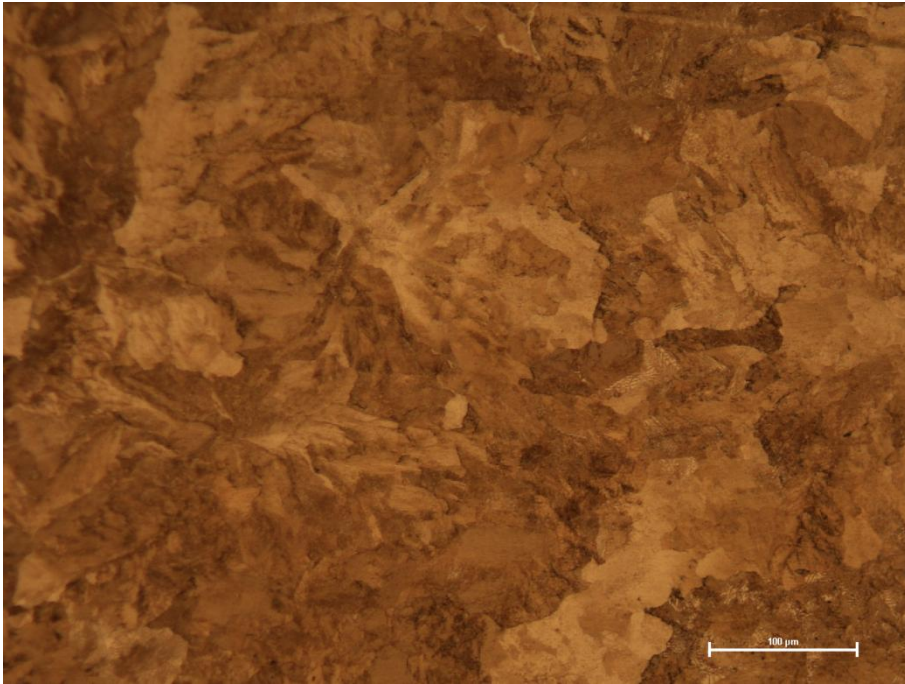


Figure 4.4. Microstructure of rail R260 (a) head: Structure is pearlite, Magnification: 200X

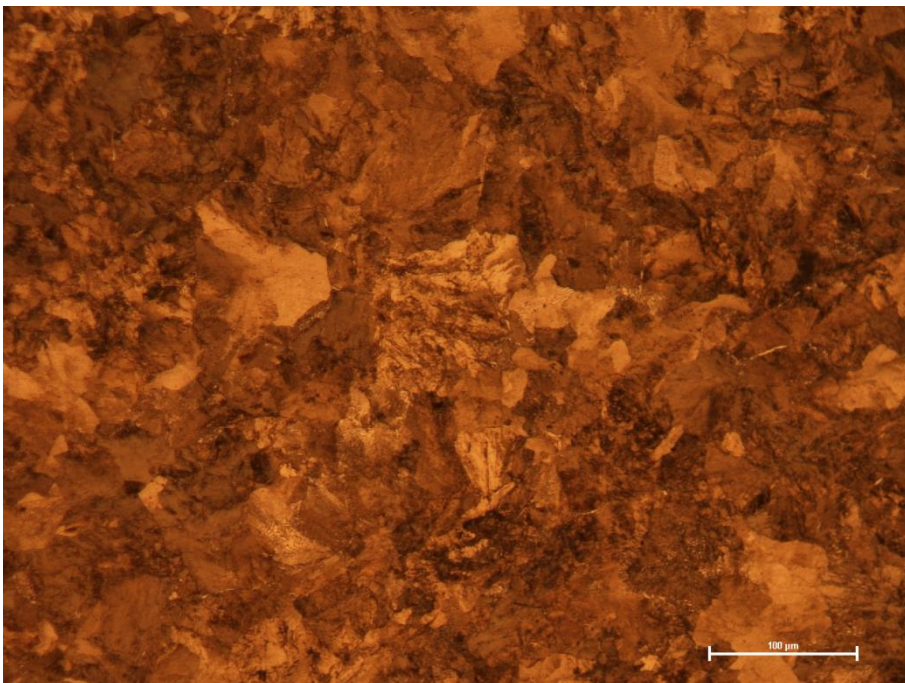


Figure 4.4. Microstructure of rail R260 (b) web: Structure is pearlite, Magnification: 200X

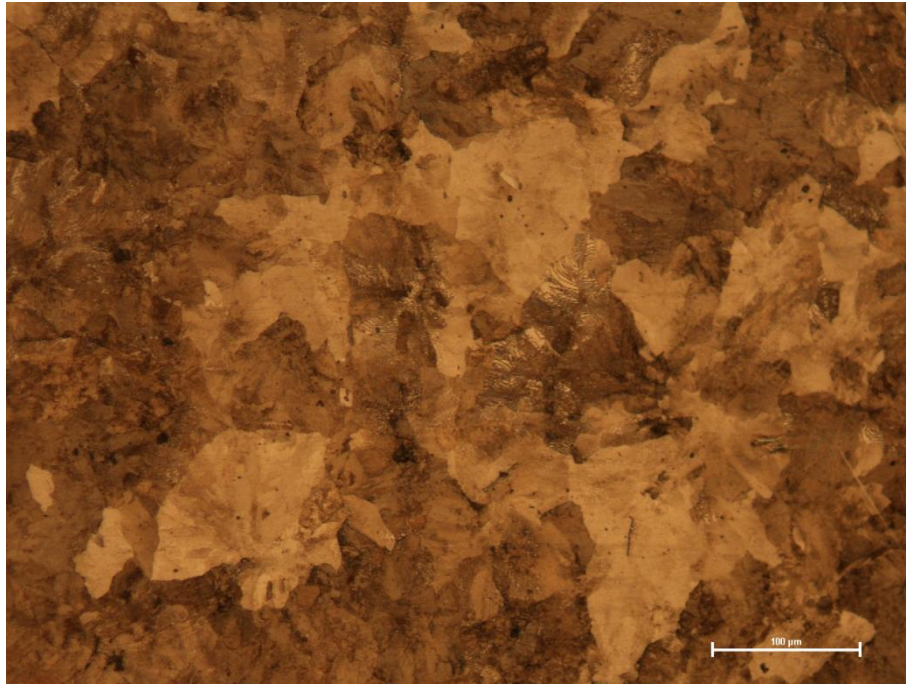


Figure 4.4. Microstructure of rail R260 (c) foot: Structure is pearlite, Magnification: 200X

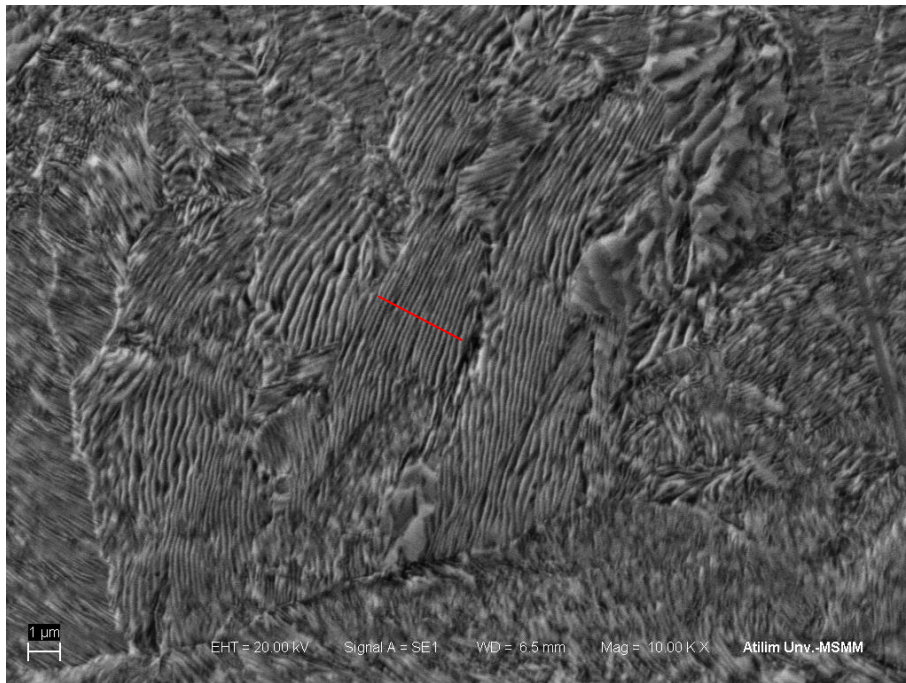


Figure 4.5. Microstructure of rail R350 HT head: Structure is pearlite, Magnification: 10000X

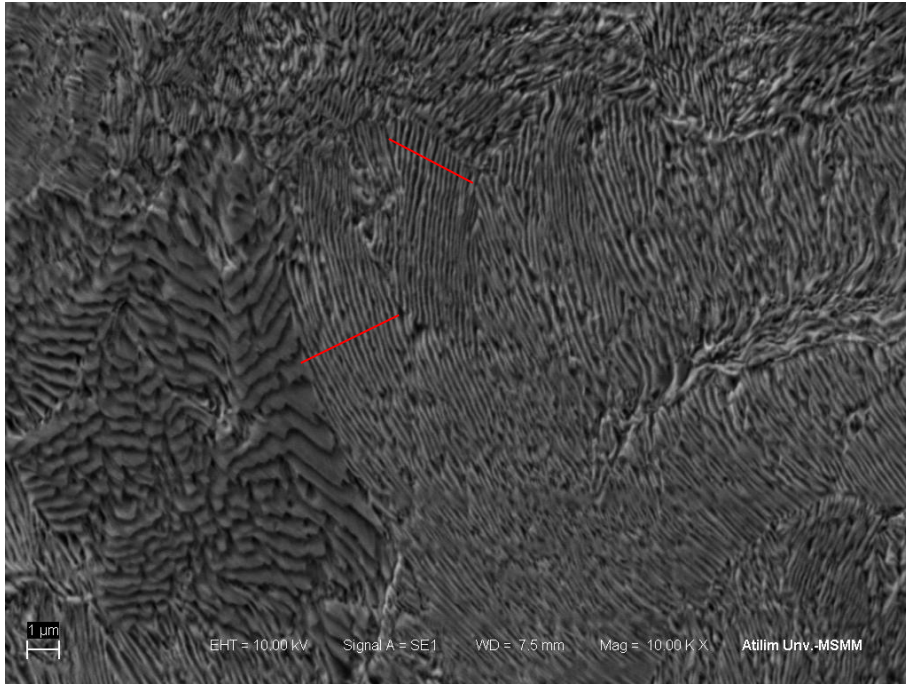


Figure 4.6. Microstructure of rail R350 HT head: Structure is pearlite, Magnification: 10000X

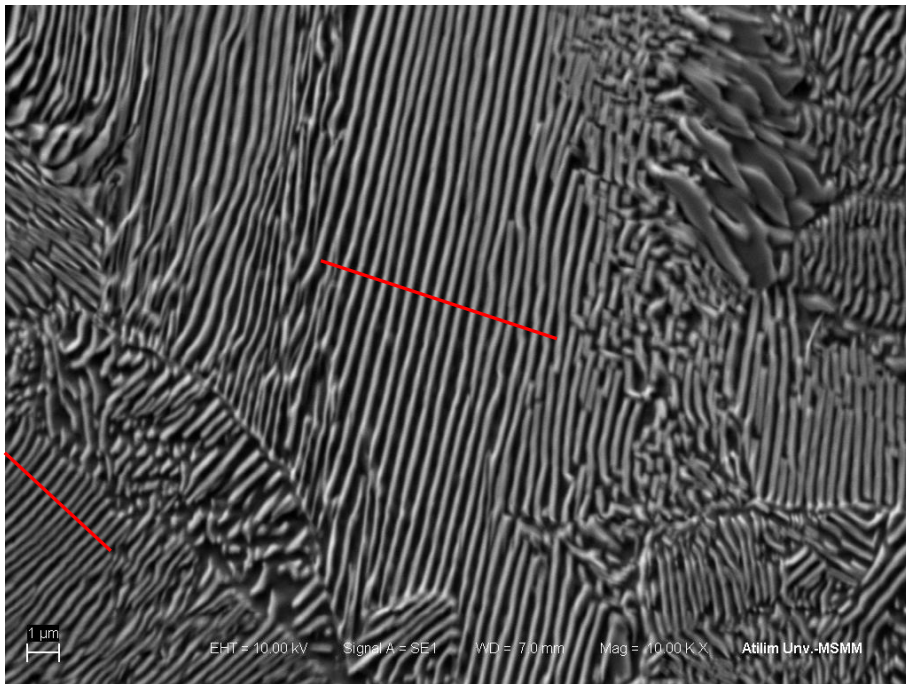


Figure 4.7. Microstructure of rail R260 head: Structure is pearlite, Magnification: 10000X

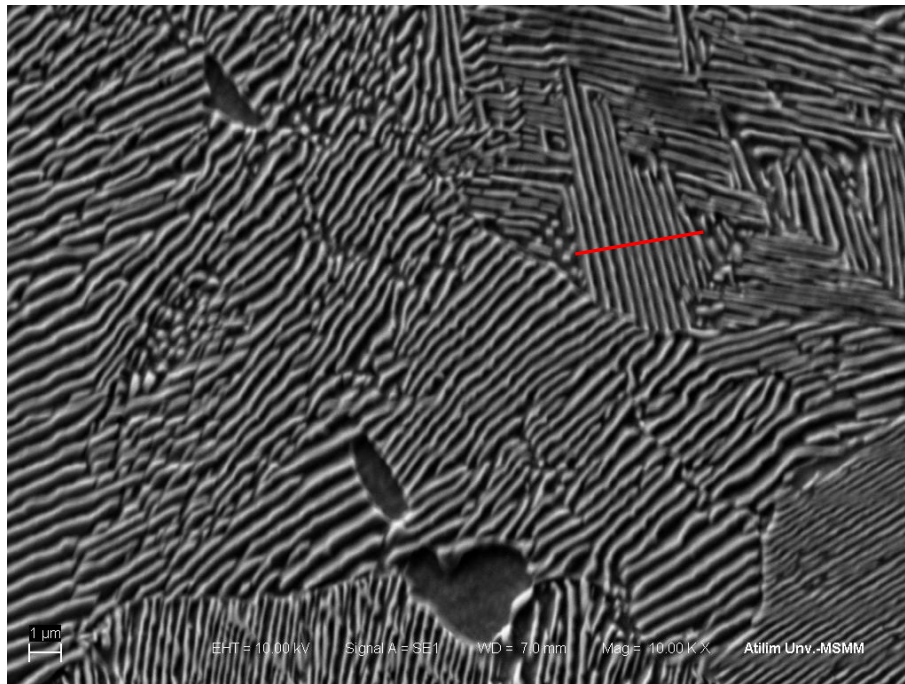


Figure 4.8. Microstructure of rail R260 head: Structure is pearlite, Magnification: 10000X

As shown in Figures 4.1 to 4.8, the microstructures of both rails R350 HT and R260 are fully pearlitic. The microstructure of rail R260 is coarse pearlite since transformation from austenite to pearlite takes place at relatively higher temperatures for R260, and thus diffusion rates are higher and carbon atoms can diffuse long distances which cause formation of thicker lamella of ferrite (α) and Fe_3C phases. The microstructure of R350 HT is fine pearlite since diffusion rate decreases with decreased pearlite transformation temperature and carbon atoms cannot diffuse long distances so layers of ferrite (α) and Fe_3C are thinner. The thick lamellar structure of R260 (fig 4.7) and thin lamellar of R350 HT (fig 4.6) rail are quite obvious in SEM micrographs at a magnification of 10000.

Inter-lamellar spacing of rails R350 HT and R260 calculated at 10000 X magnification from the three grains on which a red line was shown. In each grain a line was drawn and the numbers of ferrite (α) and Fe_3C lamella were counted and the distance between lamellae in the grain was measured. Dividing the distance of the

lamellar structure to the number of lamellae gives inter-lamellar spacing. Table 1 summarizes results of these measurements.

Table 4.1. Inter-lamellar spacing of R350 HT and R260.

Rail Grade	Inter-Lamellar Spacing at Different Grains (nm)			Average Inter-Lamellar Spacing (nm)
	R350 HT	87.08	88.23	83.60
R260	144.24	201.85	152.69	166.26

Average inter-lamellar spacing of rail R350 HT is about half of the average inter lamellar spacing of rail R260. So, smaller inter lamellar spacing results in higher strength in R350HT.

4.2. MECHANICAL TEST RESULTS

4.2.1. TENSION TEST

Machined tensile specimens from the head and web of R350HT (fig 4.9-a) and R260 rails were tested according to the TS EN ISO 6892-1 in the INSTRON 5582 Tensile-compression testing machine so as to determine mechanical properties. Attachable optical extensometer used in some of the tensile specimens to determine accurate % elongation. Results of the tensile tests are shown in table 4.2 and 4.3. Tensile stress versus axial strain diagram of Rail R350 HT specimen machined from the head in the longitudinal direction is given in Figure 4.9-b.

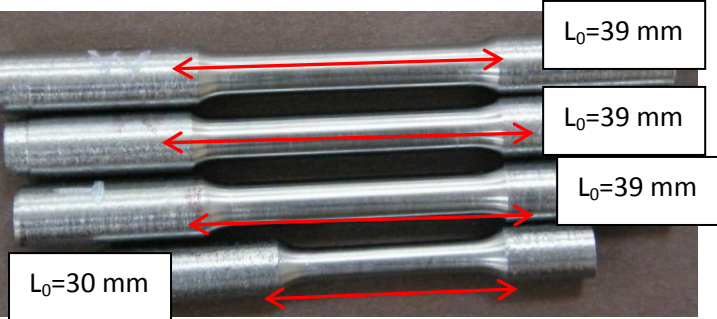


Figure 4.9. (a) R350 HT tensile specimens

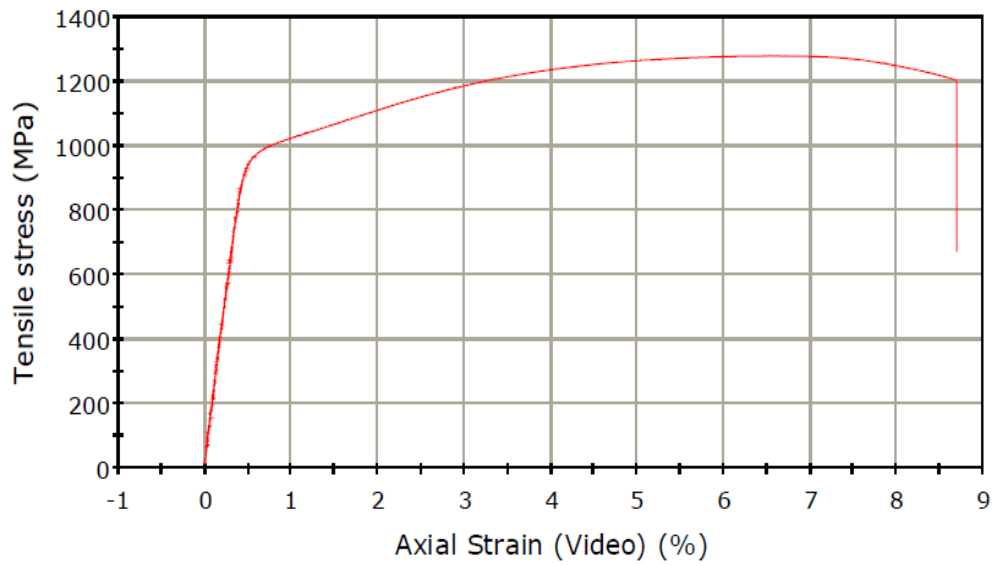


Figure 4.9. (b) Tensile stress versus Axial strain diagram of head of rail R350 HT.

Table 4.2. Tensile results of R350HT rail.

Specimen No.	Initial Diameter D_o (mm)	Initial Length l_o (mm)	Yield Strength $R_{p0.2}$ (MPa)	Tensile Strength R_m (MPa)	Percent Elongation A (%)	Percent Reduction in Area Z (%)
R350HT- Longitudinal Direction Head 1	7.8	39	740	1194	11.1	24.6
R350HT - Longitudinal Direction Head 2	7.9	39	984	1278	9.0	20.7
R350HT - Longitudinal Direction Web 1	7.8	39	605	999	9.7	21.2
R350HT - Transverse Direction Head 1	5.9	30	755	1079	20.4	23.7

Table 4.3. Tensile results of R260 rail.

Specimen No.	Initial Diameter D_o (mm)	Initial Length l_o (mm)	Yield Strength $R_{p0.2}$ (MPa)	Tensile Strength R_m (MPa)	Percent Elongation A (%)	Percent Reduction in Area Z (%)
R260-Longitudinal Direction Head 1	8.0	40	597	940	18.3	17.3
R260-Longitudinal Direction Head 2	7.0	35	645	921	18.6	17.7
R260-Longitudinal Direction Web 1	8.0	40	473	907	13.7	19.6
R260-Transverse Direction Head 1	5.4	27	654	926	18.3	17.3

According to the results, tensile properties of R350 HT in the head have yield strength and tensile strength greater than that of R260 in all directions. These high mechanical properties can be related to the grain size of the R350 HT rail since average pearlitic grain size and inter-lamellar spacing of the R350 HT rail is much lower than those of R260 and, according to the Hall-Petch equation, with decreasing grain size yield strength increases [33] as there are more barriers to dislocation motion. In return, percent elongation of R350HT is less than that of R260 as tabulated in Table 4.3 and 4.4.

4.2.2. CHARPY IMPACT TEST RESULTS

Six V-notched charpy impact specimens machined from head of the 2 rail grades, R350HT and R260. Specimens tested on Tinius Olsen testing machine at three different temperatures according to the ASTM E23-12, “Standard Test Methods for Notched Bar Impact Testing of Metallic Materials”. The Results of the tests are tabulated in the table 4.4 and 4.5

Table 4.4. R350 HT rail Impact test results.

Specimen Identification	Specimen Dimensions	Testing Temp.	Impact Test Result		
			Energy Absorbed (Joule)		Average (Joule)
R350 HT	10X10 ,2V	21 °C	8	8.7	8
R350 HT	10X10 ,2V	0 °C	5	6	6
R350 HT	10X10 ,2V	-20°C	5	6	6

Table 4.5. R350 HT rail Impact test results.

Specimen Identification	Specimen Dimensions	Testing Temp.	Impact Test Result		
			Energy Absorbed (Joule)		Average (Joule)
R 260	10X10 ,2V	21 °C	10	9	10
R260	10X10 ,2V	0 °C	8	8	8
R260	10X10 ,2V	-20°C	5	7	6

According to the charpy impact test results Table 4.4 and 4.5 results of rail R260 is a little bit higher than that of R350 HT, but this difference is small. One notable result is that R350HT impact toughness values are less sensitive to lower temperatures.

4.2.3 HARDNESS TEST RESULTS

Hardness measurements on the heads of two rails were taken at the specified positions according to EN 13674-1:2003+A1 and related ASTM E10-12 standards. Positions of indentations for hardness measurement on the head are shown in Figures 4.10 and 4.11 for R350HT and R260 grade rails. The results of head hardness values were given in Table 4.6.

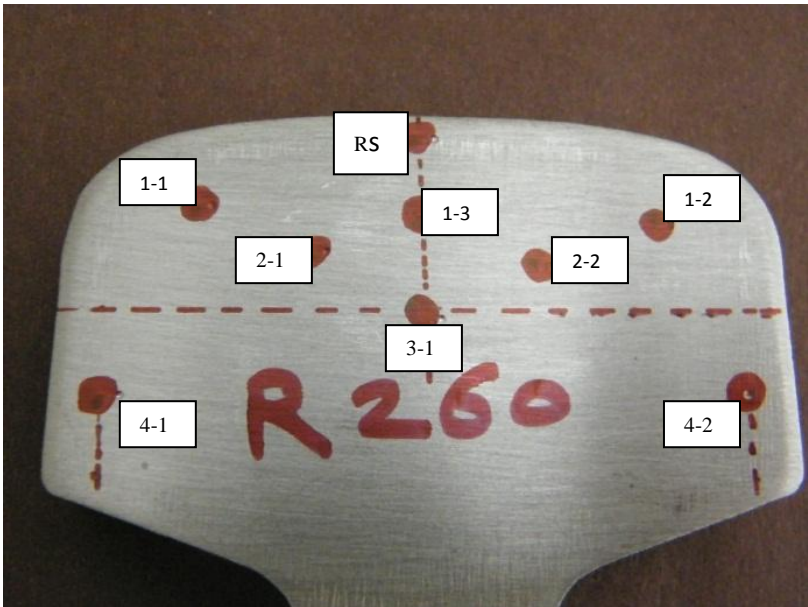


Figure 4.10.Hardness position of rail R 260.

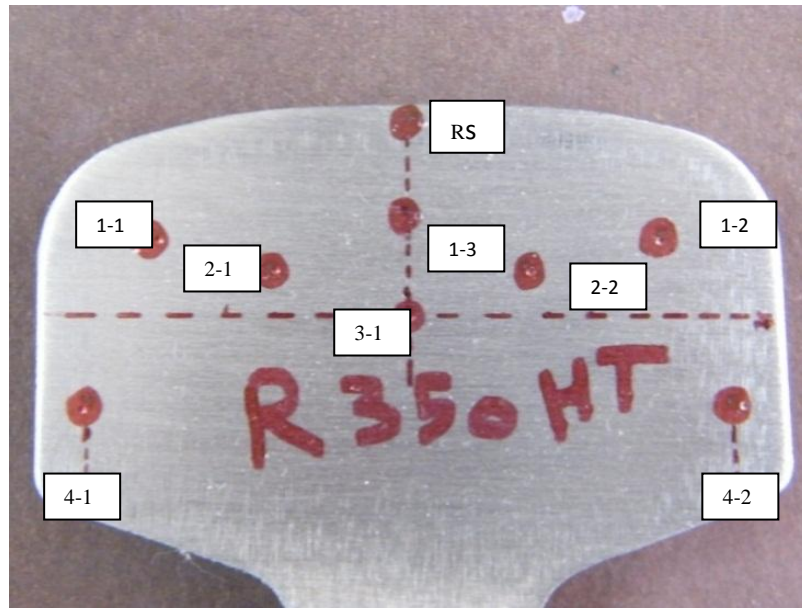


Figure 4.11.Hardness position of rail R350 HT.

Table 4.6. Hardness result of head of R350HT and R260.

Position	Brinell Hardness Number HB 187.5/2.5	
	R350 HT	R260
RS	362	263
1-1	383	282
1-2	348	273
1-3	375	267
2-1	400	282
2-2	361	266
3-1	344	288
4-1	347	285
4-2	350	277

Hardness measurements were also made at the webs of the rails with equally spaced intervals. The distance between two indentations is 5mm. The results of web hardness values were given in Table 4.7.

Table 4.7. Hardness result of web of R350HT and R260.

Position	Brinell Hardness Number HB 187.5/2.5	
	R350 HT	R260
1	290	284
2	286	251
3	286	240
4	266	252
5	268	244
6	270	251
7	269	254
8	270	239
9	261	240
10	260	233
11	279	234
Average Hardness Number	273 HB 187.5	247 HB 187.5

As can be seen from the results of the Table 4.6 and 4.7, R350 HT rail has hardness values greater than those for R260 rail, both in the head and web of the rail. From hardness survey it is apparent that hardness numbers do not change so much from rail running surface to the interior for both rail grades. This can be related to the carbon concentration of rail grades since high carbon content in steels results in hardenability curves do not vary so much after cooling. Furthermore, to achieve high stable hardness value in rail R350 HT, the carbon concentration of rail R350 HT

(table 3.1) is higher than the rail R260. Since hardenability is strongly dependent on carbon content.

4.3. FRACTURE TOUGHNESS TEST K_{Ic} RESULTS

Machined fracture toughness specimen from the head, web and the foot of the rails from the rail R350HT and R260 were subjected to the test. K_{Ic} fracture toughness tests were done on MTS 810 servo-hydraulic universal test machine. Tests conducted according to ASTM E399-09^{e2} [30]. Specimens were subjected to the fatigue cycling until that crack size conform to the requirement of the standard, i.e, crack extended until 0.45 W and 0.55 W (total size of crack starter plus fatigue crack). A fatigue precrack were introduced until it grew to 0.5 W by cyclical sinusoidal fatigue loading at the stress ratio $R=0.1$ ($\frac{P_{min}}{P_{max}}=0.1$) as shown in figure 4.12. Selection of fatigue precrack force should be such that fatigue sinusoidal force cycle does not pass 80 % of the predicted K_{Ic} value of the material, since higher values of K_{max} can cause sudden failure of the specimen and/or high rate of fatigue crack growth. The extension of fatigue precrack until the 0.5 W monitored using traveling microscope with the sensitivity of 0.1 mm.

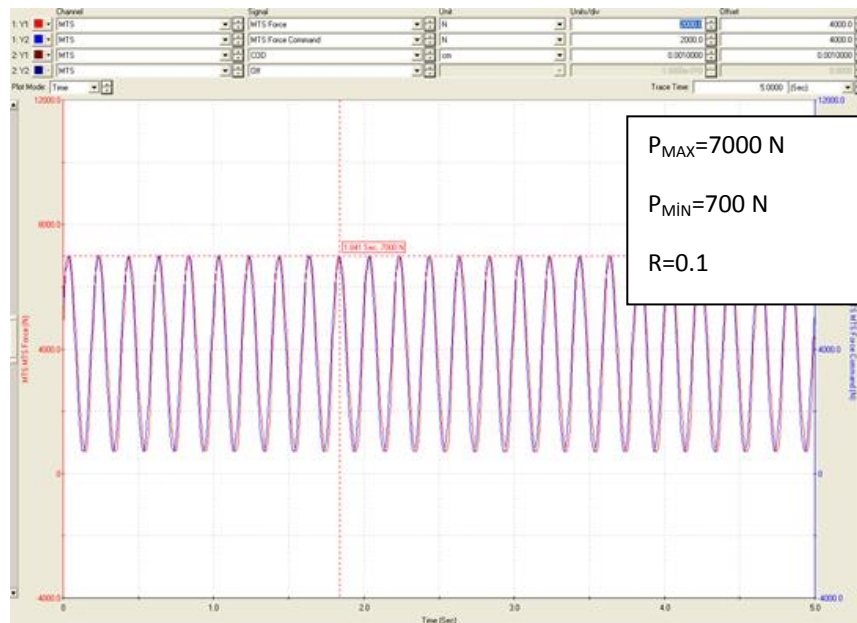


Figure 4.12. Sinoidal form of fatigue loading.

After introducing a fatigue precrack which meets requirements of ASTM E399-09^{e2}, MTS 632.01 displacement gage attached as shown in Figure 4.13 to the machined integral knife edges. After attachment of displacement gage, specimen is loaded with loading rate of 0.5 KN/s until specimen fractures. During loading of the specimen, force versus crack mouth opening displacement (CMOD) was recorded by a computerized data acquisition system.

Afterwards, force versus crack mouth opening displacement data was plotted for each of the specimens machined from the head, web and foot of the rails as shown in Figure 4.14.

According to ASTM E399-09^{e2}, in order to determine value of P_Q required to calculate K_Q of the specimens, a secant line was drawn through the origin of Force-versus- crack mouth opening displacement with slope of 0.95 (P/V), as shown in Figure 4.14. There are three types of typical force-displacement records for materials in the specified standard. Almost all of the fracture toughness specimens tested are TYPE III Force-versus- crack mouth opening displacement so P_{max} is the P_Q value of the specimens since maximum force comes prior to the P_5 value of the force. But one of the specimens has TYPE II Force-versus- crack mouth opening displacement record.

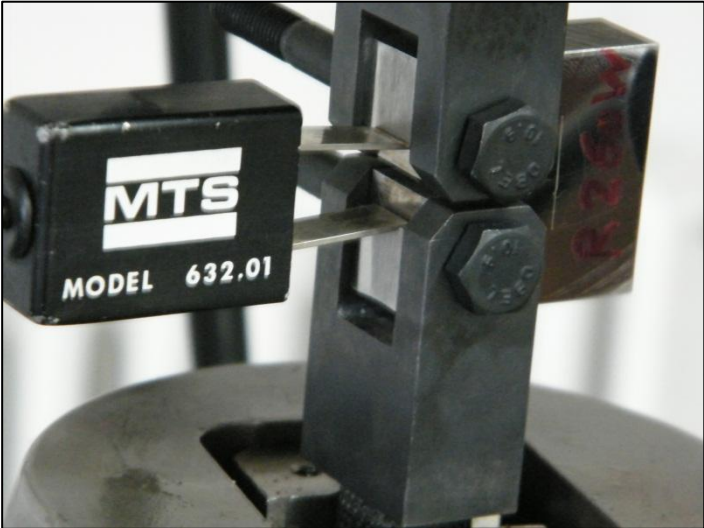


Figure 4.13. Displacement gage attached to integral knife edges of specimen.

After determining the value of the P_Q (table 4.8-a and 4.9-a), specimen crack size measured at mid thickness and two quarter thickness points. The average of three measurements of crack was taken as the crack size a . The average crack size measurement for three specimen head, web and foot for rail R350 HT can be seen in Figure 4.15. There is requirement for validity of average crack size which is surface crack size measurement cannot differ from the average crack size by more than 15 %.

By inserting the value of force P_Q , average crack size a and specimen dimension in the equation 3 and 4, fracture toughness K_Q value calculated. There are two requirements stated in the standard to validity whether calculated K_Q value is plane-strain Fracture toughness K_{IC} or not. The first one is the ratio of P_{max}/ P_Q does not exceed 1.1 .The latter one is the value $2.5 (K_Q / \sigma_y)^2$ must be less than the specimen ligament size, $W-a$.

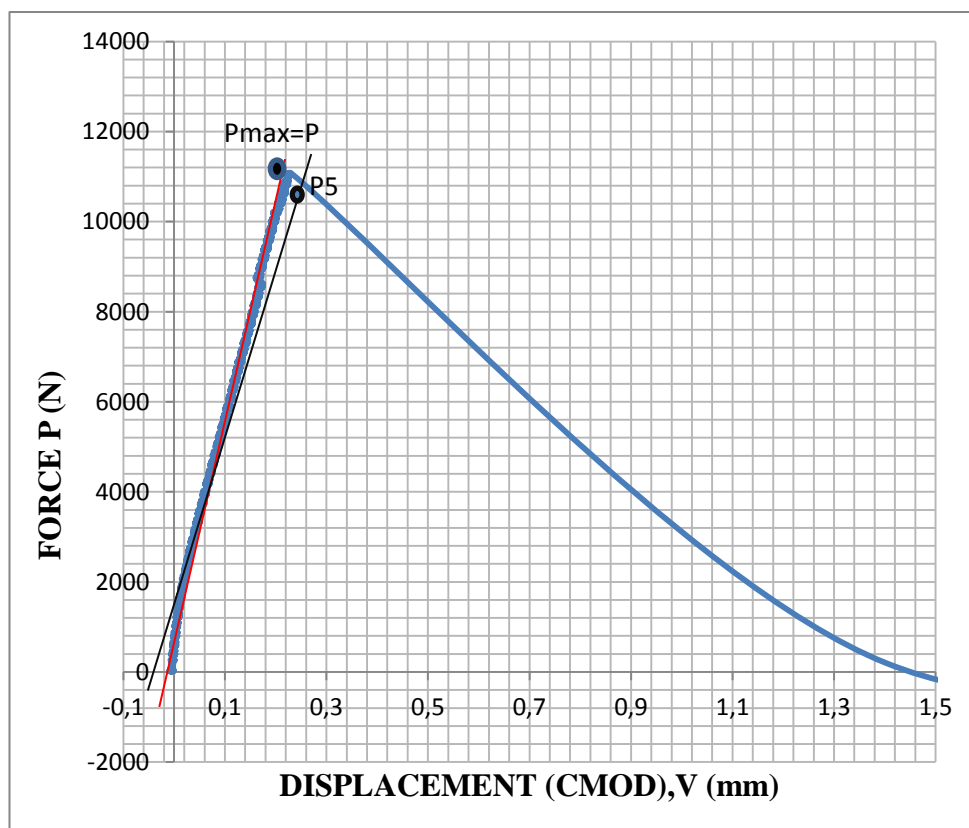


Figure 4.14. Force versus crack mouth opening displacement record.

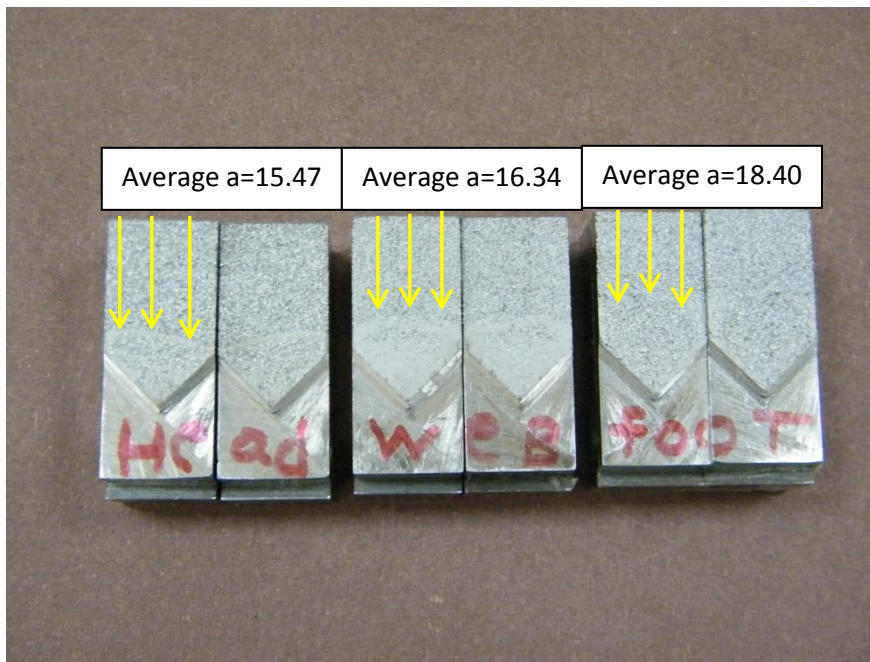


Figure 4.15. Average crack size measurement for three specimen head, web and foot of rail R350 HT.

$$K_Q = \frac{P_Q}{B B_N \sqrt{W}} f\left(\frac{a}{w}\right) \quad (3)$$

$$f\left(\frac{a}{w}\right) = \frac{2 + \frac{a}{w} \left(0.886 + \frac{4.64a}{w} - 13.32 \frac{a}{w}^2 + 14.72 \frac{a}{w}^3 - 5.6 \frac{a}{w}^4 \right)}{1 - \frac{a}{w}^{\frac{3}{2}}} \quad (4)$$

P_Q = force, N

B =specimen thickness, m

B_N =specimen thickness between the roots of the side grooves, m

W =specimen width, m

a =crack size, m

For all of the fracture toughness specimens machined from the head, web and foot of R350HT and R260 rail grades, fracture toughness values were calculated and given in Table 4.8-b and Table 4.9-b. By consideration of validity requirement mentioned previously for plane-strain fracture toughness two specimens in R350 HT and three specimens in R260 meet validity requirement as seen in Table 4.8-b and 4.9-b. The specimens which do not meet validity requirement have ligament size $w-a$ less than

the value of validity requirement $2.5 (K_Q / \sigma_y)^2$ therefore calculated values are K_Q Fracture Toughness and not K_{IC} Plane –Strain Fracture Toughness.

Table 4.8.a. Fracture toughness R350 HT results.

Specimen No.	Specimen Thickness B (mm)	Average Crack Size a (mm)	Specimen Width W (mm)	Specimen Ligament Size W-a (mm)	Force P_{max} (N)	Force P_Q (N)
HEAD	15.9	15.47	32	15.78	13041	13041
WEB	15.9	16.34	32	15.74	19370	19370
FOOT	16.0	18.40	32	15.41	10000	10000

Table 4.8.b. Fracture toughness R350 HT results.

Specimen No.	Validity requirement $\frac{P_{max}}{P_Q}$	Validity requirement $2.5 \frac{K_Q^2}{\sigma_{ys}}$ (mm)	Fracture Toughness K_Q $Mpa \bar{m}$	Plane –Strain Fracture Toughness K_{IC} $Mpa \bar{m}$
HEAD	1	7.80	42.2	42.2
WEB	1	31.70	68.1	---
FOOT	1	12.86	43.4	43.4

Table 4.9.a. Fracture toughness R260 results.

Specimen No.	Specimen Thickness B (mm)	Average Crack Size a (mm)	Specimen Width W (mm)	Specimen Ligament Size W-a (mm)	Force P_{max} (N)	Force P_Q (N)
HEAD Transverse Direction	16.0	17.19	32	16.56	8957	8957
WEB Transverse Direction-1	16.0	17.81	32	17.00	10859	10859
WEB Transverse Direction-2	16.0	17.71	32	15.5	7360	7176
WEB Longitudinal Direction	16.0	18.19	32	15.02	11066	11066
FOOT Transverse Direction	16.0	16.7	32	16.03	12900	12900

Table 4.9.b Fracture toughness R260 results.

Specimen No.	Validity requirement $\frac{P_{max}}{P_Q}$	Validity requirement $2.5 \frac{K_Q}{\sigma_{ys}}$ (mm)	Fracture Toughness K_Q Mpa \bar{m}	Plane –Strain Fracture Toughness K_{Ic} Mpa \bar{m}
HEAD Transverse Direction	1.00	6.77	34.1	34.1
WEB Transverse Direction-1	1.00	21.71	44.1	---
WEB Transverse Direction-2	1.03	9.26	28.83	28.83
WEB Longitudinal Direction	1.00	14.83	46.6	46.6
FOOT Transverse Direction	1.00	14.89	46.7	46.7

The calculated values of fracture toughness given in the above tables, fracture toughness of R350 HT in head and web has higher value than fracture toughness of R260 in the head and web. This higher value of fracture toughness in the head is related to the much finer pearlite structure in the head of the rail R350 HT resulted from the forced cooling from austenite temperatures. Higher fracture toughness of the rail in the web of the rail R350 HT can be explained again by the faster cooling rate. In head hardened rails, cooling rate at the end of hot rolling is higher than that of R260 rail in the head region of the rail profile. So, these high cooling rates apparently affect also the web of the rail. This cooling effect is also evident in the hardness data taken from the heads and the webs of R350 HT and R260 rails. The fracture toughness values in the foot sections of both rails are nearly the same.

4.4 FRACTURE TOUGHNESS K_{IIC} TESTING

Fatigue precracking is conducted on compact shear specimen machined from the web of the rail R260 in the longitudinal direction as shown in Figure 4.16 until $0.45W$. Tension-tension cyclically sinusoidal loading with stress ratio of $R=0.1$ ($\frac{P_{min}}{P_{max}}=0.1$) in Mode I (fig 4.17-a) was applied to the specimen by MTS 810 servo-hydraulic universal test machine. Fatigue precracking loads were calculated from the formula 1. Specimens, previously fatigue precracked in Mode I, inserted in the loading frame for K_{IIC} tests as shown in figures 4.17-b and 4.18.

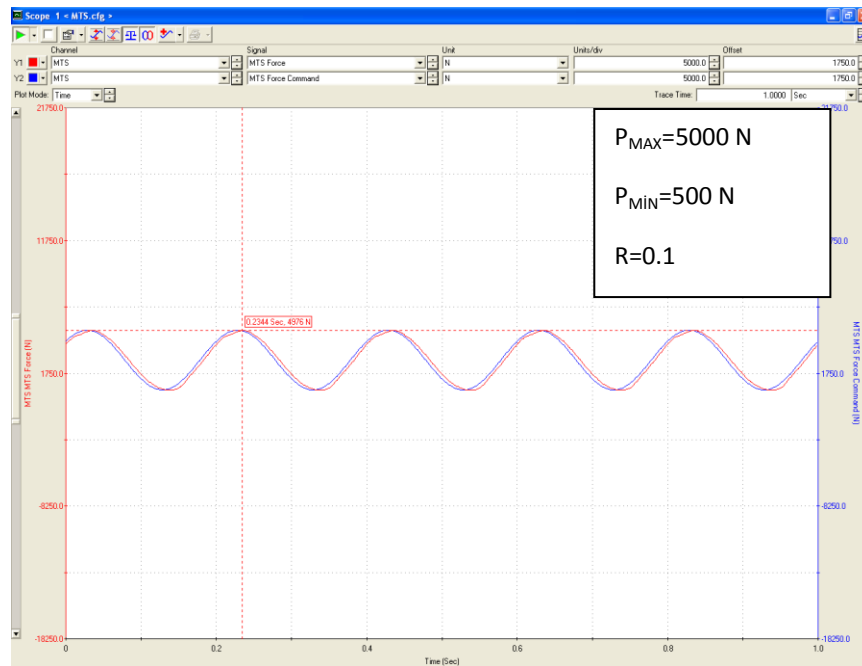


Figure 4.16. Sinosoidal form of fatigue loading.

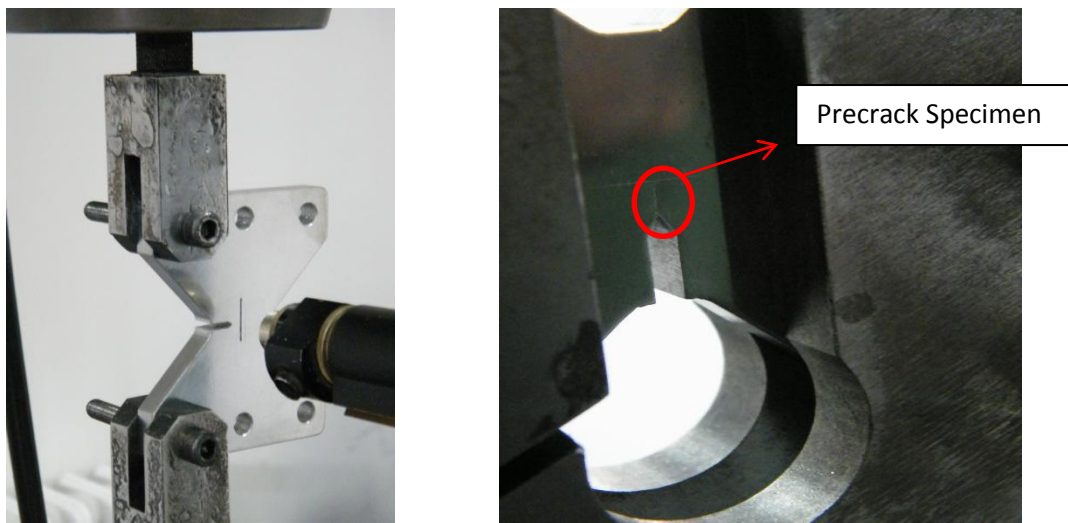


Figure 4.17. (a) Mode I loading. (b)specimen inserted in frame.

After inserting the shear specimen in the loading frame, specimen was loaded at loading rate of 0.5 KN/sec until the fracture of the specimen. Force versus displacement data recorded by MTS data acquisition system.



Figure 4.18. Shear specimen inserted in loading frame.

According to the study of the Banks-Sills L. and Arcan M, data evaluation for finding K_{IIC} fracture toughness is the same as the ASTM E399.

According to the ASTM E399-09^{e2}, in order to determine value of P_Q required to calculate K_Q of the specimens, a secant line was drawn through the origin of Force versus displacement with slope of 0.95 (P/V). as shown in Figure 4.19.

All of the toughness specimen tested were TYPE III Force versus displacement so P_{max} is the P_Q value of the specimens since Maximum force comes prior to the P_5 value of the force.

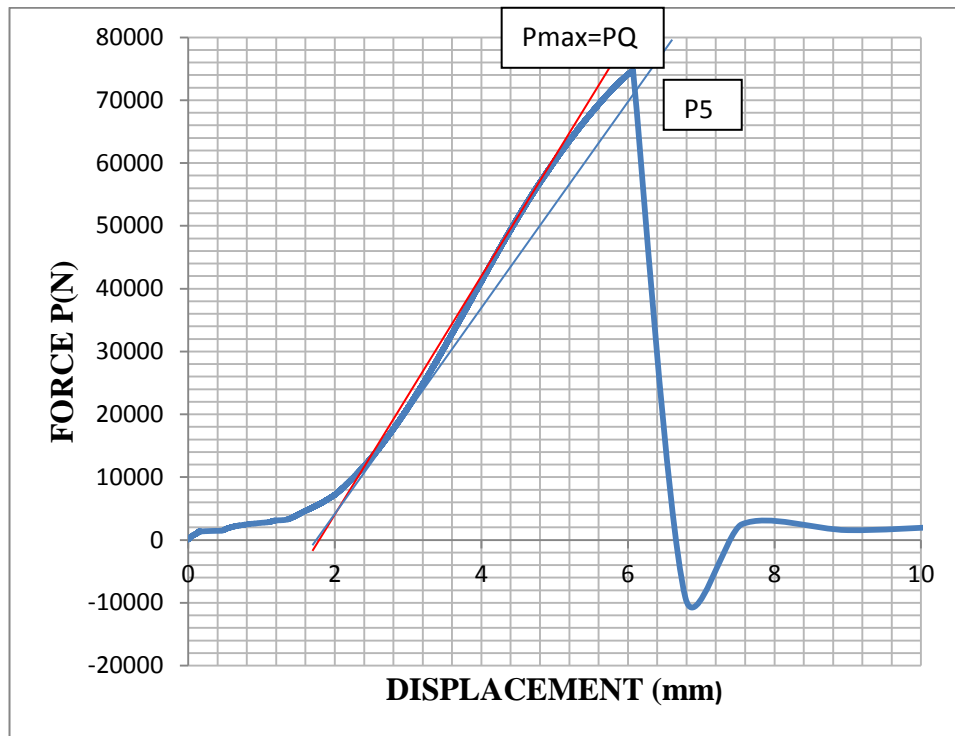


Figure 4.19. Force versus displacement record.

After determining the value of the PQ, specimen crack size measured at mid thickness and two quarter thickness points. The average value of three crack size measurements was taken as the crack size a . The average crack size measurement for one of the specimen is shown in figure 4.20. By inserting the value of force PQ, average crack size a and specimen dimension in the equation 2, fracture toughness K_{IIC} value is calculated. Results of the compact shear specimens are provided in Table 4.10.

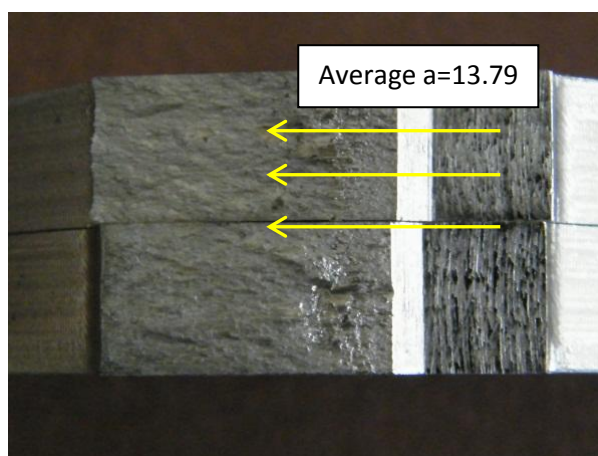


Figure 4.20. Shear specimen after fracture.

Table 4.10. R260 rail Shear specimen fracture toughness test results.

Specimen No.	Average Crack Size a (mm)	Specimen Width W (mm)	Force P_{max} (N)	Force P_Q (N)	Fracture Toughness K_{IIc} $Mpa \bar{m}$
R260 Longitudinal Direction WEB 1	13.79	30	79000	79000	64.2
R260 Longitudinal Direction WEB 2	15.91	30	73631	73631	67.5
R260 Longitudinal Direction WEB 3	13.98	30	84159	84159	69.1

Table 4.11.Results of K_{IC} and K_{IIc} of rail R260 in the web.

Specimen No.	Average Fracture Toughness K_{IIc} $Mpa \bar{m}$	Fracture Toughness K_{IC} $Mpa \bar{m}$
R260 WEB Longitudinal Direction	67	46.6

As seen from the table above Mode I fracture toughness value of rail R260 in the web in the longitudinal direction is lower than the Mode II fracture toughness in the same direction. It can be concluded that K_{IIc} is approximately 1.44 K_{IC} .

4.5. MODE II FATIGUE TESTING

Mode II fatigue testing were conducted on shear compact specimens with stress ratio of $R = -1$ ($\frac{P_{min}}{P_{max}} = -1$) but because of branching at the tip of crack test stopped. Crack tip change to Mode I type of fatigue crack growth as shown in Figure 4.21.

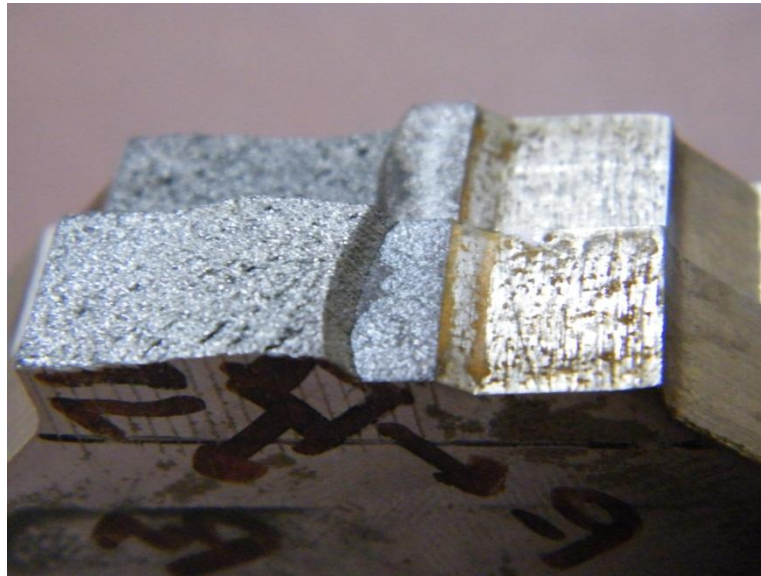


Figure 4.21. Mode II fatigue crack growth specimen.

4.6. CRACK LENGTH VERSUS NUMBER OF CYCLE CURVES FOR MODE I FATIGUE TESTING

Crack measurements versus number of cycles were conducted by the rumul krak gage glued on the specimen. Repeated tensile to tensile sinusoidal loading was applied to the specimen by MTS 810 machine. Applied loads to the specimen chosen such that loads to be lower than K_{max} of the specimen as seen in Figure 4.22-a. Fatigue precracking conducted before starting the collection of data to remove the effect of machined starter notch. K-increasing test procedure with constant force amplitude was applied. By applying constant repeated loading Figure 4.22-b crack extended and this extension was read from the screen of the fractomat device. Number of cycles recorded for every 0.1 mm extension of the crack and finally

plotted against crack length as can be seen in Figures 4.23 to 4.28 for both R350 HT and R260 rails.

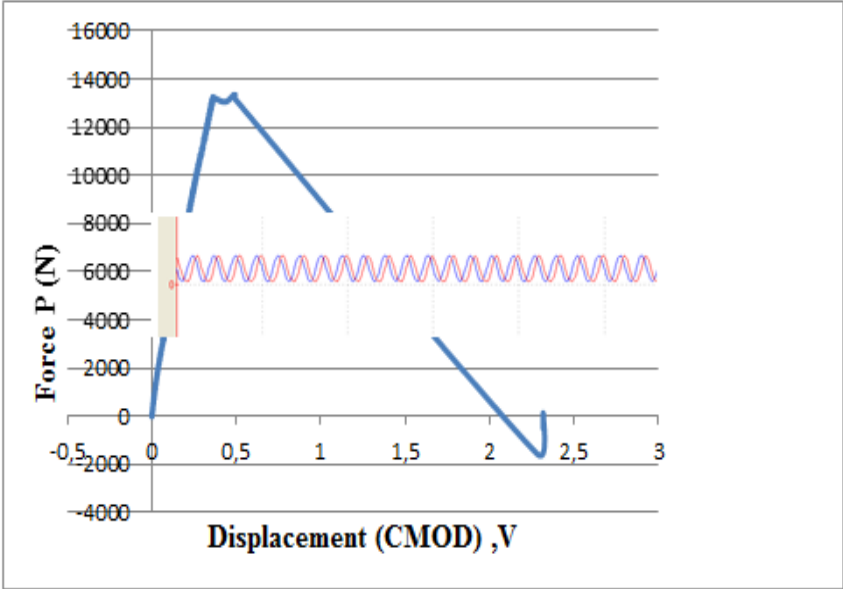


Figure 4.22. (a) Applied fatigue loads lower than K_{max}

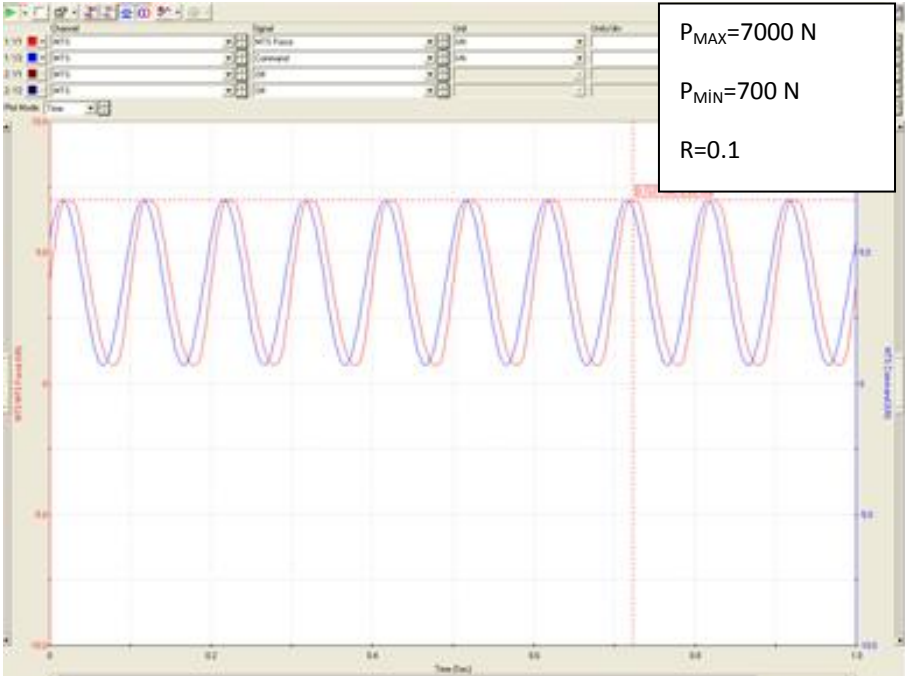


Figure 4.22. (b) Constant range repeating loading.

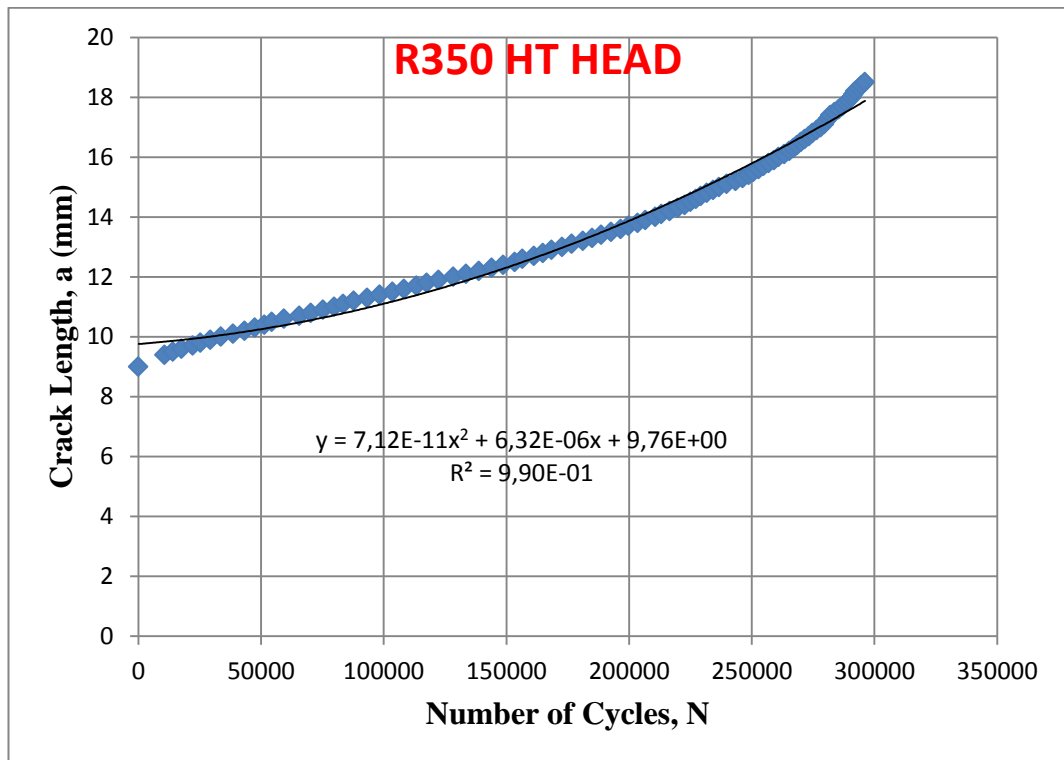


Figure 4.23.Crack length versus number of cycles of R350 HT HEAD.

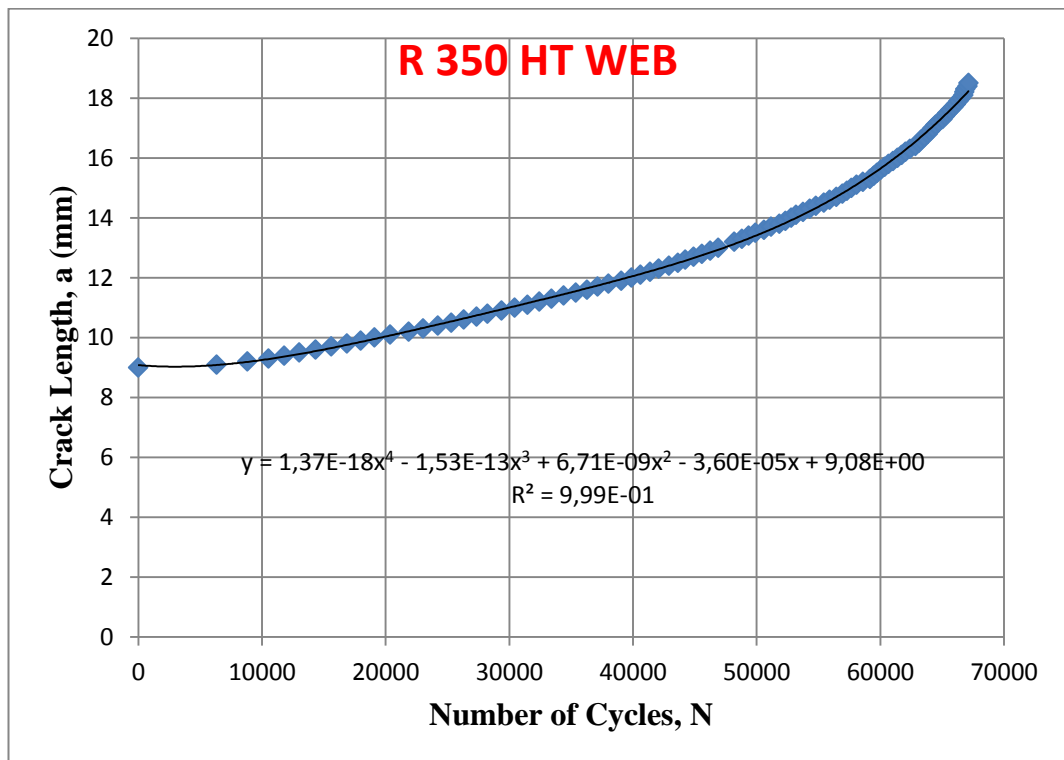


Figure 4.24.Crack length versus number of cycles of R350 HT WEB.

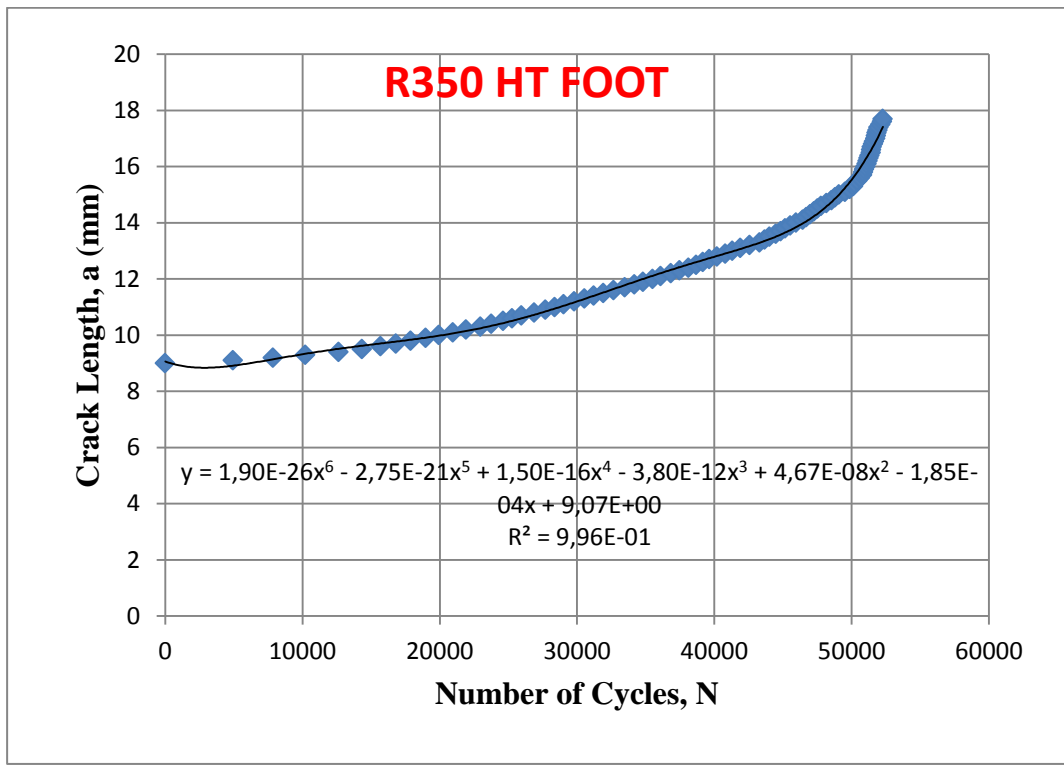


Figure 4.25.Crack length versus number of cycles of R350 HT FOOT.

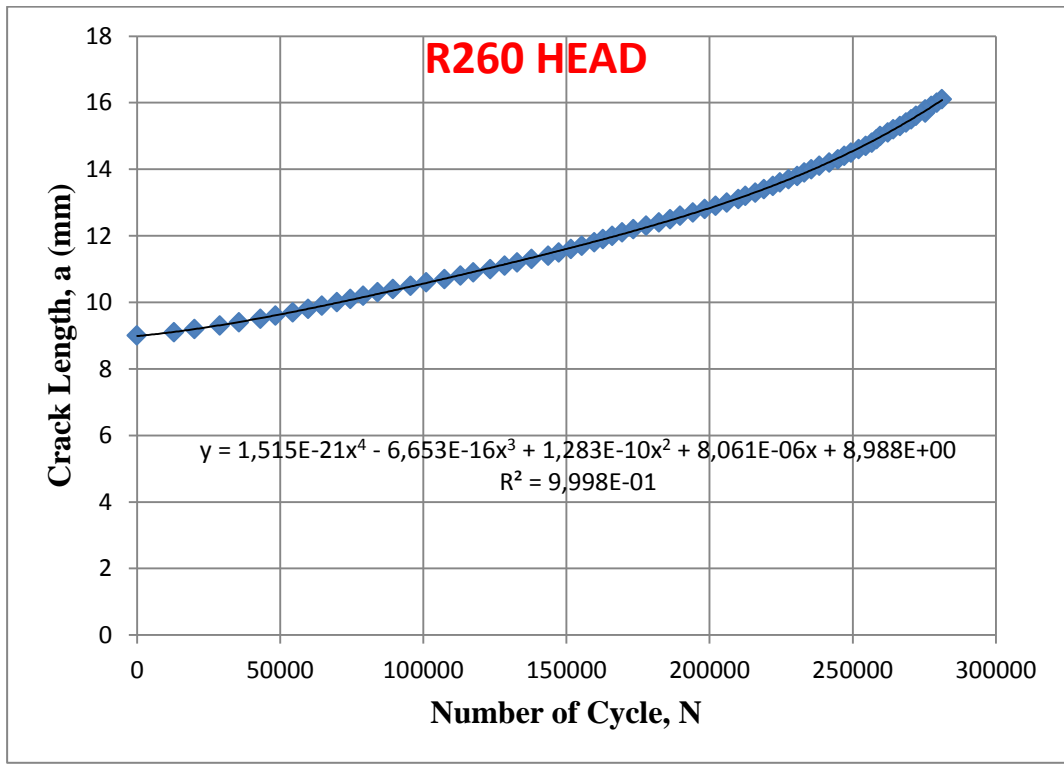


Figure 4.26.Crack length versus number of cycles of R260 HEAD.

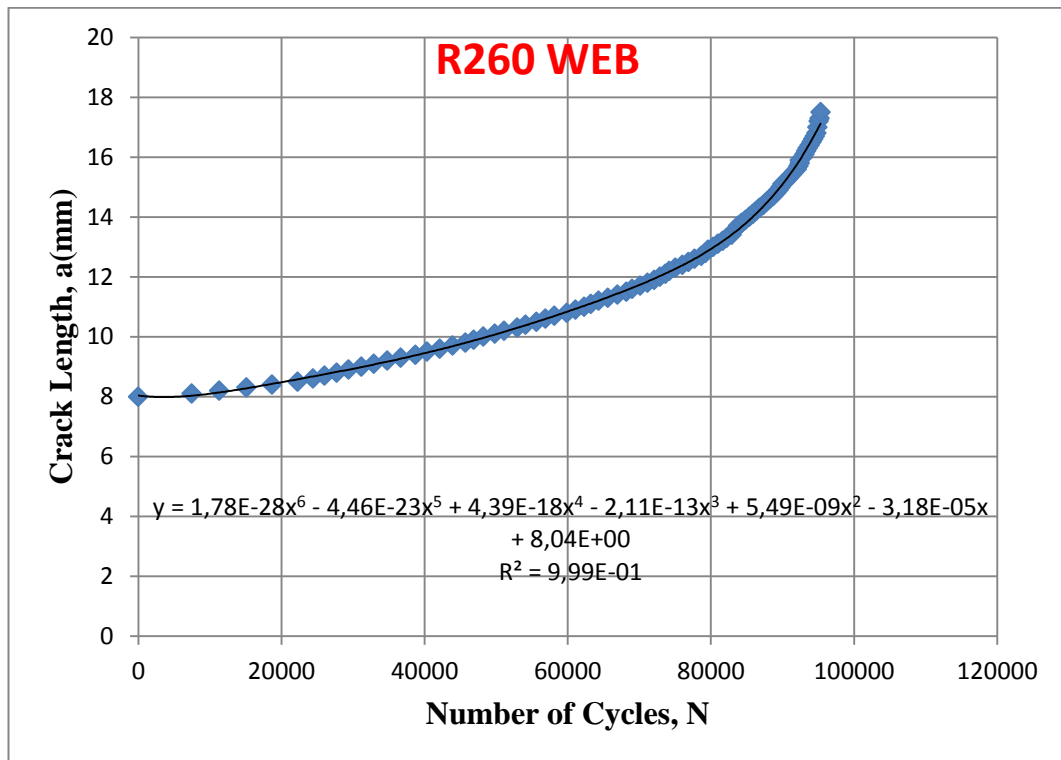


Figure 4.27.Crack length versus number of cycles of R260 WEB.

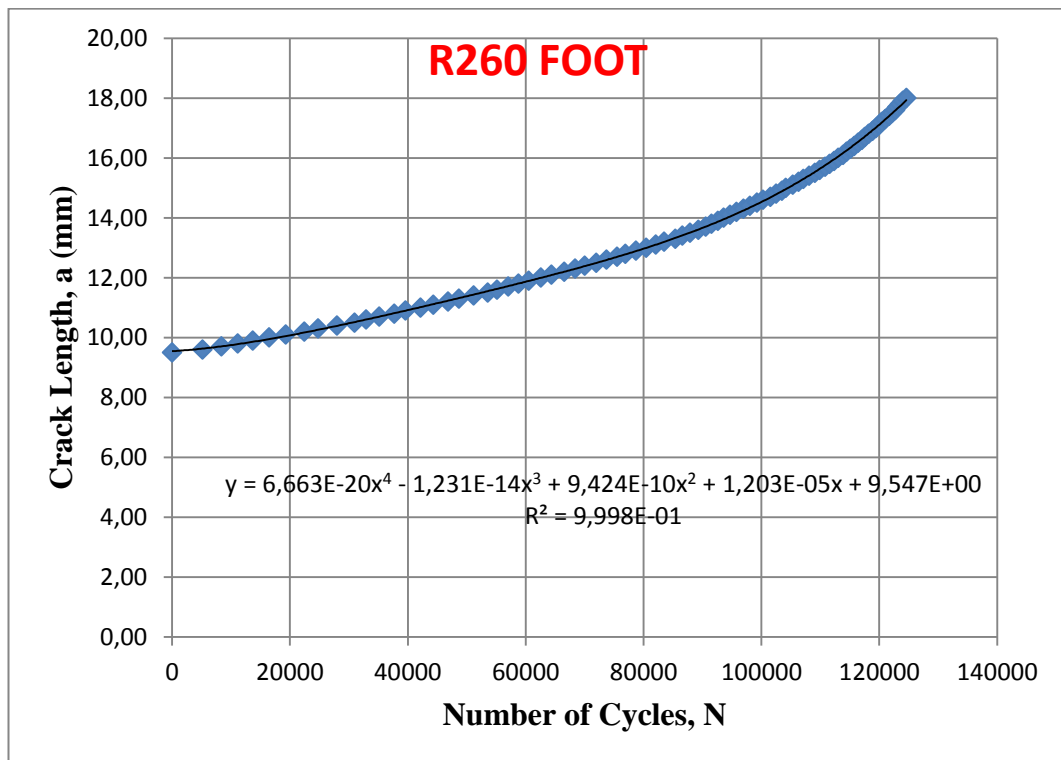


Figure 4.28.Crack length versus number of cycles of R260 FOOT.

4.7. CRACK GROWTH RATE VS STRESS INTENSITY RANGE

Crack growth rate versus stress intensity range for all of the specimens are plotted using seven point incremental polynomial method as given in ASTM E647-11. In this method a second order polynomial is fitted to the seven data points. The local fit has the form like the equation 5 :

$$\hat{a}_i = b_0 + b_1 \frac{Ni-C1}{C2} + b_2 \frac{Ni-C1}{C2}^2 \quad (5)$$

Where
$$-1 \leq \frac{Ni-C1}{C2} \leq 1$$

b_0 , b_1 and b_2 are the parameters which are found by least square methods over the range $a_{i-n} \leq a \leq a_{i+n}$. The growth rate of crack at cycle N_i is calculated by taking the derivative of the fitted parabola as follows:

$$(da/dn)_{a=i} = (b_1)/(C_2) + 2b_2(N_i - C_1)/C_2^2 \quad (6)$$

The value of stress Intensity Factor Range, ΔK corresponding to da/dN is calculated via the fitted crack size, corresponding N_i .

$$\Delta K = \frac{\Delta P}{B \sqrt{W}} \frac{2+\alpha}{1-\alpha^{\frac{3}{2}}} (0.886 + 4.64\alpha - 13.32\alpha^2 + 14.72\alpha^3 - 5.6\alpha^4) \quad (7)$$

Crack growth rate (da/dN) versus stress intensity factor range ΔK plotted via BASIC computer program stated in ASTM E647-11. An example of the output of BASIC computer program for R350 HT HEAD specimen is given in appendix. In the output of the program M.C.C means multiple correlation coefficient which shows goodness of fit.

Crack growth rate versus stress intensity factor range ΔK plotted for all specimens as can be seen in Figures 4.29 to 4.34.

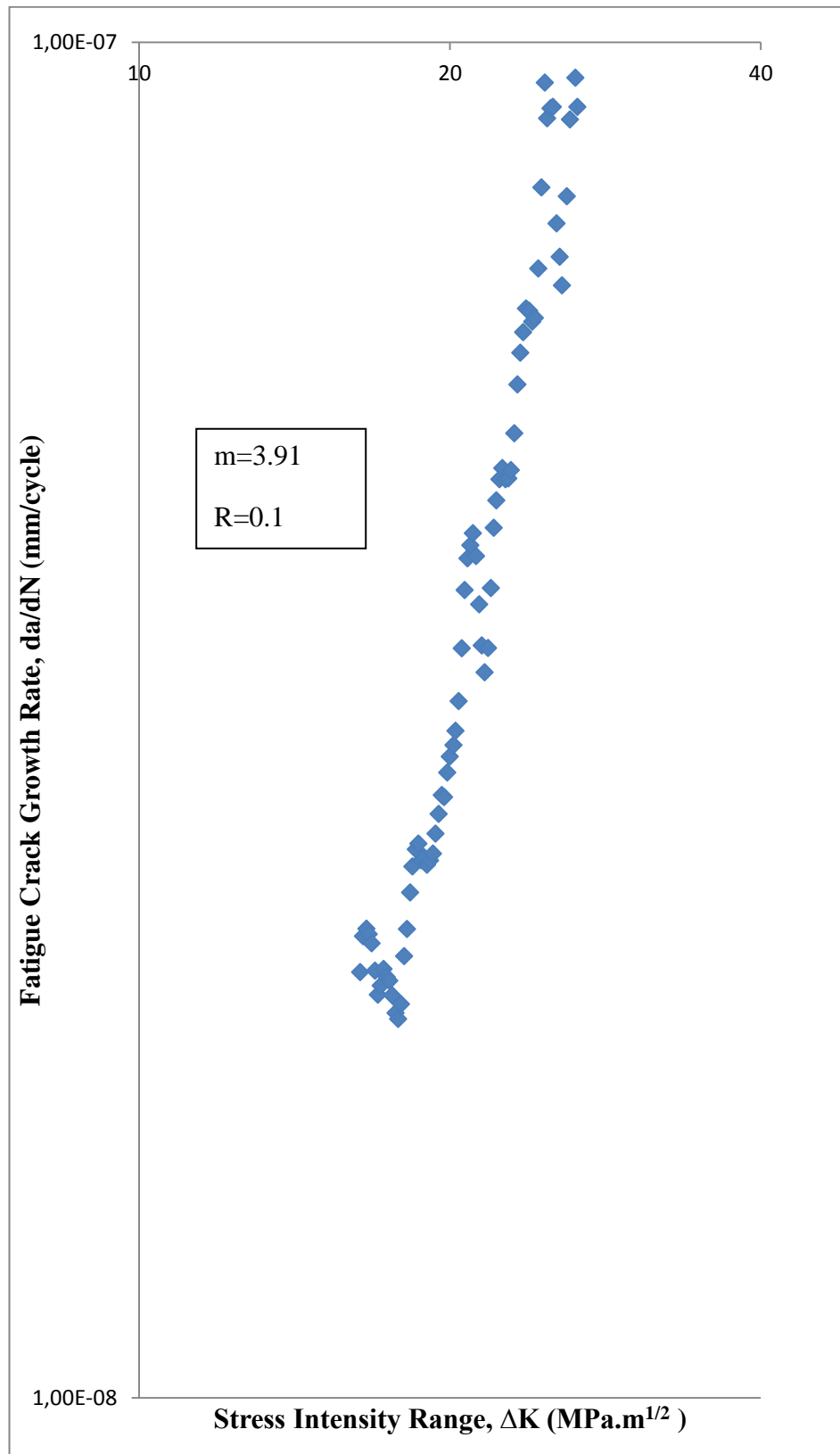


Figure 4.29. da/dN vs. ΔK plot of R350 HT HEAD.

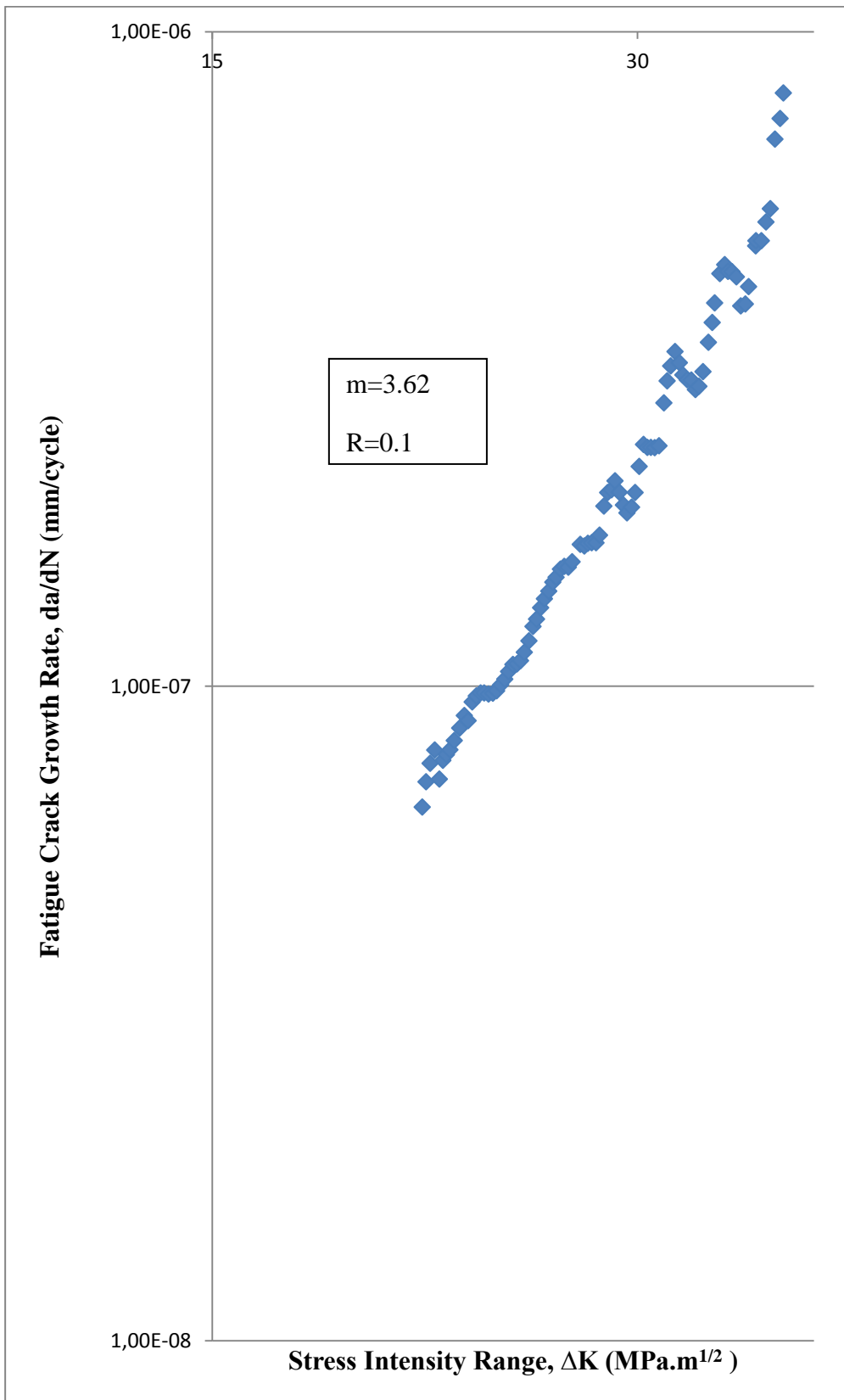


Figure 4.30. da/dN vs. ΔK plot of R350 HT WEB.

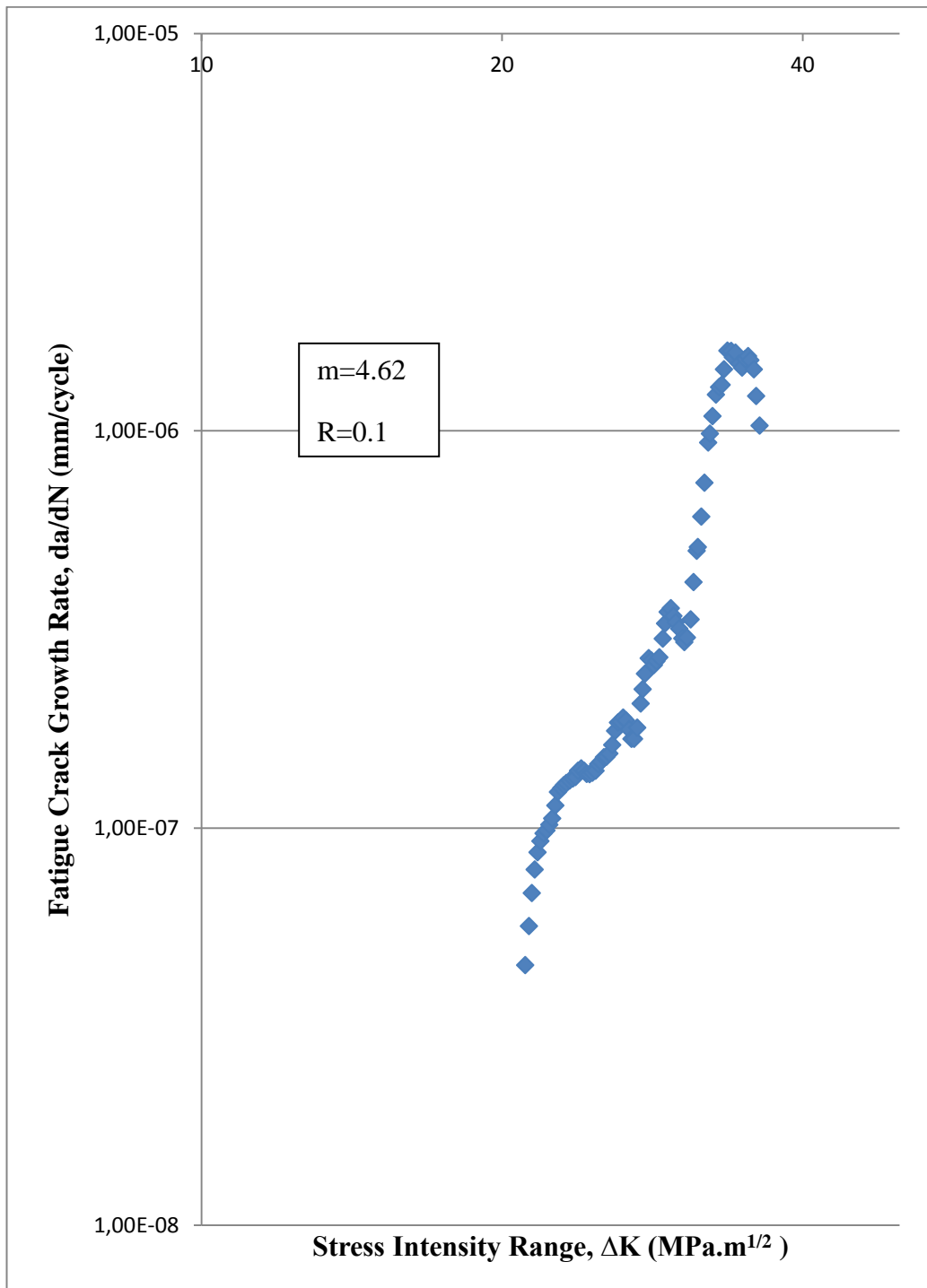


Figure 4.31. da/dN vs. ΔK plot of R350 HT FOOT.

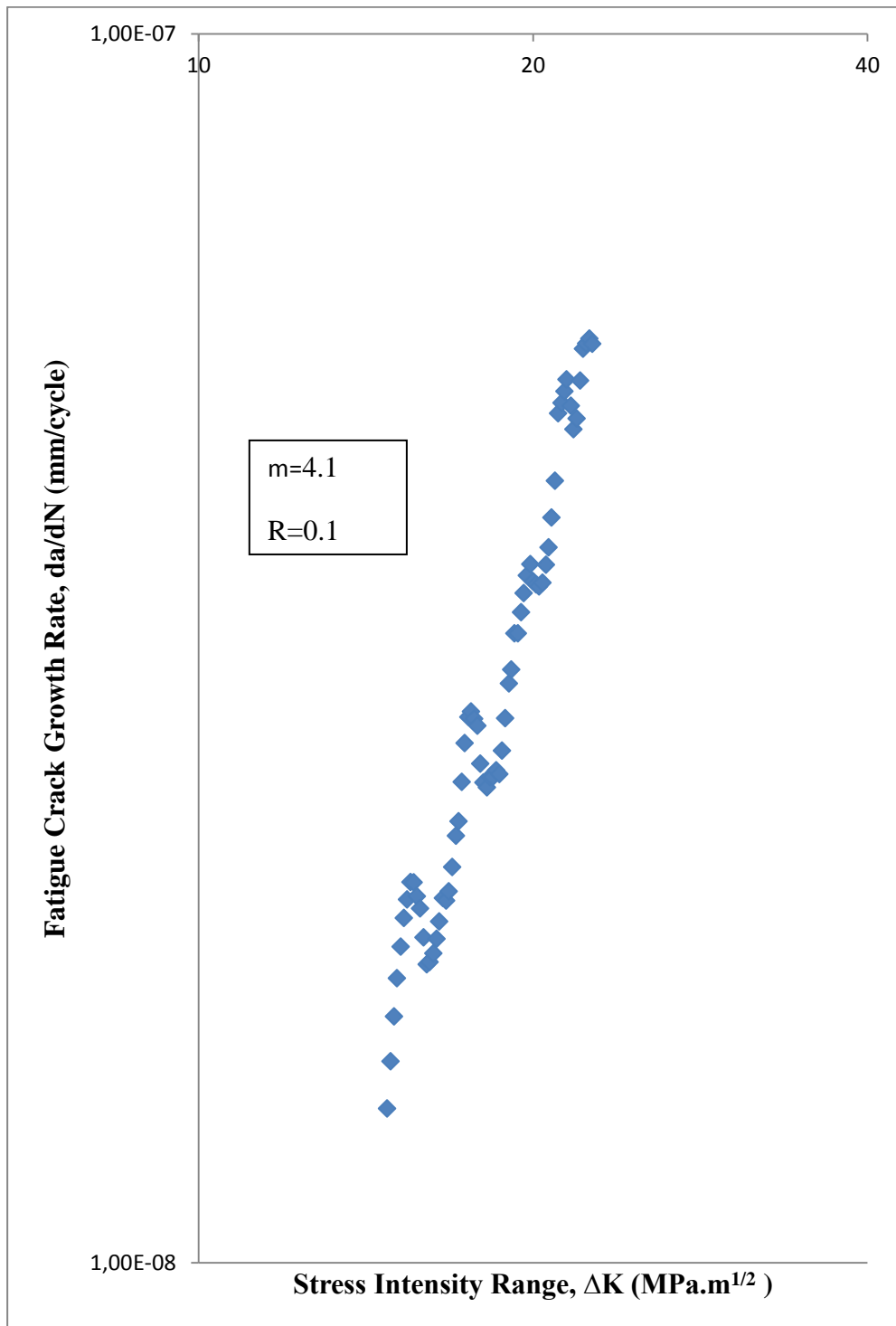


Figure 4.32. da/dN vs. ΔK plot of R260 HEAD.

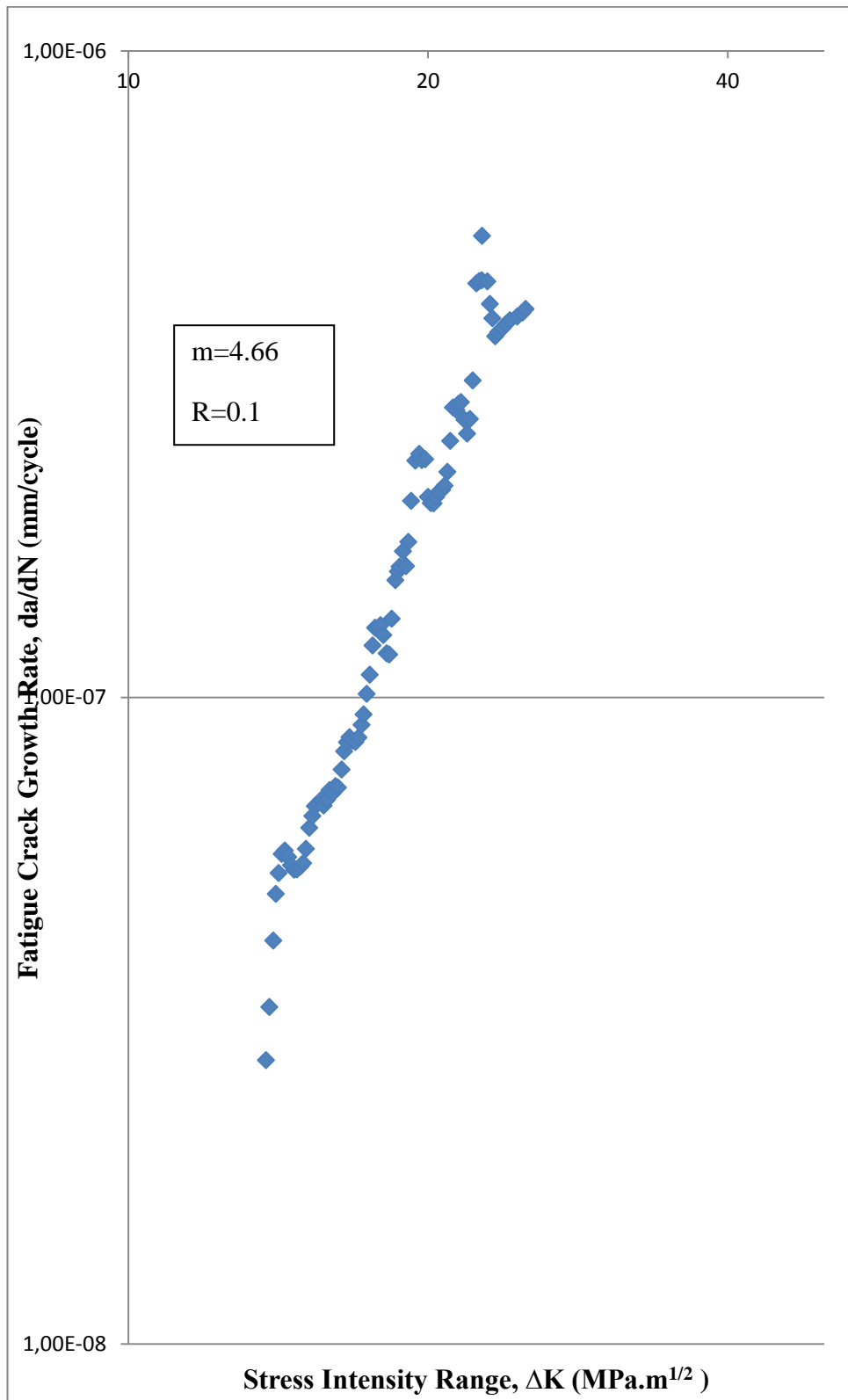


Figure 4.33. da/dN vs. ΔK plot of R260 WEB.

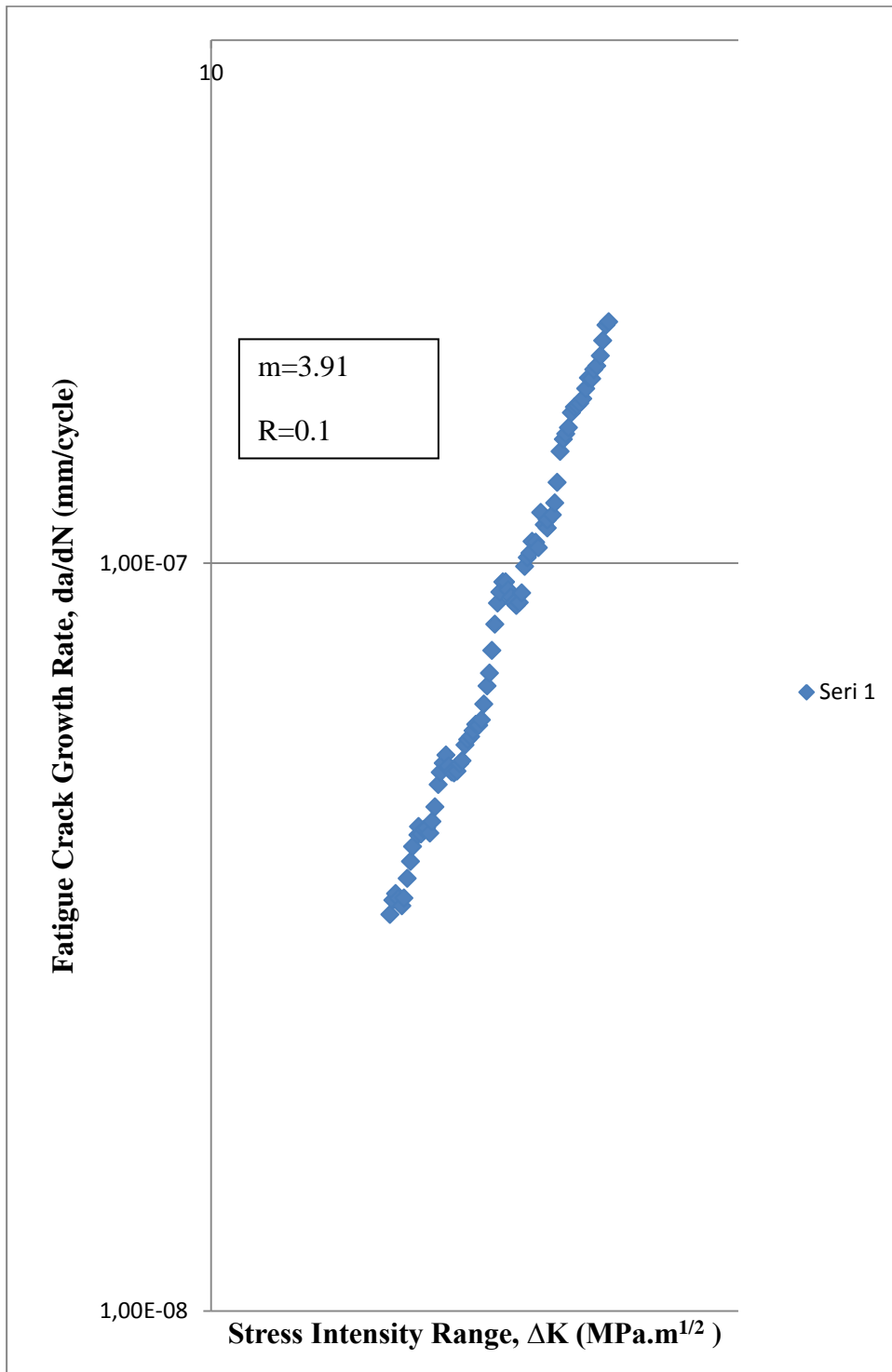


Figure 4.34. da/dN vs. ΔK plot of R260 FOOT.

4.8. PARIS –ERDOGAN LAW APPLICATION

Paris-Erdogan law was fit to the linear portion of the plot da/dN versus ΔK of R350 HT and R260 rails. As seen in the figure below constant m of the Paris-Erdogan law is the slope of $\log da/dN$ versus $\log \Delta K$. The value of C can be calculated by extending the line to intercept $\log da/dN$ where ΔK is $1 \text{ Mpa m}^{1/2}$. Linear regions of $\log da/dN$ versus $\log \Delta K$ given in Figures 4.36 to 4.41. Results of the constants C and m tabulated in Table 4.12. After determination of constants, rate of fatigue crack growth rate for all specimens calculated at $\Delta K=25 \text{ MPa.m}^{1/2}$ as seen in Table 4.13.

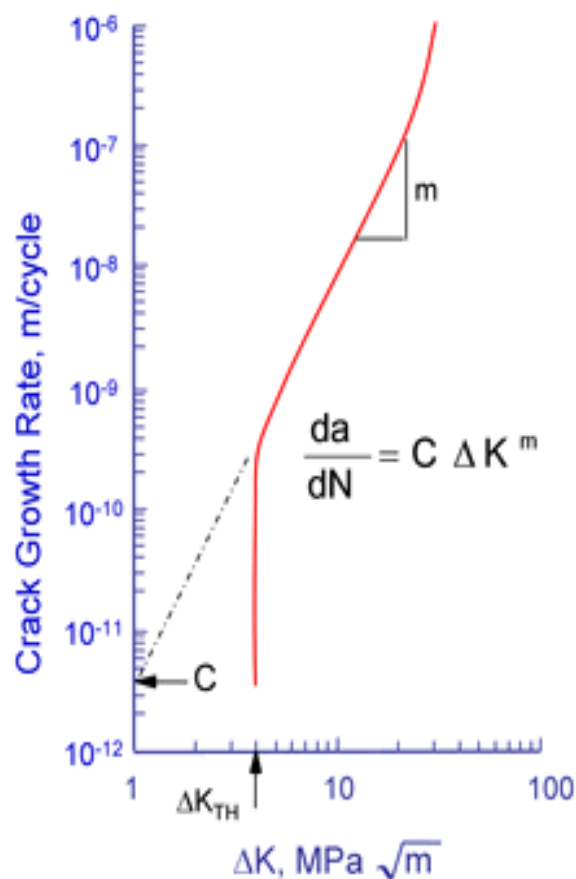


Figure 4.35. da/dN vs. ΔK plot [34].

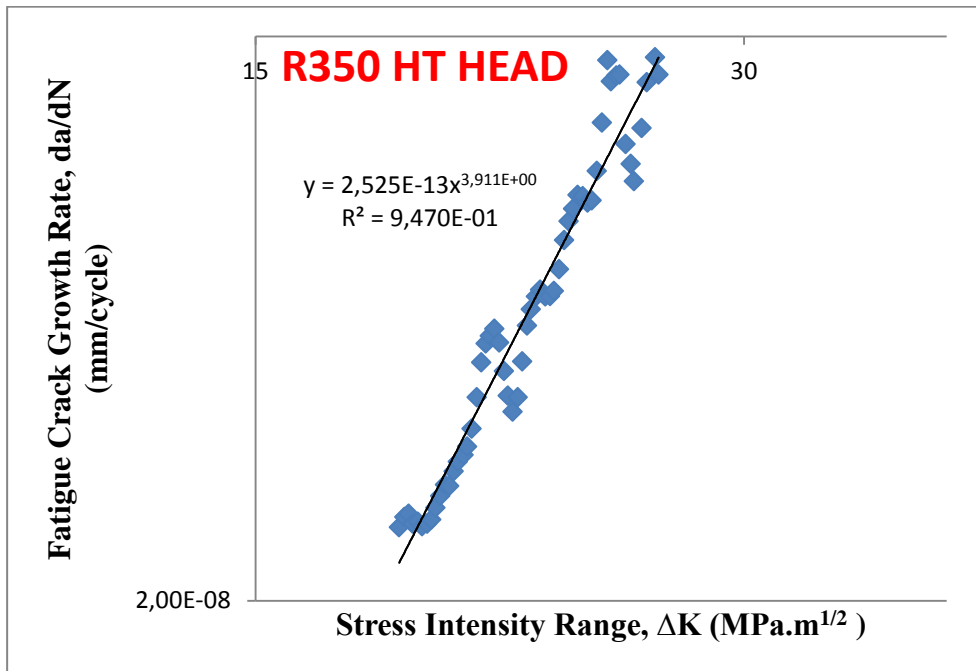


Figure 4.36. Linear region of da/dN vs.ΔK plot of R350 HT HEAD.

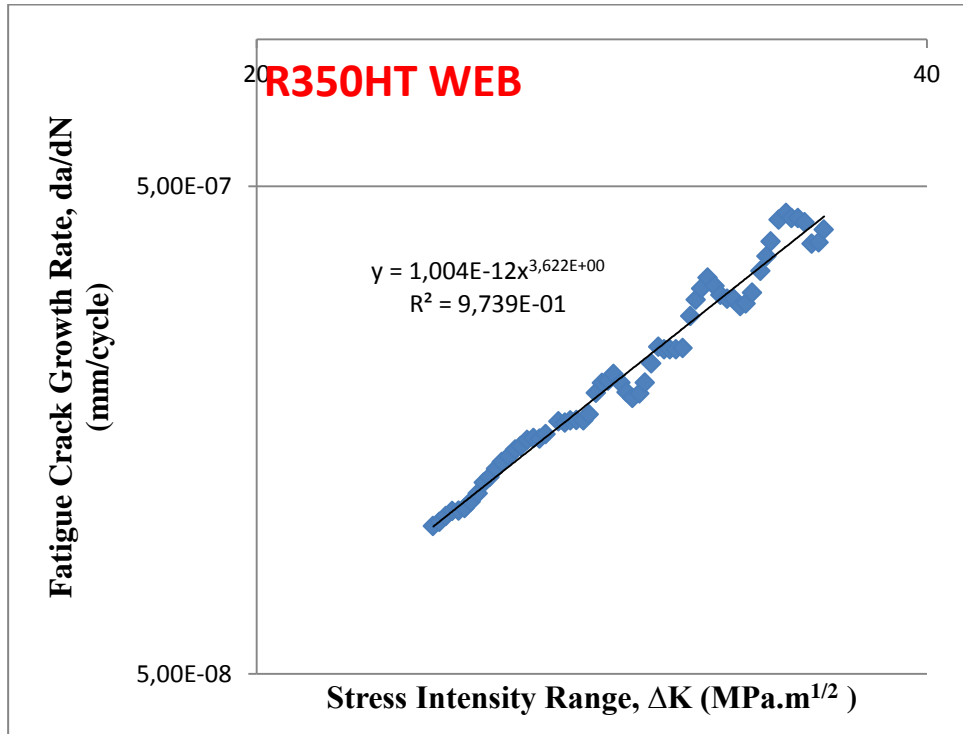


Figure 4.37. Linear region of da/dN vs.ΔK plot of R350 HT WEB.

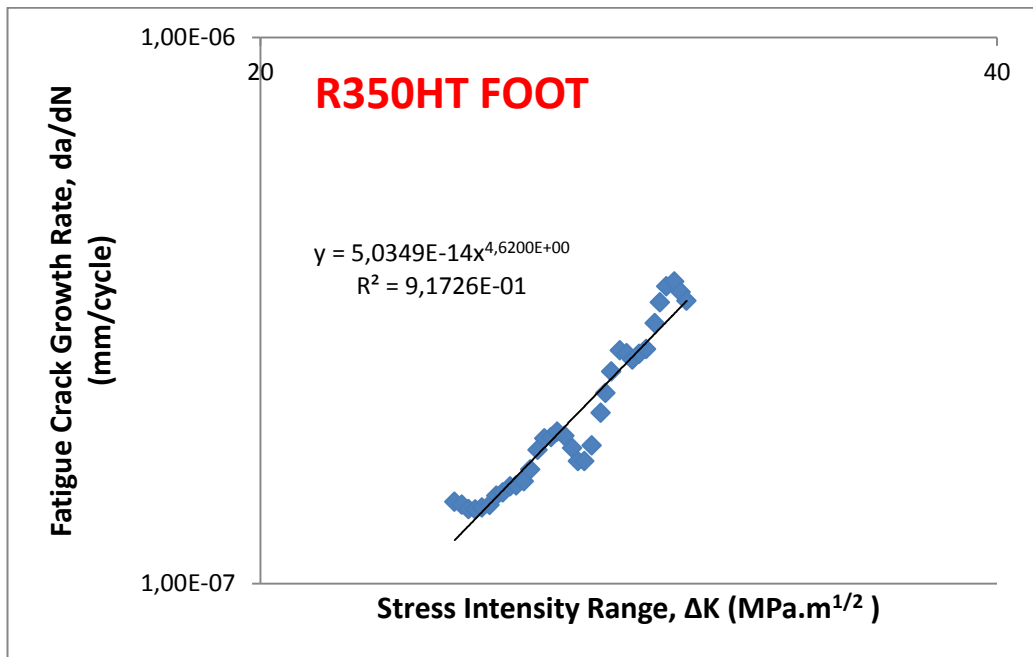


Figure 4.38. Linear region of da/dN vs.ΔK plot of R350 HT FOOT.

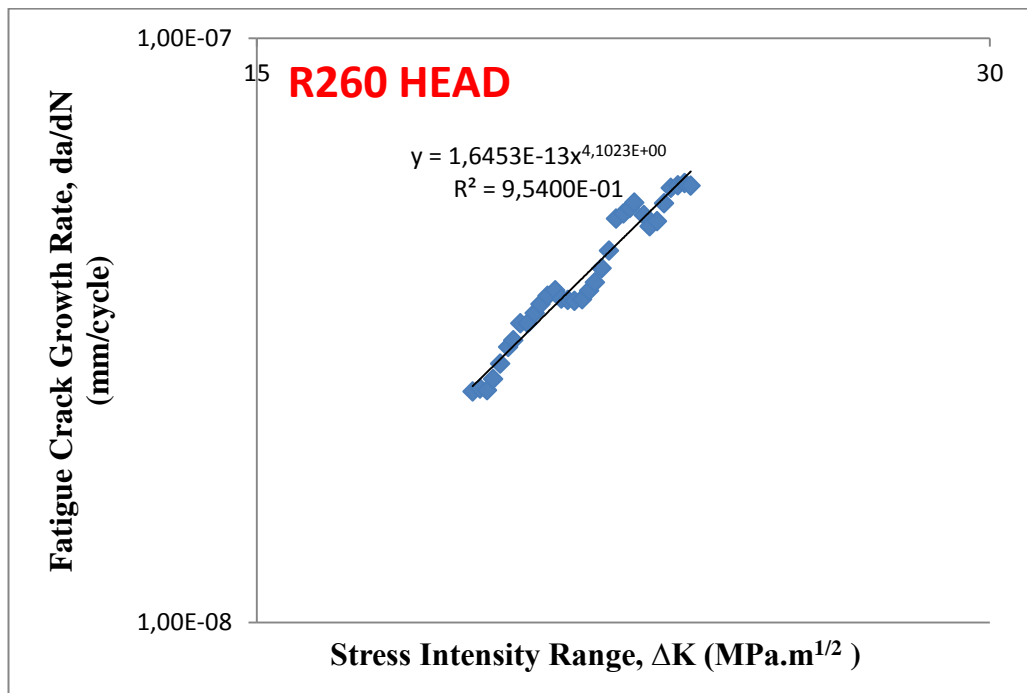


Figure 4.39. Linear region of da/dN vs.ΔK plot of R260 HEAD.

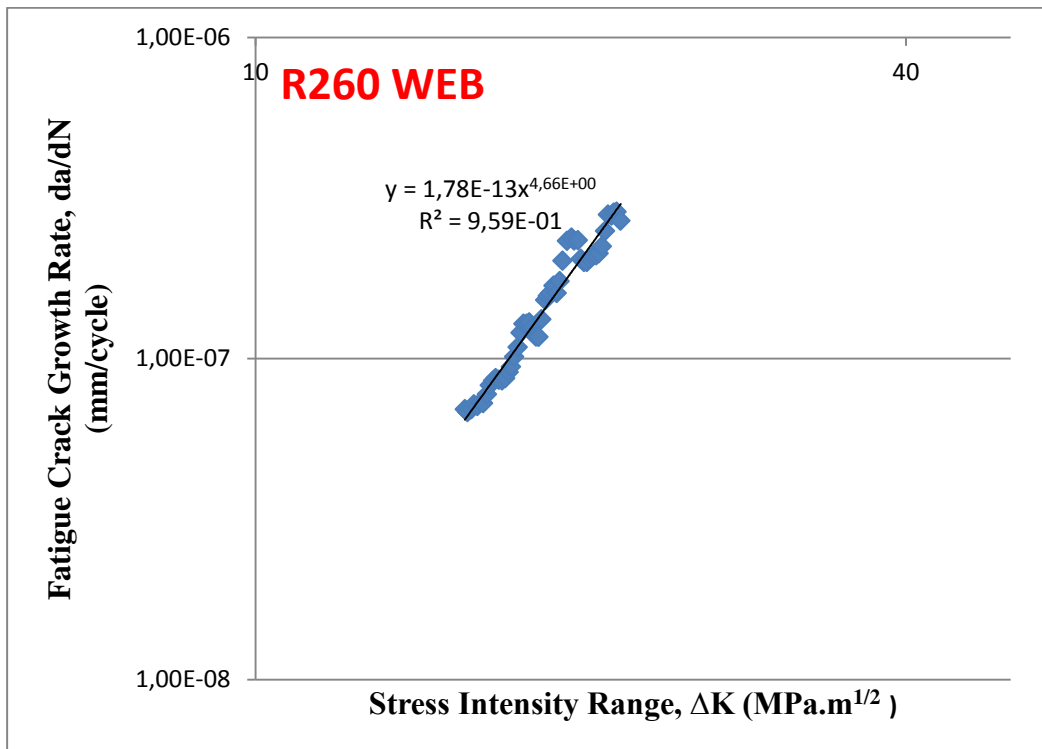


Figure 4.40. Linear region of da/dN vs.ΔK plot of R260 WEB.

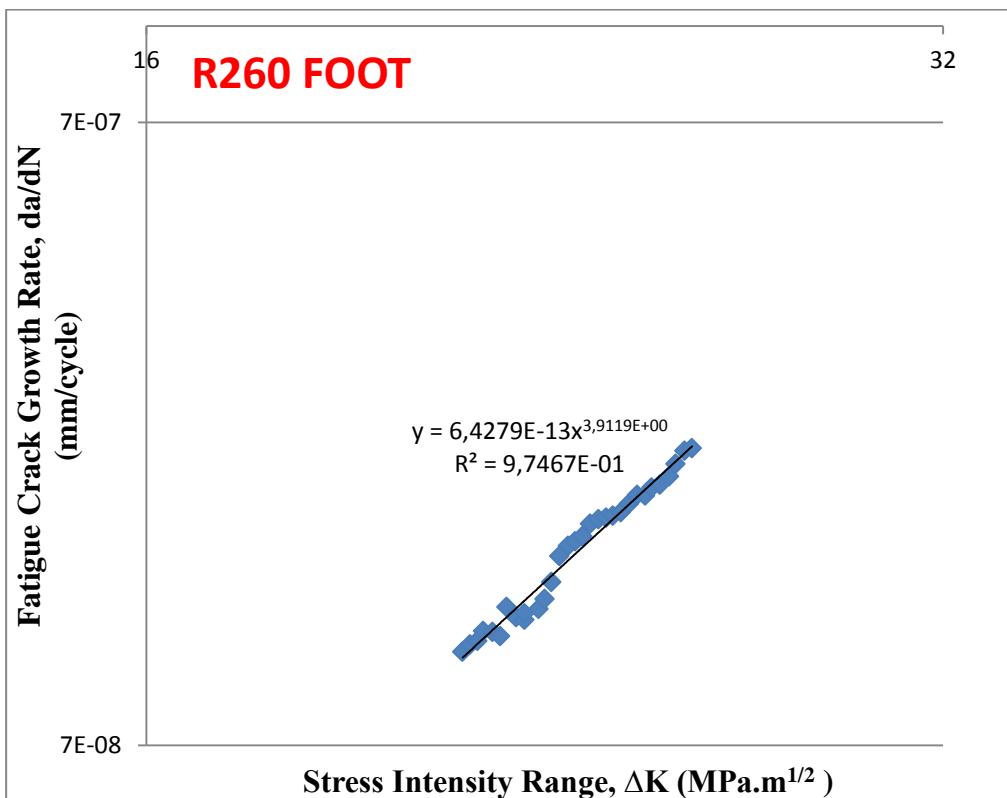


Figure 4.41. Linear region of da/dN vs.ΔK plot of R260 FOOT.

Table 4.12. Results of the constants C and m.

Specimen No	C	m	R²
R350HT HEAD	2.525X10 ⁻¹³	3.91	0.94
R350HT WEB	1.004X10 ⁻¹²	3.62	0.97
R350HT FOOT	5.034X10 ⁻¹⁴	4.62	0.91
R260 HEAD	1.64X10 ⁻¹³	4.1	0.95
R260 WEB	1.78X10 ⁻¹³	4.66	0.95
R260 FOOT	6.42X10 ⁻¹³	3.91	0.97

Table 4.13. Mode I fatigue crack growth rate data at $\Delta K = 25 \text{ MPa.m}^{1/2}$.

Specimen No	da/dN(m/cycle)	Stress Ratio (R)	Fracture Toughness MPa.m^{1/2}	
			K_{IC}	K_Q
R350HT HEAD	7.406X10 ⁻⁸	0.1	42.2	---
R350HT WEB	1.161X10 ⁻⁷	0.1	---	68.1
R350HT FOOT	1.447X10 ⁻⁷	0.1	43.4	---
R260 HEAD	8.928X10 ⁻⁸	0.1	34.1	---
R260 WEB	5.818X10 ⁻⁷	0.1	---	44.1
R260 FOOT	1.891X10 ⁻⁷	0.1	46.7	---

4.9. COMPARISON OF THE da/dN vs ΔK

The plots of da/dN versus ΔK of rail R350 HT and R260 in the head, web and foot compared with each other in Figures 4.42 to 4.44.

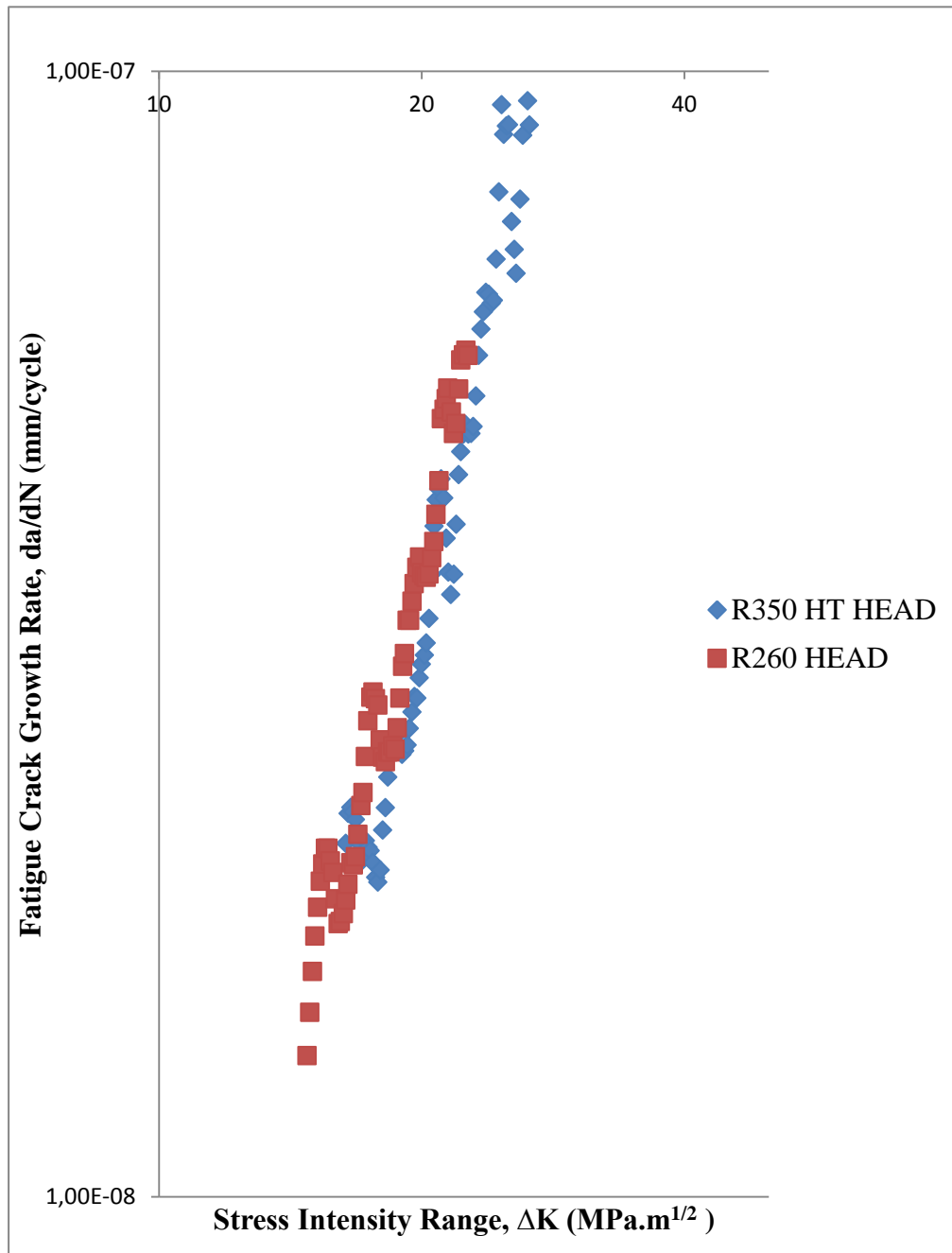


Figure 4.42. Comparison of da/dN vs. ΔK plot of R350 HT HEAD versus R260 HEAD.

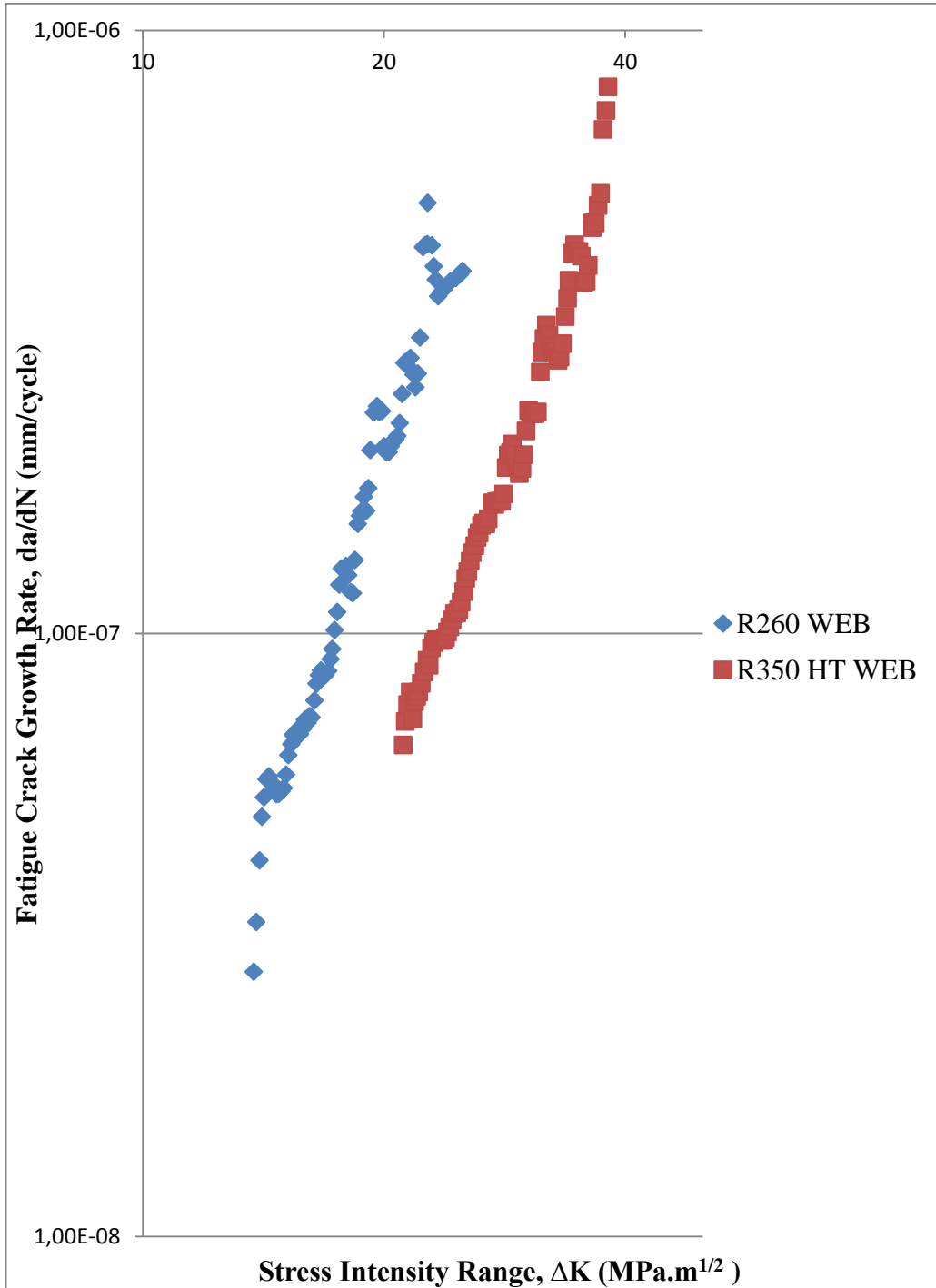


Figure 4.43. Comparison of da/dN vs. ΔK plot of R350 HT WEB versus R260 WEB.

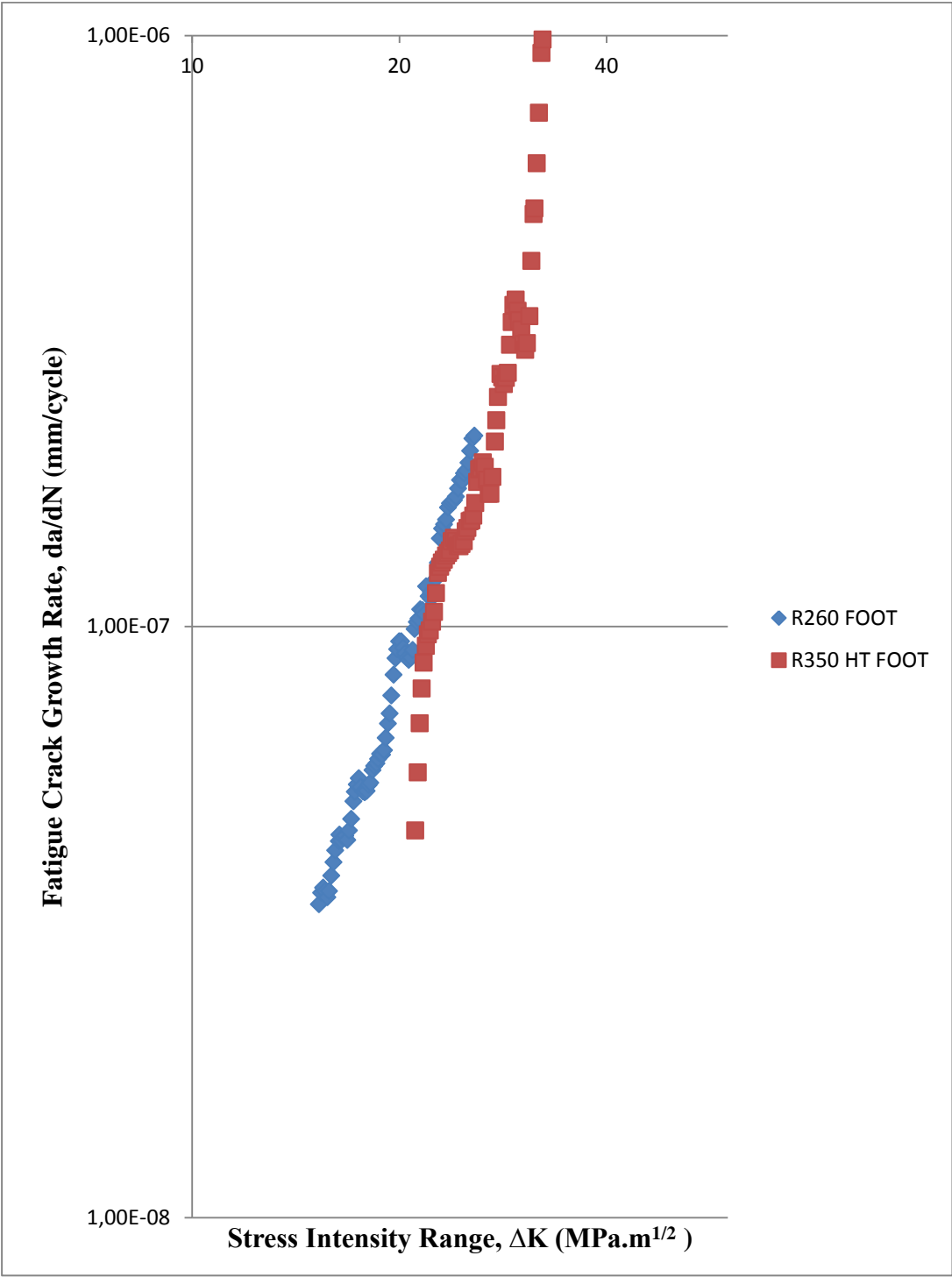


Figure 4.44. Comparison of da/dN vs ΔK plot of R350 HT FOOT versus R260 FOOT.

Fatigue crack growth rate at $\Delta K = 25 \text{ MPa}\cdot\text{m}^{1/2}$ calculated for both Rail R350 HT and R260 in the head, web and foot (table 4.11).

As seen in Table 4.13, Fatigue resistance of R350 HT HEAD specimen in transverse direction is higher than web and foot specimens. Furthermore, Fatigue crack growth resistance of web is higher than foot specimen in the same direction.

Calculation of crack growth rates are provided in Table 4.13. R260 HEAD specimen in transverse direction has more fatigue crack growth resistance than those of web and foot specimens. Furthermore, fatigue crack growth resistance of foot is higher than web specimen in the same direction.

When the fatigue crack propagation of two rails R350 HT and R260 compared in the head in transverse direction, as seen in Table 4.13, fatigue crack growth resistance of R350 HT is a little bit higher than that of R260, yet it is not so pronounced. This difference in fatigue crack growth rate can also be correlated to the microstructure of the head of the rail grades since rail R350 HT has fine pearlite (fig 4.5) when compared to rail R260 (fig 4.7). It might be concluded that R350 HT and R260 have nearly same fatigue crack propagation in the head of rail.

Comparing web specimens of fatigue crack propagation of two rails R350 HT and R260 in the transverse direction, it is clear from Table 4.13 and Figure 4.43 that R350 HT specimen is more resistant than R260 specimen. This difference between fatigue crack propagation rates at the rail web can be correlated to the value of fracture toughness of the web and. Since, in the webs of R350 HT and R260 rails (table 4.8-b and 4.9-b), the fracture toughness values are $68.1 \text{ MPa}\cdot\text{m}^{1/2}$ and $36.5 \text{ MPa}\cdot\text{m}^{1/2}$ respectively. Pearlite grain size has also a great effect on fatigue crack growth rate, rail R350 HT has finer grain size (fig 4.1-b) when compared to R260 (fig 4.2-b).

Comparing the fatigue crack growth rates of foot specimens of two rails of interest in the transverse direction, at $\Delta K = 25 \text{ MPa}\cdot\text{m}^{1/2}$ in Table 4.13, it is apparent that rail R350 HT has more fatigue crack growth resistance than that of R260. But, when looking at the Figure 4.44 the two da/dN vs ΔK plots behave nearly in the same manner. Furthermore, Paris-Erdogan fit to the linear portion of the plot of da/dN

versus ΔK for the foot specimen of R350 HT has lower regression coefficient. Therefore, it may be concluded that due to the reduced of goodness of fit as compared to the other curve fits, calculated C and m constants are not so reliable for the foot specimen of R350HT. The microstructure of two rails R350 HT and R260 are same in the foot (fig 4.1-c and 4.2-c).

4.10. ELECTRON FRACTOGRAPHIC ANALYSIS

The fracture surface of both of the rail R350 HT and R260 were examined under the Scanning Electron Microscope (SEM). The fracture surfaces of the specimens are shown in Figures 4.45 to 4.52. Yellow line on the fractographs shows direction of the fatigue crack growth propagation. Moreover, in some fractographs direction of microcracks were indicated with red arrow. Microcrack growth rates of specimens calculated from striations on fractographs. Image J computer program used to measure distance of striation precisely. Results of microcrack growth rates are given in Table 4.14.

Table 4.14.Micro crack growth rate of rail R350 HT and R260.

Specimen No	da/dN(m/cycle)
R350HT HEAD	2.34×10^{-7}
R350HT WEB	2.03×10^{-7}
R350HT FOOT	3.00×10^{-7}
R260 HEAD	1.87×10^{-7}
R260 WEB	3.56×10^{-7}
R260 FOOT	3.21×10^{-7}

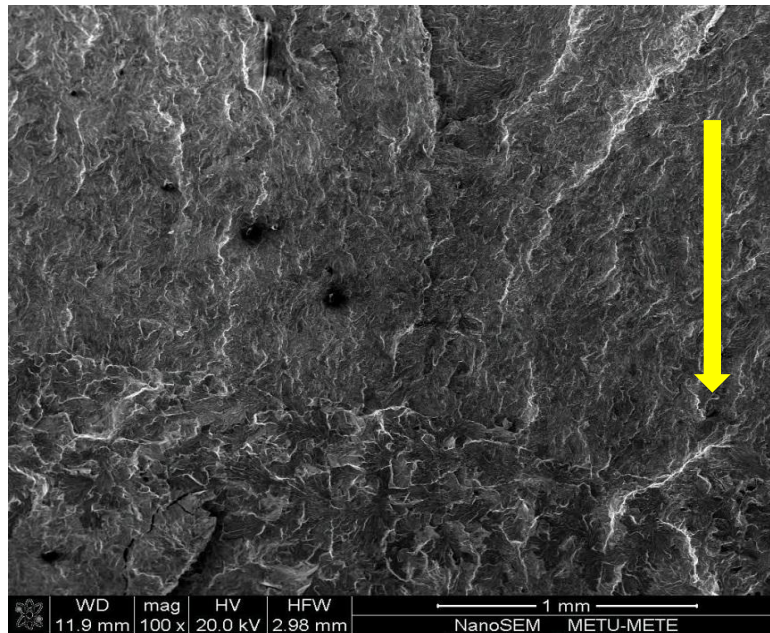


Figure 4.45. SEM fractographs of Mode I Fracture Toughness Specimen in WEB Longitudinal Direction of R260. (a) General view of fracture surface transition from fatigue precrack to final loading region Magnification: 100 X

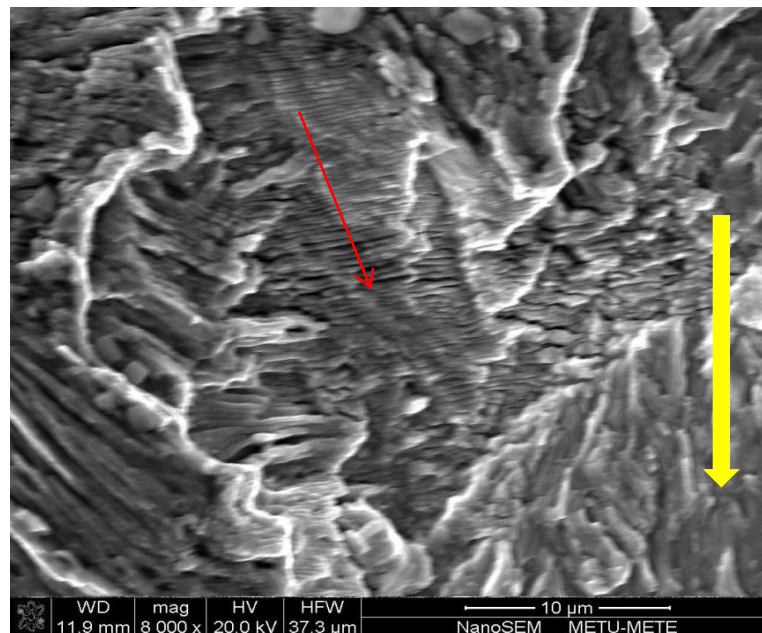


Figure 4.45. SEM fractographs of Mode I Fracture Toughness Specimen in WEB Longitudinal Direction of R260. (b) Fatigue fracture striations in precrack region between two tear ridges. Magnification: 8000 X

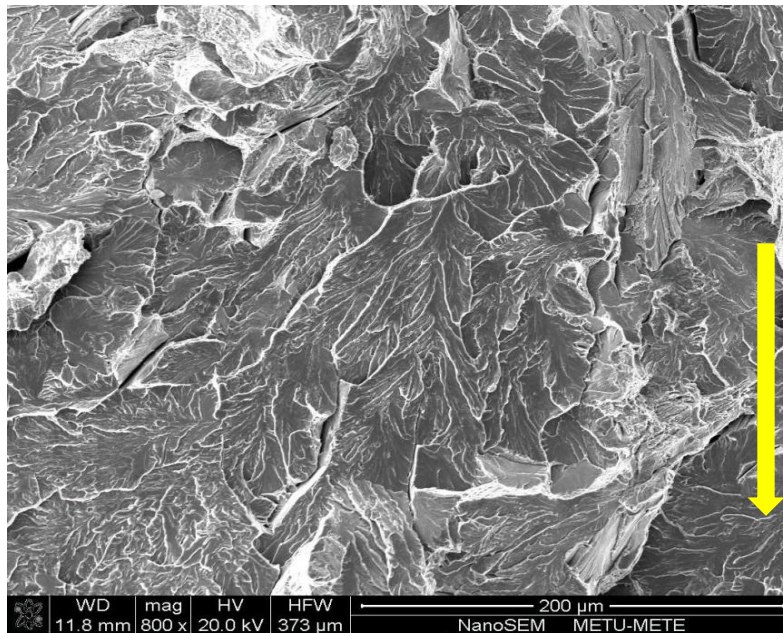


Figure 4.45. SEM fractographs of Mode I Fracture Toughness Specimen in WEB Longitudinal Direction of R260.(c) Final loading region with brittle cleavage fracture and river markings in each grain. Magnification: 800 X

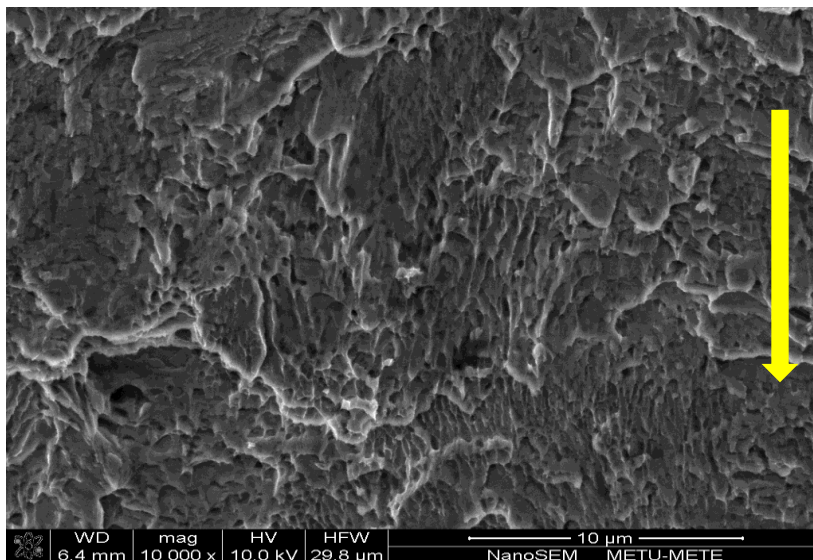


Figure 4.46. SEM fractographs of Mode II Fracture Toughness Specimen in WEB Longitudinal Direction of R260. (a) General view of elongated shear dimples on the ductile fracture surface. Magnification: 10000 X

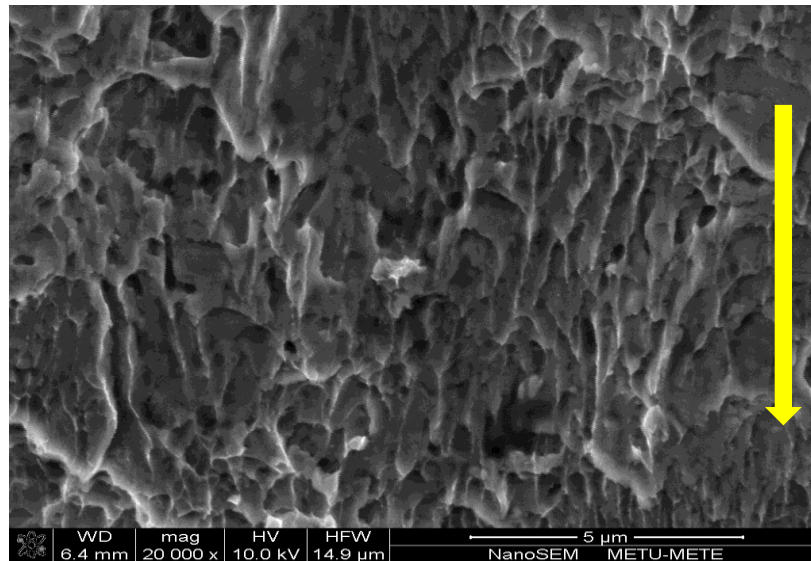


Figure 4.46. SEM fractographs of Mode II Fracture Toughness Specimen in WEB Longitudinal Direction of R260. (b) Cup-like depressions of shear dimples can be seen easily in the close view of ductile fracture. Magnification: 20000 X

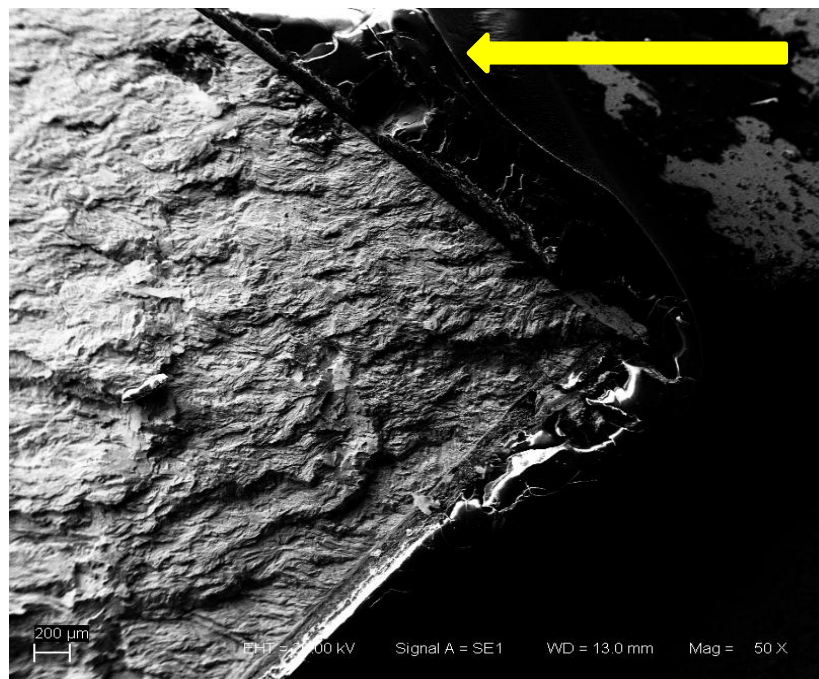


Figure 4.47. SEM fractographs of R350 HT HEAD in Transverse Direction. (a) Fatigue crack propagation from starter chevron notch. Magnification: 50 X

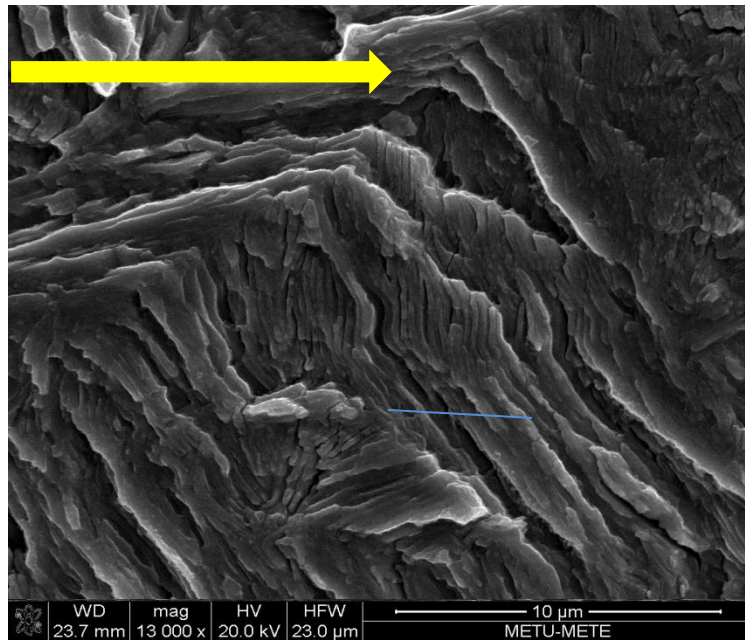


Figure 4.47. SEM fractographs of R350 HT HEAD in Transverse Direction. (b) Fatigue striations in the stage II region. Magnification: 13000 X

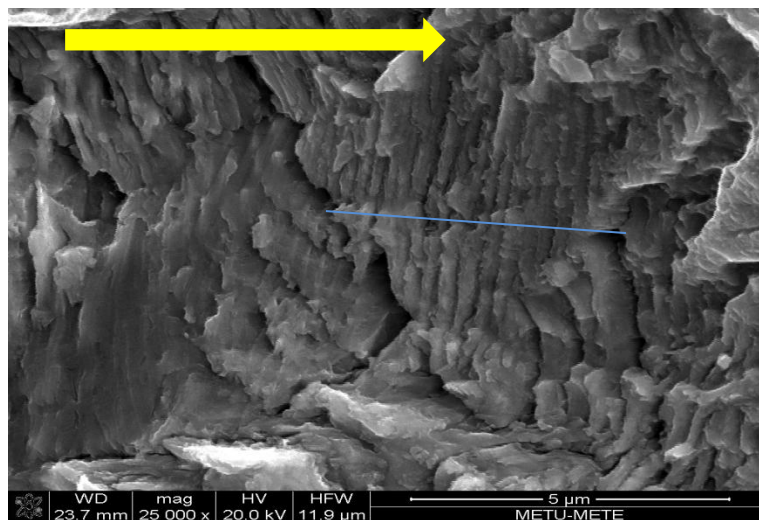


Figure 4.47. SEM fractographs of R350 HT HEAD in Transverse Direction. (c) Close view of fatigue striations in the stage II region. Magnification: 25000 X

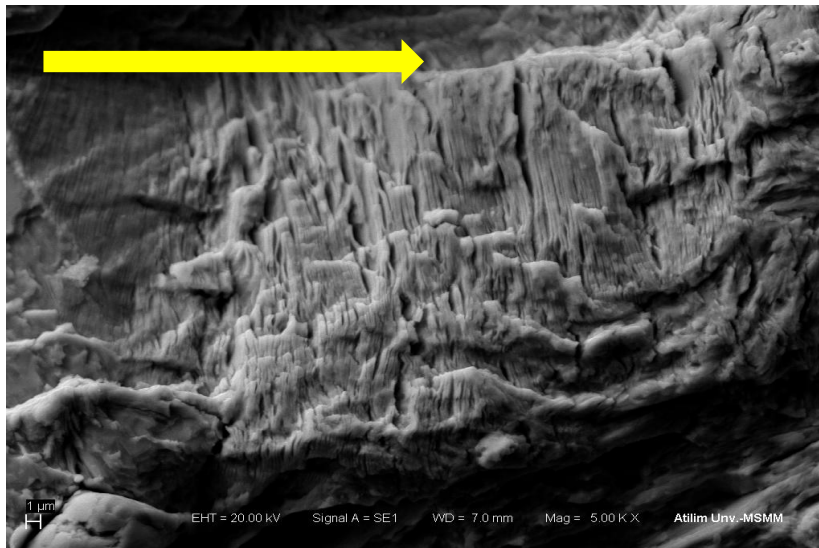


Figure 4.48. SEM fractographs of rail R350 HT WEB in Transverse Direction. (a) Fatigue crack propagation striations between tear ridges. Magnification: 5000 X

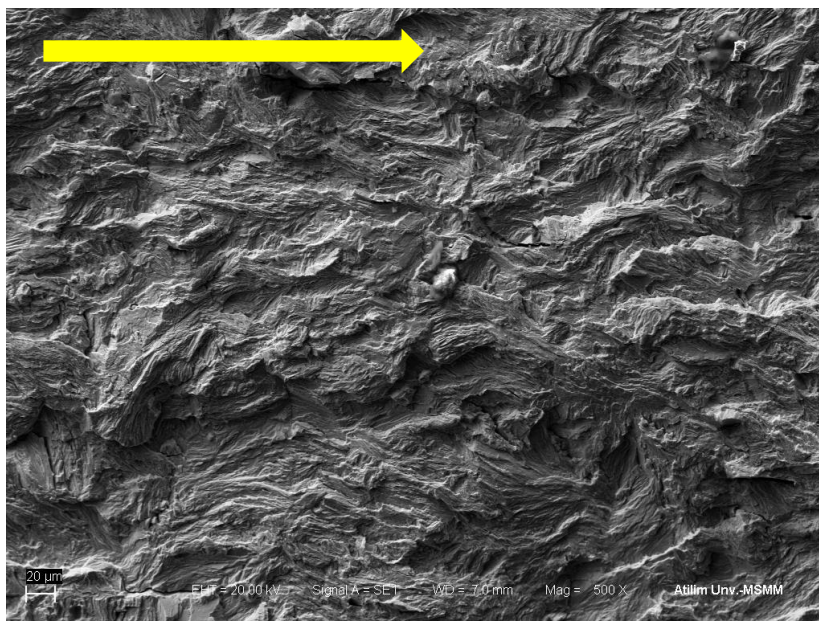


Figure 4.48. SEM fractographs of rail R350 HT WEB in Transverse Direction. (b) General view of fatigue crack propagation in stage II region. Magnification: 500 X

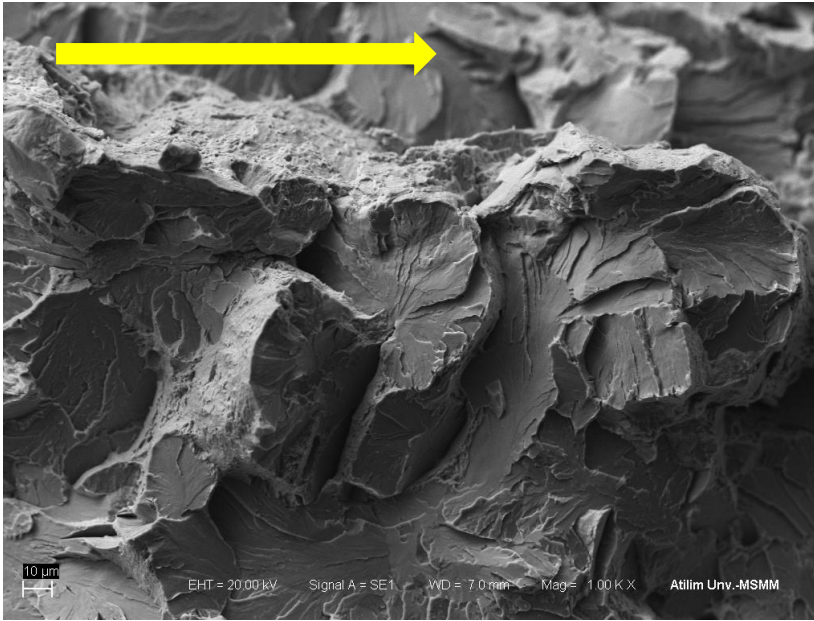


Figure 4.48. SEM fractographs of rail R350 HT WEB in Transverse Direction.(c)
Brittle cleavage fracture and river markings in each grain. Magnification: 1000 X

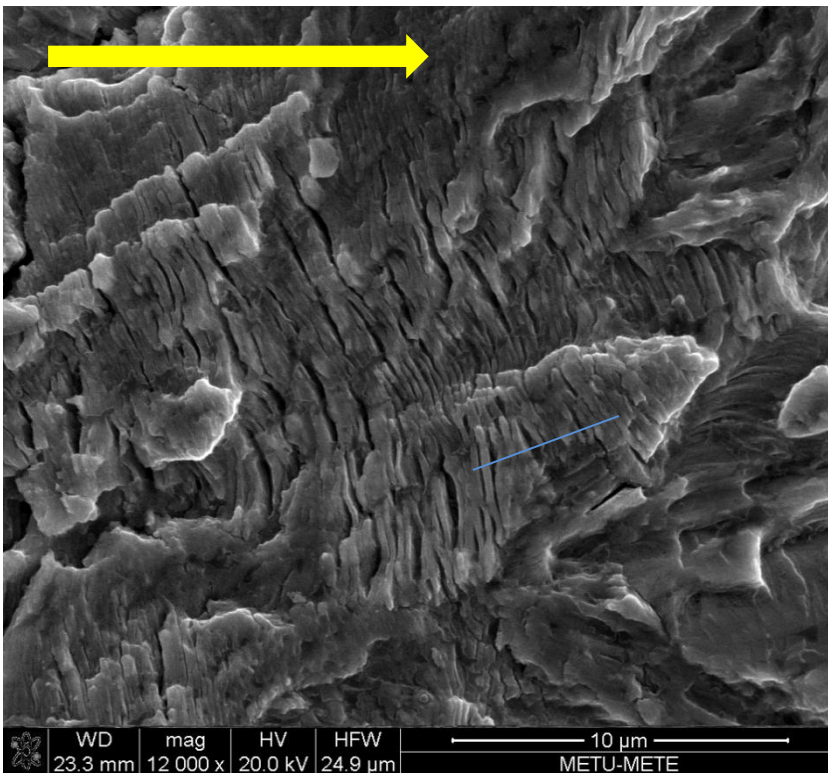


Figure 4.48. SEM fractographs of rail R350 HT WEB in Transverse Direction. (d)
Secondary cracks between striations and tear ridges on different planes.
Magnification: 12000 X

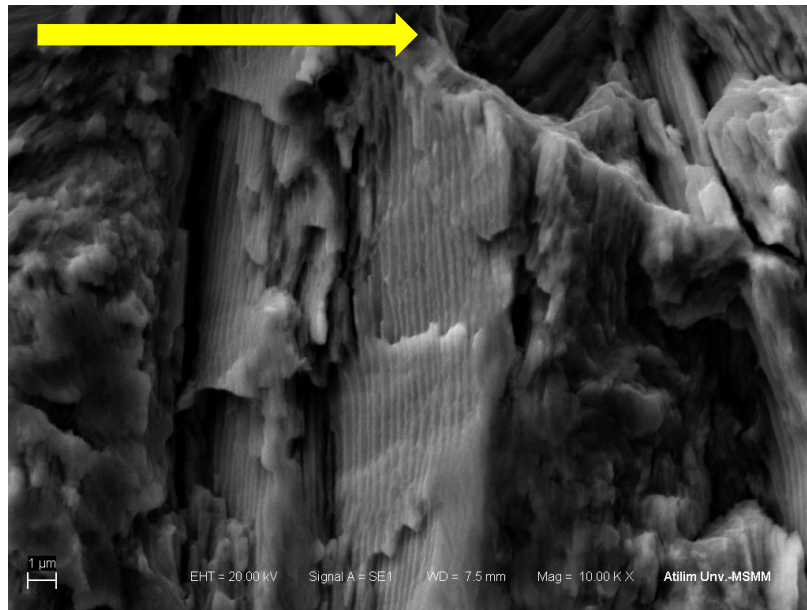


Figure 4.49. SEM fractographs of rail R350 HT FOOT in Transverse Direction. (a) Pearlite morphology in stage II region of fatigue crack propagation. Magnification: 10000 X

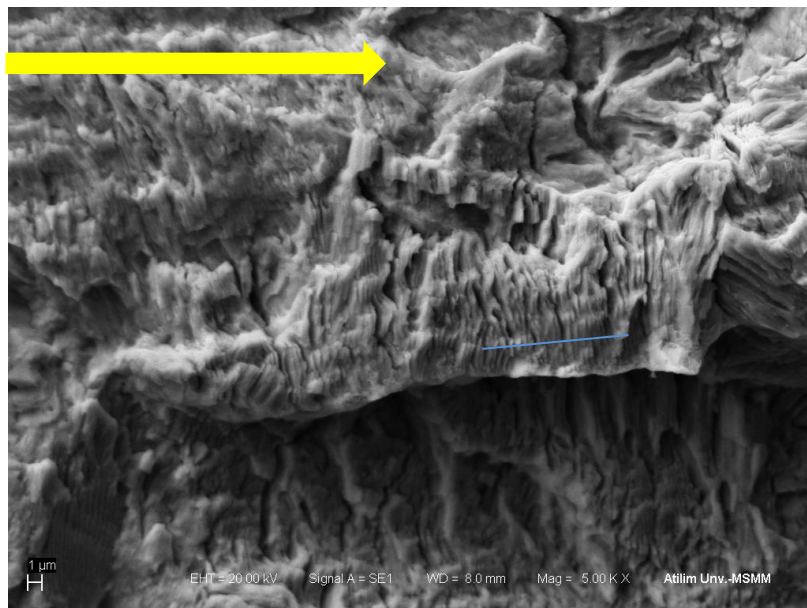


Figure 4.49. SEM fractographs of rail R350 HT FOOT in Transverse Direction. (b) Fatigue striation in direction of fatigue crack propagation. Magnification: 5000 X

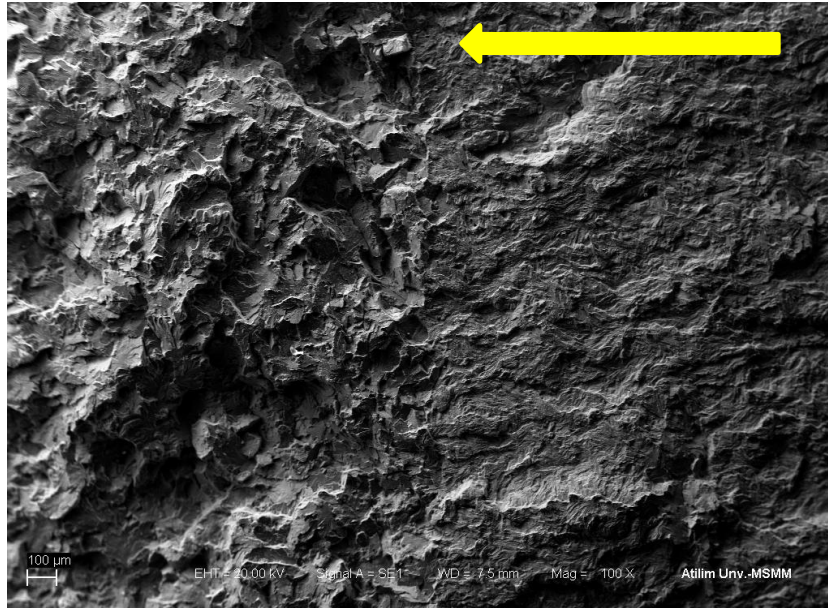


Figure 4.49. SEM fractographs of rail R350 HT FOOT in Transverse Direction.(c)
 Transition from fatigue crack propagation region to fast brittle fracture region.
 Magnification: 100 X

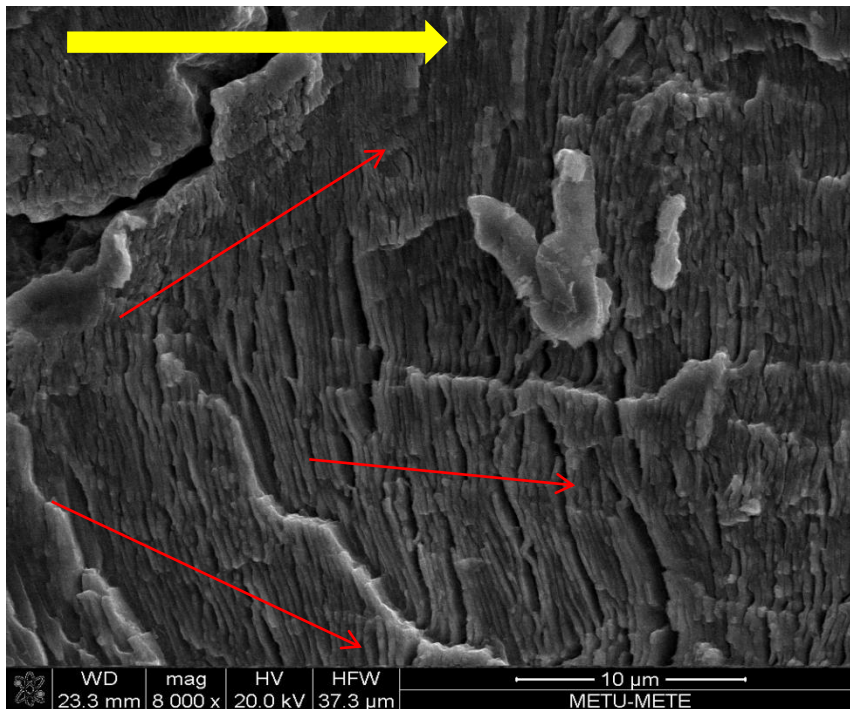


Figure 4.50. SEM fractographs of rail R260 HEAD in Transverse Direction.(a)
 Crack propagation in stage II region on multiple plateaus at different elevations.
 Magnification: 8000 X

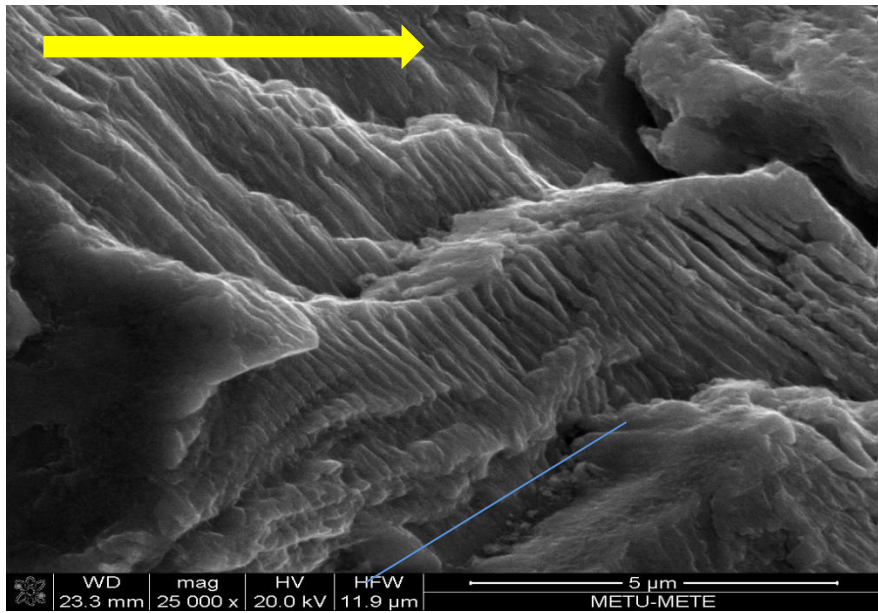


Figure 4.50. SEM fractographs of rail R260 HEAD in Transverse Direction.(b)
Close view of tear ridges and fatigue striation. Magnification: 25000 X

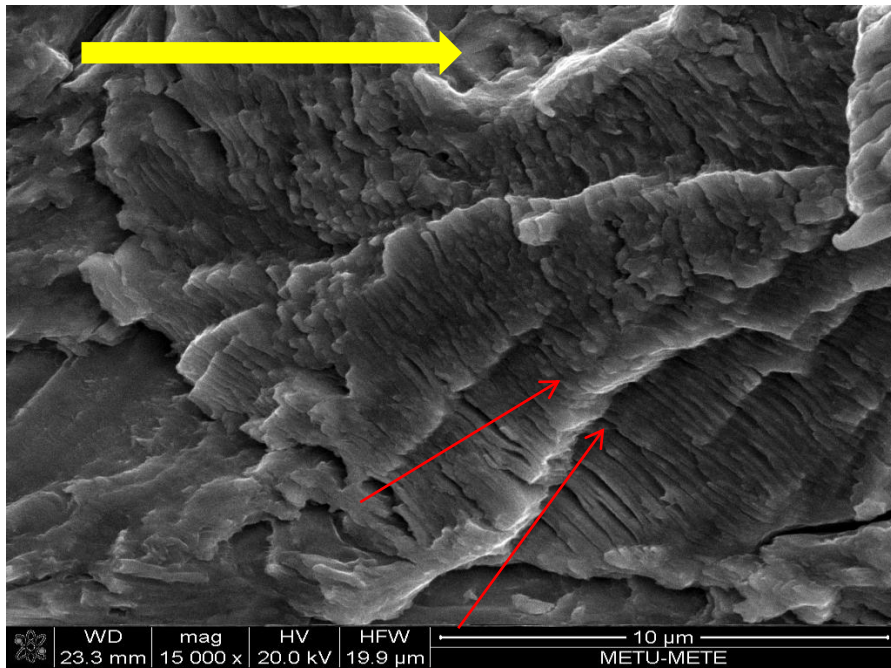


Figure 4.50. SEM fractographs of rail R260 HEAD in Transverse Direction.(c)
Joining of two fatigue striation plateaus by tear ridges. Magnification: 15000 X

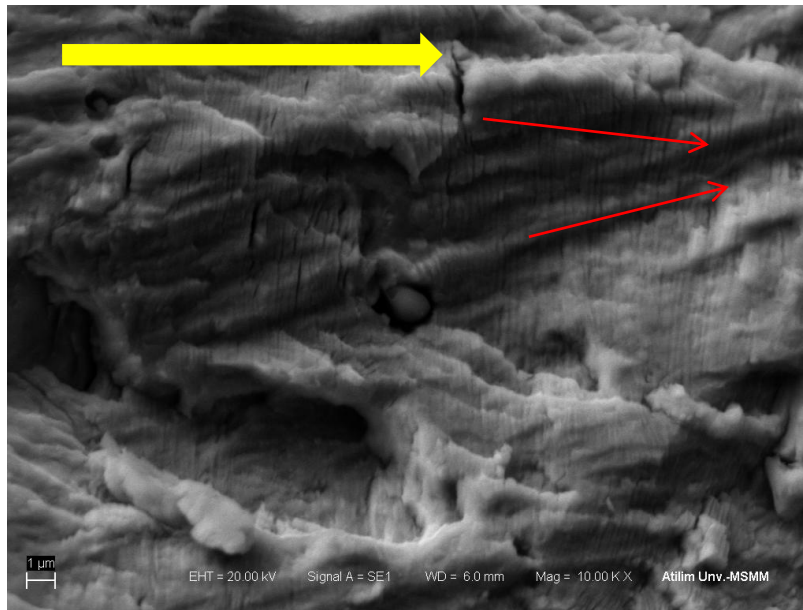


Figure 4.51. SEM fractographs of rail R260 WEB in Transverse Direction.(a)
Joining of fatigue striation by walls which contain fatigue striation. Magnification:
10000 X

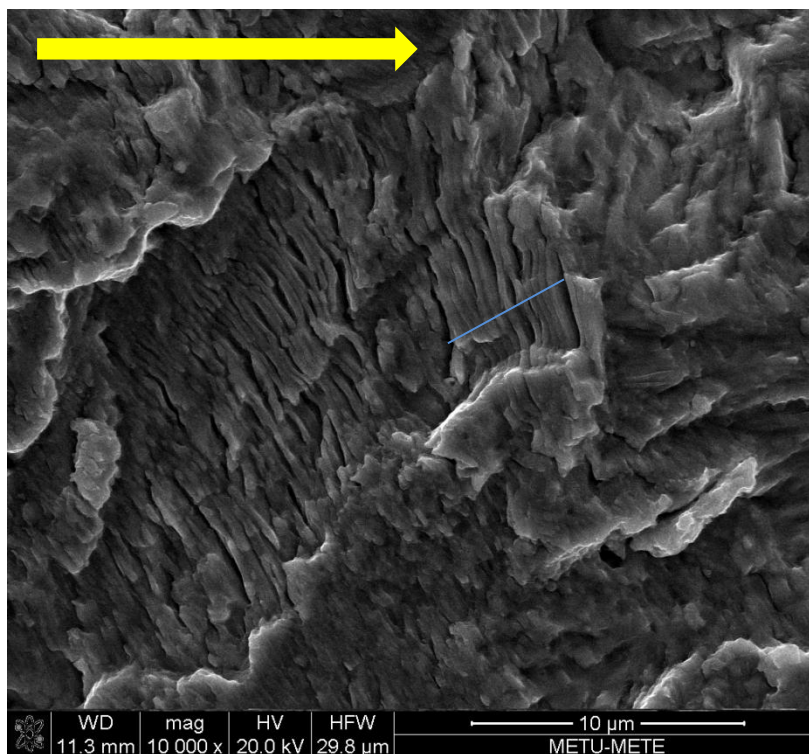


Figure 4.51. SEM fractographs of rail R260 WEB in Transverse Direction. (b)
Forming of secondary cracks between fatigue striations. Magnification: 10000 X

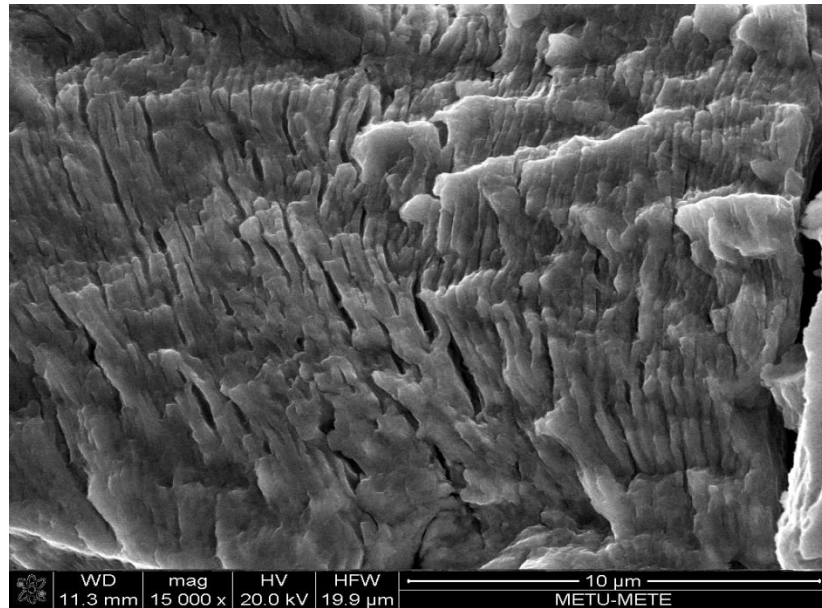


Figure 4.51. SEM fractographs of rail R260 WEB in Transverse Direction. (c) Fatigue striations in stage II region of propagation. Magnification: 15000 X

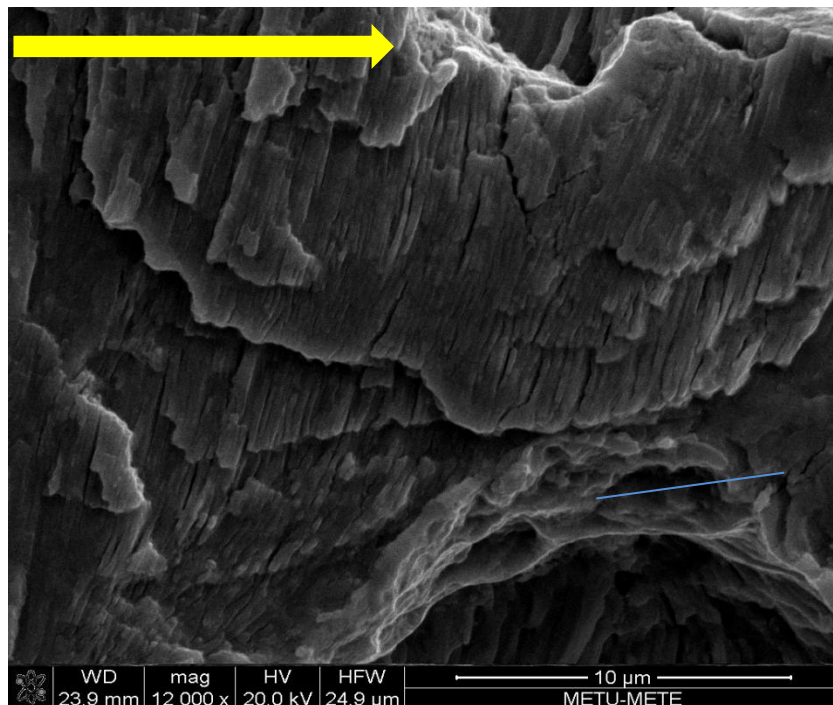


Figure 4.52. SEM fractographs of rail R260 FOOT in Transverse Direction. Fatigue crack propagation between two tear ridges. Magnification: 12000 X

CHAPTER 5

CONCLUSIONS

In this study, fatigue crack propagation of rail R350 HT and R260 under tensile mode in three different region of the 60 kg/m rail steel investigated. From the results of the study it can be said that head hardened rail steels can be replaced with rail R260. The main conclusions drawn from the data are as follows

1. Mode I Fracture toughness of R350 HT is higher than that of R260, in the head and the web.
2. Fatigue crack growth resistance of R350 HT in transverse direction is higher in the head as compared to web and foot. Furthermore, fatigue crack growth resistance of web is higher than foot specimen in the same direction.
3. R260 head specimen in transverse direction has greater fatigue crack growth resistance than those of web and foot specimens.
4. Fatigue crack growth resistance of R350 HT is a little bit higher than that of R260, yet it is not so pronounced. It might be concluded that R350 HT and R260 have nearly same fatigue crack propagation rate in the head of rail. Fatigue crack propagation resistance of web of R350 HT in the transverse direction is higher than that of R260 specimen.
5. Fatigue crack growth rates of foot specimens of two rails of interest in the transverse direction are nearly the same.
6. Mode I fracture toughness, K_{IC} of rail R260 in the web is lower than the Mode II fracture toughness, K_{IIIC} in the longitudinal direction.

REFERENCES

1. W. Schütz, Engineering Fracture mechanics, Vol.54, 1996, pp.263-300.
2. S. Suresh, 'Fatigue of materials', Cambridge University Press, 1998, pp.1.
3. R.J. Sanford, 'Principles of Fracture Mechanics', Prentice Hall, 2003, pp.282.
4. Zerbst U, Lunden R, Edel K. O, Smith R. A. Introduction to the damage tolerance behaviour of railway rails - a review Elsevier: Engineering Fracture Mechanics 2009;76:2563-2601
5. M.E. Fine, Metall. Trans. A, Vol.11A, 1980, PP.368-379.
6. ASM Handbook, Volume 19, 'Fatigue and Fracture', pp.368-379.
7. <http://www.keytometals.com/page.aspx?ID=CheckArticle&site=kts&NM=299>
2014
8. <http://www.key-to-steel.com/Articles/Art162.htm>. 2013
9. W.A. Wood, Bull. Inst. Met., Vol.3, 5-6, (1955)
10. G.E. Dieter, "Mechanical Metallurgy", McGraw Hill, (1988)
11. W.D. Callister, "Fundamentals of Materials Science and Engineering", Wiley, (2001)
12. R.G. Forman, V.E. Kearney, and R.M. Engle, "Numerical Analysis of Crack Propagation in Cyclic Load Structure", Trans. ASME, J. Basic Eng., Vol.89, 459, (1967)
13. H. LEwalds and R.J.H. Wanhill, Fracture Mechanics, Edward Arnold, (1984)
14. Skyttebol A. Continuous welded railway rails: residual stress analyses, fatigue assessments and experiments. PhD Thesis, Chalmers University of Technology, Goteburg, Sweden; 2004.
15. Esveld C. Modern rail way track. 2nd ed. Zaltbommel, The Netherlands: MTR-Productions; 2001.
16. Zerbst U. Paper on rail material properties relevant for damage tolerance
17. Orringer O, Tang YH, Gordon JE, Jeong DY, Morris JM, Pertman AB, Crack propagation life of detail fractures in rails. US Department of Transportation, FRA, DOT/FRA/ORD-88/13; 1988.

18. Cannon DF, Edel K-O, Grassie SL, Sawley K. Rail Defects : an overview. *Fatigue Fracture Engineering Material Structure* 2003;26:865-87
19. Mayville RA, Stringfellow RG. Numerical Analysis of a railroad bolt hole fracture problem. *Theor Apply Fract Mech* 1995;24:1-12
20. Madshus C, Kaynia AM. High speed railway lines in soft ground: dynamic behavior at critical train speed. *J Sound Vib* 2004;275:515-32
21. Skyttebol A, Josefson BL, Numerical simulation of flash-butt welding of railway rails. In: Cerjak H, Editor. *Mathematical modelling of weld phenomena*. Graz, Austria: TU Graz Publishing; 2004. p.7.
22. ERRI Committee D 173/RP42 rail rolling contact fatigue. Residual stress measurements on naturally hard and two head-hardened rails by neutron diffraction, Utrecht; 1993
23. Webster PJ, Wang X, Mills G, Kamg W, Webster GA. Residual stress measurements on ORE railway rails by neutron diffraction. UIC, Final Report BRSUIC02/91; 1991.
24. René Heyder, Gregor Girsch, Testing of HSH® rails in high-speed tracks to minimise rail damage, *Wear*, Volume 258, Issues 7–8, March 2005, Pages 1014-1021
25. KRAK-GAGE® Theory of Operation , www.krak-gage.com. 2013
26. EN 13674-1:2003+A1 Railway applications-Track-Rail-part 1:Vignole railway rails 46 kg/m above.
27. TS EN ISO 6892-1 Metallic materials - Tensile testing - Part 1: Method of test at room temperature.
28. ASTM E23-12, Standard Test Methods for Notched Bar Impact Testing of Metallic Materials
29. ASTM E10-12 Standard Test Method for Brinell Hardness of Metallic Materials.
30. ASTM E399-09ε2 Standard Test Method for Linear-Elastic Plane-Strain Fracture Toughness K_{Ic} of Metallic Materials.
31. ASTM E647-11 Standard Test Method for Measurement of Fatigue Crack Growth Rates.

32. L.Banks-Sills, M.Arcan, "A Compact Mode II Fracture Specimen", Fracture Mechanics, Vol.17, 347-363, (1986)
- 33.N. J .Petch, J .Iron Steel Inst. London , vol. 174, p. 25,1953.
34. <https://www.efatigue.com/constantamplitude/crackgrowth/#a>. 2013

APPENDIX A

OUTPUT OF BASIC COMPUTER PROGRAM FOR R350 HT HEAD

NO	CYCLES	A (MEAS.)	A (REG)	M.C.C.	DELTA K	da/dN
1	0	9.0000				
2	10687	9.4000				
3	14057	9.5000				
4	17507	9.6000	9.5980	0.9987	15.09153	0.000028503035
5	22067	9.7000	9.7138	0.9990	15.21250	0.000026102260
6	25237	9.8000	9.7961	0.9988	15.29828	0.000024995992
7	29287	9.9000	9.8954	0.9988	15.40214	0.000023877663
8	33647	10.0000	9.9974	0.9986	15.50950	0.000023262071
9	38527	10.1000	10.1007	0.9990	15.61933	0.000022546059
10	43277	10.2000	10.2028	0.9988	15.72744	0.000023880582
11	47467	10.3000	10.3062	0.9976	15.83699	0.000024164301
12	51287	10.4000	10.4083	0.9949	15.94588	0.000023353203
13	54357	10.5000	10.4836	0.9972	16.02728	0.000023402281
14	59337	10.6000	10.5915	0.9959	16.14336	0.000021701935
15	65527	10.7000	10.7111	0.9961	16.27181	0.000020177195
16	70307	10.8000	10.7984	0.9991	16.36610	0.000020600341
17	75157	10.9000	10.8990	0.9996	16.47597	0.000021901802
18	79806	11.0000	11.0100	0.9982	16.59725	0.000022177266
19	83466	11.1000	11.0951	0.9982	16.69051	0.000021979729
20	87716	11.2000	11.1908	0.9991	16.79623	0.000021635420
21	93186	11.3000	11.3035	0.9984	16.92125	0.000020653557
22	98266	11.4000	11.4006	0.9994	17.02907	0.000019827998
23	103566	11.5000	11.5016	0.9998	17.14183	0.000020134665
24	108276	11.6000	11.5980	0.9998	17.24951	0.000020716172
25	113345	11.7000	11.7078	0.9986	17.37348	0.000020434994
26	117525	11.8000	11.7962	0.9991	17.47314	0.000020302881
27	122265	11.9000	11.8907	0.9991	17.5812	0.000019810517
28	128305	12.0000	12.0066	0.9988	17.71384	0.000019222825
29	133505	12.1000	12.1001	0.9995	17.82075	0.000019031480
30	138745	12.2000	12.1980	0.9999	17.93396	0.000019514364
31	143985	12.3000	12.3012	0.9989	18.05358	0.000021170419
32	148653	12.4000	12.4016	0.9990	18.17152	0.000022171384
33	153313	12.5000	12.5078	0.9990	18.29600	0.000023593539
34	156553	12.6000	12.5870	0.9990	18.38925	0.000024660649
35	161233	12.7000	12.7075	0.9988	18.53287	0.000025379075
36	164813	12.8000	12.8016	0.9990	18.64514	0.000025630261
37	168433	12.9000	12.8943	0.9988	18.75562	0.000024915604
38	172633	13.0000	13.0017	0.9995	18.88607	0.000025033429
39	176573	13.1000	13.0950	0.9992	18.99909	0.000024725245
40	181193	13.2000	13.2065	0.9996	19.13605	0.000024907236
41	184993	13.3000	13.3023	0.9995	19.25297	0.000025205120
42	188633	13.4000	13.3934	0.9994	19.36562	0.000026075846
43	192572	13.5000	13.5002	0.9995	19.49892	0.000026962949
44	196572	13.6000	13.6074	0.9995	19.63315	0.000027828773

45	199652	13.7000	13.6956	0.9988	19.74553	0.000027742170
46	203412	13.8000	13.8012	0.9984	19.87896	0.000028921440
47	206532	13.9000	13.8927	0.9984	19.99666	0.000029724735
48	210652	14.0000	14.0145	0.9987	20.15389	0.000030297457
49	213172	14.1000	14.0922	0.9987	20.25382	0.000031045482
50	216492	14.2000	14.1943	0.9984	20.38703	0.000032652802
51	219752	14.3000	14.3036	0.9976	20.53178	0.000035710480
52	222692	14.4000	14.4058	0.9995	20.66704	0.000039440038
53	225052	14.5000	14.5028	0.9987	20.79662	0.000041618052
54	227172	14.6000	14.5993	0.9979	20.92578	0.000042543907
55	229212	14.7000	14.6927	0.9995	21.05317	0.000043434182
56	231692	14.8000	14.8014	0.9997	21.20067	0.000041767162
57	234272	14.9000	14.9072	0.9995	21.34664	0.000038478847
58	236652	15.0000	14.9920	0.9989	21.46457	0.000035889650
59	239672	15.1000	15.0914	0.9970	21.60294	0.000034292229
60	243392	15.2000	15.2085	0.9947	21.76930	0.000035731166
61	246272	15.3000	15.3068	0.9981	21.90869	0.000039570601
62	248732	15.4000	15.4055	0.9991	22.05065	0.000043822041
63	250512	15.5000	15.4913	0.9986	22.17348	0.000045915302
64	252732	15.6000	15.6016	0.9992	22.33520	0.000047602571
65	254692	15.7000	15.6969	0.9994	22.47284	0.000048519698
66	256871	15.8000	15.8009	0.9996	22.62903	0.000047609832
67	259045	15.9000	15.9053	0.9996	22.78462	0.000047674752
68	260895	16.0000	15.9907	0.9993	22.91436	0.000048345104
69	263215	16.1000	16.1015	0.9984	23.08331	0.000051464947
70	265275	16.2000	16.2068	0.9987	23.24468	0.000055914759
71	266985	16.3000	16.3033	0.9991	23.39359	0.000059010101
72	268445	16.4000	16.3965	0.9988	23.54068	0.000061120489
73	269965	16.5000	16.4948	0.9996	23.69540	0.000063606334
74	271615	16.6000	16.6019	0.9996	23.86597	0.000063369946
75	273284	16.7000	16.7060	0.9996	24.03344	0.000062206142
76	274684	16.8000	16.7910	0.9994	24.17156	0.000062597959
77	276449	16.9000	16.8986	0.9948	24.34870	0.000068082118
78	278094	17.0000	17.0086	0.9950	24.53107	0.000078146702
79	279484	17.1000	17.1176	0.9978	24.71375	0.000093388939
80	280214	17.2000	17.1950	0.9873	24.84400	0.000087894761
81	281274	17.3000	17.3040	0.9920	25.03013	0.000089399509
82	282054	17.4000	17.3762	0.9958	25.15422	0.000089625559
83	283734	17.5000	17.4995	0.9940	25.37010	0.000073517534
84	285354	17.6000	17.6011	0.9940	25.54800	0.000069452130
85	286994	17.7000	17.6689	0.9361	25.66884	0.000066156696
86	288264	17.8000	17.8237	0.9845	25.94755	0.000076969067
87	289414	17.9000	17.9262	0.9767	26.13350	0.000087714383
88	291394	18.1000	18.0999	0.9957	26.45549	0.000094153038
89	292144	18.2000	18.1674	0.9905	26.58112	0.000089606699
90	293564	18.3000				
91	294664	18.4000				
92	296111	18.5000				

*--DATA VIOLITE SPECIMEN SIZE REQRIMENTS